SYNTHESIS AND PROPERTIES OF NANOCRYSTALLINE TUNGSTEN HEAVY ALLOY POWDERS CONSOLIDATED BY PULSED ELECTRIC CURRENT SINTERING

by

Steven James Livers

A thesis
submitted in partial fulfillment
of the requirements for the degree of
Master of Science in Materials Science and Engineering
Boise State University

May 2014

BOISE STATE UNIVERSITY GRADUATE COLLEGE

DEFENSE COMMITTEE AND FINAL READING APPROVALS

of the thesis submitted by

Steven James Livers

Thesis Title: Synthesis and Properties of Nanocrystalline Tungsten Heavy Alloy Powders Consolidated by Pulsed Electric Current Sintering

Date of Final Oral Examination: 10 December 2013

The following individuals read and discussed the thesis submitted by student Steven James Livers, and they evaluated his presentation and response to questions during the final oral examination. They found that the student passed the final oral examination.

Megan Frary, Ph.D.	Chair, Supervisory Committee
Rick Ubic, Ph.D.	Member, Supervisory Committee
Dmitri Tenne, Ph.D.	Member, Supervisory Committee

The final reading approval of the thesis was granted by Megan Frary, Ph.D., Chair of the Supervisory Committee. The thesis was approved for the Graduate College by John R. Pelton, Ph.D., Dean of the Graduate College.

ACKNOWLEDGEMENTS

I would like to thank my faculty advisors, Dr. Megan Frary and Dr. Michael Hurley, for their continued support and advice throughout my graduate program. I would also like to thank my thesis committee members, Dr. Frary, Dr. Ubic, and Dr. Tenne for their advice and contributions to completing this work.

A special thanks to the collaborators at MIT for their contributions in the powder processing required for this project. I would also like to thank the Defense Threat Reduction Agency for funding this project for basic research to improve our capabilities to counter threats. Additional thanks to the Center for Advanced Energy Studies, which housed the pulsed electric current sintering machine and Dr. Allahar and Brian Forsmann for their expertise with its operation.

This work wouldn't have been completed in a timely manner without undergraduate support and the Frary Research group. Megan Beck, Kosette Leperi, and Chris Stifter contributed hard work and dedication to this project, which was greatly appreciated.

Family support also contributed to this work. Thank you, Peter Livers and Barbara Livers, for your continued support and words of encouragement. Special thanks to James Livers, my grandfather, who has helped all of his grandchildren complete graduate school.

ABSTRACT

Amorphous and nanocrystalline W-based materials are candidate alloys where high toughness and abrasion resistance are required, such as for kinetic energy penetrators (KEPs). Using a bottom-up approach to produce a tungsten heavy alloy (WHA), W-based alloys, including W-Mo-Fe and W-Cr-Fe, have been produced using high-energy ball milling and consolidated with pulsed electric current sintering (PECS). Powder consolidation using PECS allows for fast consolidation and for high relative densities to be achieved after sintering at a fraction of the melting temperature. Rapid consolidation of the alloyed powders also reduces grain growth, resulting in improved mechanical properties. During consolidation of mechanically alloyed powders, the structure evolves with sintering conditions due to the residual stress introduced during ball milling and the addition of other component elements added to promote amorphization. Multiple nanoscale crystalline microstructures were seen in the W based alloys depending on processing conditions. Negligible porosity was achieved at nearly one third of homologous temperature, 1050 °C for W-Mo-Fe and 1200 °C for W-Cr-Fe, using nanocrystalline powders and consolidating with PECS. Specimens containing nanocrystalline microstructures showed extremely high hardness and improved mechanical properties over several baseline microcrystalline tungsten alloys. Consolidated alloys had improved hardnesses over baseline materials, up to 300%. Intermetallic phase formation aided sintering by filling in pores and acting as a binder phase between nanocrystalline powder particles. At temperatures above 1500 °C, liquid-phase sintering characteristics were observed, including the formation of spheroidal grains and rapid grain growth. PECS offers a novel processing route for tailoring the structure and properties of these advanced alloys by altering the grain size. The ballistic performance of these alloys under selected process parameters will be evaluated during subsequent studies and will determine whether or not these alloys can be used as effective KEPs.

TABLE OF CONTENTS

LIST OF TABLES

LIST OF FIGURES

LIST OF ABBREVIATIONS

ARL	Army Research Laboratory
EDS	Energy Dispersive X-ray Spectroscopy
HP	High Pressure
KEP	Kinetic Energy Penetrator
LP	Low Pressure
PECS	Pulsed Electric Current Sintering
MA	Mechanical Alloying
MD	Molecular Dynamics
MIT	Massachusetts Institute of Technology
NC	Nanocrystalline
SAED	Selected Area Electron Diffraction
SEM	Scanning Electron Microscopy
STEM	Scanning Transmission Electron Microscopy
TEM	Transmission Electron Microscopy
UFG	Ultra-fine Grain
WHA	Tungsten Heavy Alloy
XRD	X-ray Diffraction

CHAPTER ONE: INTRODUCTION

Tungsten-based alloys have high strength and high density, which make them excellent candidates for kinetic energy penetrator (KEP) applications.[1] In order for an alloy to be effective as a KEP, it must be able to survive launch and impact. KEP properties must be tailored to optimize the combination of the material's hardness, resistance to abrasion and fracture toughness to maximize performance.[2] Tungsten heavy alloys (WHA) and depleted uranium (DU) are two systems currently being widely used as KEPs. DU is preferred due to enhanced ballistic performance[1, 3]; however, increased environmental concerns due to the low-level radioactivity of DU have promoted the current effort to find a WHA that can match the ballistic properties of DU.[4] It is the goal of this research to produce an amorphous tungsten alloy with suitable properties to replace DU KEPs. Ideal candidate alloys would have high strength, high toughness, and high resistance to abrasion to be considered replacements for existing KEP materials. A collaborative effort between Boise State University (BSU), Massachusetts Institute of Technology (MIT), and the Army Research Laboratory (ARL) was undertaken to develop the candidate alloys and characterize their mechanical properties and microstructure for use as KEPs.

Suitable WHA alloying elements have been found using molecular simulations and metallic glass forming principles. Emphasis was placed on the ability of the alloying elements to promote amorphous or nanocrystalline microstructures. Candidate elements were mechanically alloyed with tungsten using high-energy ball milling to promote mixing, reduce grain size, and promote amorphization. Consolidation of the candidate alloy powders was performed via pulsed electric current sintering (PECS). PECS uses a pulsed direct current to heat the specimen in an inert environment. This resistive heating can create higher heating rates (e.g., 100-200 °C/min) than conventional sintering techniques, which reduces the time needed for consolidation. This technique also provides excellent control of the processing parameters such a heating rate, dwell time, and pressure to reduce the overall time needed for consolidation. To avoid or reduce the grain growth of the nanocrystalline powders, high heating rates and short dwell times at low temperatures were used for consolidation.

After consolidation, candidate alloy compacts were evaluated to test their mechanical properties (Vickers hardness) and evaluate their microstructure. In parallel, collaborators at ARL are performing nano-indention, nano-compression, and ballistic testing of selected candidate alloys that showed high hardness and low porosity. Microstructural characterization included porosity measurements, grain size analysis, and phase determination.

CHAPTER TWO: BACKGROUND

2.1 Kinetic Energy Penetrators

Kinetic energy penetrators (KEP) are armor-piercing munitions for hardened targets. There are only two basic material systems used for this application: depleted uranium and tungsten heavy alloys. These materials have high densities (19.1 g/cm^3 and 19.25 g/cm^3, respectively), deliver high kinetic energy to a small area, and can penetrate armored targets. High yield strengths are required for a KEP to survive impact and high hardness is required to resist mass abrasion during penetration. Deformation behavior during penetration is different for WHA and DU depending on the alloying elements that are used in each. When a KEP undergoes stable plastic flow during penetration, a mushroomed head can develop, increasing the munitions' tip radius and therefore reducing the penetration depths achieved[3]; however, when early shear localizations occur, the deformed material is discarded and the munitions' tip becomes smaller and more pointed, increasing the ballistic performance of the KEP.[2]

2.1.1 Depleted Uranium

DU has been widely used for kinetic energy penetrators since the Gulf War of 1991.[4] DU KEPs perform better than WHAs because of their deformation behavior and therefore are preferred in most cases.[3] Some DU alloys undergo early shear localization deformation behavior during penetration, known as chiseling.[5] Two uranium alloys with chiseling deformation behavior are U-8Mo and U-0.75Ti (in wt.%).[2]

Two main health issues have driven the search for alternative materials systems: (1) large amounts of DU can enter the water supply after atmospheric corrosion of the used KEP occurs and (2) DU oxides can potentially be inhaled by surviving combatants as DU penetrates armor and generates aerosols or dust.

2.1.2 Tungsten Heavy Alloys

Tungsten heavy alloys have been studied extensively as a replacement for DU and are currently being used in some situations as KEPs. WHAs contain 60-98 wt.% tungsten and transition metals such as cobalt, iron, and nickel. W-Ni-Fe is one of the most commonly used WHAs, with Ni/Fe ratios between 2:1 and 4:1 providing optimal strength and ductility for use as KEPs.[6] Many other alloys have been developed to improve the performance of WHAs by varying compositions of the alloy and including other elements such as Al, Hf, Mn, Rh, or Ta. A complete review of WHAs used for KEP can be found in work by Cai *et al.*[1] The processing conditions of WHAs also have an impact on the strength, hardness, ductility, grain size, volume fractions of phases, and contiguity of the microstructure. To achieve full density, liquid-phase sintering is often done at temperatures ranging from 1400 °C to 1600 °C depending on the eutectic temperature of the alloy.[7] WHAs can reach near full density at temperatures significantly lower than bulk melting temperatures of the alloy. After liquid-phase sintering, a more rounded grain morphology is formed due to grain shape accommodation with the liquid-phase present [5], as seen in Figure 1.

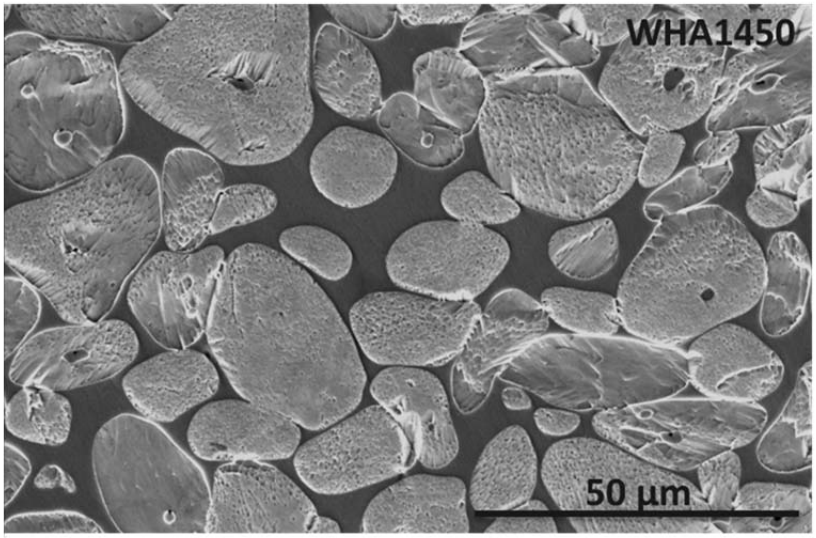

Figure 1 WHA (W-17Ni-2Co) processed by liquid-phase sintering. Pure tungsten particles are surrounded by a binder phase, mainly Ni and Co.

Liquid-phase sintering can reduce defects such as pores, which enhances the mechanical properties; however, it also leads to grain growth, which degrades the mechanical properties. Despite the relatively large grain size (20-60 μm), WHAs have yield strengths greater than 1 GPa and can have high ductility, ranging from 10-30%.[1] Both high strength and high ductility lead to high toughness, which is required for optimized performance. To improve the penetration depths of KEPs, several material properties are desirable: high strength, rapid thermal softening, low heat capacity, low strain-rate hardening, and work hardening.[2] These properties are required for beneficial deformation behavior such as novel-flow softening, which has been suggested to improve the KE penetration of WHAs.[3] These targeted properties can be altered by using different alloying elements in WHA and DU alloys.

2.2 Amorphous Metals

Amorphous metals have been studied extensively since the 1960s when researchers used rapid quenching from a melt to produce non-crystalline microstructures in Au-Si alloys.[8] The lack of long-range order in amorphous metals causes their properties to be unique, exhibiting similar elastic moduli to their crystalline counterparts but with increased strengths at room temperature.[9]

2.2.1 Amorphous Metal Glass-Forming Principles

Amorphous metals, often called metallic glasses, are formed on different principles compared to amorphous oxide glasses, to which Zachariason's principles apply.[10] One strategy to forming an amorphous metal relies on the ability to construct random packing through variation in the atomic radii of component elements. Efficient atomic packing, found in metallic glasses due to metallic bonding, causes specific ratios of solute and solvent atomic radii to occur. The efficient packing reduces the free volume in metallic glasses and densities near their crystalline counterparts are almost achieved. Ratios between the solute and solvent atomic radii for binary metallic glasses, higher-order metallic glasses and bulk metallic glasses have been compiled in work by Miracle *et al.*[11] Specific ratios were found that create metallic glasses and could be applied to other metallic systems to create a new amorphous metal.[12] Molecular simulations can also be applied that can help predict the potential of an alloy to become amorphous.

2.2.2 Amorphous Metal Processing

Amorphous metals can be produced via several processing techniques including mechanical alloying (MA), various casting techniques using cold molds, and melt-quenching techniques. All methods except MA have extremely high cooling rates that quench in the liquid microstructure. Melt quenching uses a metal wheel or mold, usually copper due to high thermal conductivity, that is cooled by water or liquid nitrogen, reaching cooling rates between 10^5 to 10^6 °C/s.[13] Using a spinning wheel, one can produce amorphous metallic ribbons with 2-5 mm width and thicknesses between 20-50 μm. Molds can also be made to cast amorphous alloys into near net shape parts. Depending on the glass formability of the alloy, typical cooling rates can be as low as 1-10 °C/s or higher than 10^4 °C/s.[14]

Mechanical alloying is discussed in Section 2.4.1. As a processing route to produce amorphous metals, mechanical alloying allows broader compositional ranges for amorphization compared to rapid-solidification processes.[15, 16] The broadening of the amorphous compositional range is due to an increase of free energy when defects are produced during mechanical alloying.[16] Even broader compositional ranges of binary amorphous alloys can be achieved using ion-beam mixing.[16] The entire compositional range can potentially be amorphized via solid-state techniques.[16]

2.2.3 Amorphous Tungsten

Amorphous tungsten alloys have been produced through the melt-quenching technique and were of interest in the late 1970s for their superconductivity at 3.45 to 4.55 K.[17] Tungsten alloys contained Ru and other components (P, B, and Si) to produce an amorphous microstructure.[17] The amorphous tungsten alloys had Vickers hardnesses between 11.2 to 15.0 GPa[17]. Similar compositions were studied in 2007; the glass transition temperatures (T_g) were between 1049-1298 K (776-1025 °C) and hardnesses were between 13.2 to 16.8 GPa.[18] $W_{46}Ru_{37}B_{17}$, produced by the single-roller melt-spinning technique, had room-temperature Vickers hardness of 16.8 GPa and hardnesses > 10 GPa at temperatures < 900 K.[19] WHAs typically have Vickers hardnesses between 2.5 – 4.7 GPa.[1]

Many amorphous tungsten and tungsten oxide specimens have been produced using thin-film techniques: electroplating [20, 21], electron-beam deposition [22], magnetron sputtering,[23, 24] and ion-beam mixing [25]. Specimen dimensions obtainable with these techniques are limited to thin films and cannot be scaled up to bulk dimensions needed for KEPs.

Amorphous tungsten powder has been produced by mechanical alloying with Ni[26]; however, consolidation via hot isostatic pressing was unsuccessful in retaining the amorphous phase while obtaining full densification.[27, 28, 29] The W-Ni alloy also had significant Fe pickup from the long milling times, 10-20 hours, needed to obtain the non-equilibrium amorphous phase in the powder.[30] Dynamic compaction was also used to consolidate the W-Ni amorphous powder, and while not fully dense or completely amorphous, the pore-free areas had Vickers hardnesses of ~13 GPa.[27] The high hardnesses seen in amorphous tungsten alloy ribbons and the W-Ni alloy produced with dynamic compaction show the hardness potential of WHAs if amorphous phases are present. Glass transition temperatures are important in understanding crystallization during consolidation of amorphous metals. [31, 32, 33, 34, 35]

2.2.4 Amorphous Metal Deformation

The disordered microstructure of metallic glasses also leads to different deformation modes when compared to crystalline metals. Amorphous-metal deformation is a high-energy process where local stresses induce atomic rearrangement of clusters of atoms [36, 37], often referred to as shear transformation zones.[38, 39] As these clusters of atoms deform, shear bands form at stress concentrations.[40] The shear band deformation mode is very useful in some applications such as KEPs where it promotes self-sharpening that can increase penetration depths over different failure modes.[1] Generally, amorphous metals deform through shear localization, which is a beneficial deformation mechanism for KEPs.[39]

2.3 Nanocrystalline Metals

Nanocrystalline materials have grain sizes on the nano-scale. This class of materials has been investigated heavily since 1989.[41] The nanoscale grain size alters the volume of grain boundaries and interfaces, which inherently alters the bulk mechanical properties.[42] Compared to larger-grained materials, nanocrystalline metals have increased hardness, toughness, compression strength, and resistance to abrasion.[41, 43, 44, 45, 46, 47, 48] Nanocrystalline metals have also be known to deform through shear band formation at high strain rates.[49]

2.3.1 Nanocrystalline Metals Processing

Nanocrystallline metals can be formed by many techniques including inert-gas consolidation, physical vapor deposition including evaporation and sputtering, plasma processing, chemical vapor condensation, chemical reactions, rapid solidification, electrodeposition, mechanical alloying and milling, devitrification of amorphous phases, spark erosion, and sliding wear.[50] Mechanical alloying requires powder consolidation to produce bulk specimens; this is one of the most common techniques to produce nanocrystalline metals and will be the focus of this study. Nanocrystalline refractory metals have been formed from amorphous or nanocrystalline powders.[51, 52, 53, 54] Often, unavoidable grain growth occurs in the consolidation of amorphous powder resulting in a composite structure consisting of both amorphous and nanocrystalline phases.[26, 34, 51, 55, 56, 57, 58, 59]

2.3.2 Nanocrystalline Tungsten

Nanocrystalline tungsten is of interest for use as a kinetic energy penetrator due to its mechanical properties and high density.[60] By reducing the grain size and bulk specimen dimensions of tungsten, very high strength can be achieved.[7, 60, 61, 62, 63] Previous studies have shown tensile strengths of 2.4 GPa for 300 μm diameter wires, 3.9 GPa for 20 μm diameter wires and up to 27 GPa for whiskers.[7] Fully dense nanocrystalline tungsten has been processed using high-pressure torsion at 500 °C and resulted in ~3 GPa quasi-static compression strengths;[63] however, the non-alloyed tungsten grains produced through this method were elongated and only had nanocrystalline dimensions in the width of the grains. Further improvement in properties by reducing grain size could likely be achieved through different processing and alloying.

Two methodologies have been used to successfully produce ultra-fine grain (UFG) and nanocrystalline (NC) tungsten: bottom-up and top-down. The top-down approach used to produce a fully dense tungsten alloy reduces grain size through severe plastic deformation such as high-pressure torsion.[60, 63] The bottom-up approach uses sub-micron starting powders of tungsten, which are then rapidly consolidated using resistive sintering under ultra-high pressure.[64] Specimens made this way had a grain size of 100 nm and microhardness of 10.87 GPa.[64]

2.3.3 Hall-Petch Relationship and Breakdown

In the late 1940's and early 1950's, two scientists, Hall [65] and Petch [66], established the same relationship between grain size and hardness in two different materials systems. Both found that as the grain size of a material was reduced, the strength of the material increased in a linear manner when the inverse root of the grain size was plotted against the strength. Increase in strength with decreasing grain size is caused by dislocation pile-up at grain boundaries. By reducing the grain size, there is an increase in the volume of grain boundaries as more obstacles are created for dislocations movement, resulting in increased yield strength of the material. This relationship does have a critical grain size at which the linear relationship breaks down; however, this breakdown is different for different materials systems. Typically, dislocations cannot remain in grains smaller than ~35 nm due to large distortions in the lattice and the Hall-Petch relationship breaks down.[67] At this point, the material will deform through grain-boundary sliding and the strengthening due to dislocation pile up is lost. Determining the grain size at which the break down occurs can be crucial to finding the maximum strength attainable in the material system.

2.4 Powder Metallurgy

A material's microstructure is largely controlled by the processing route.[42] Powder metallurgy is a solid-state processing route that can produce bulk materials with nanocrystalline and even amorphous microstructures. Specimen processing is a three-step route that involves starting with highly pure powders or powder alloys, mixing components based on desired composition and properties, then sintering the powders to consolidate to near-net shape parts.

The desired properties of an alloy are dependent on its constituent elements and can be tailored for a number of applications including KEPs. An improved alloy can be developed by carefully selecting alloying elements that will provide the best mechanical properties while maintaining high densities, which are required for KEPs.

2.4.1 Mechanical Alloying

Mechanical alloying is a technique that uses milling as a method to produce fully mixed alloy powder and even amorphous powder. Mechanical alloying can produce supersaturated solid solutions, intermetallic phases, quasi-crystalline phases, or amorphous alloys.[13] The selected powders are put into a vial along with spherical milling media and milled at high speeds, typically between 200-1000 RPM, causing collisions between the media and powder inside the vial. The collisions cause the powders to plastically deform, which leads to the formation of several types of defects such as dislocations, grain boundaries, surface defects, and stacking faults.[13] Increasing the milling intensity creates highly deformed microstructures and reduces grain size as milling time is increased.[67] Increasing the energy of the ball mill by increasing the milling RPM or ball-to-powder ratio (BPR) can promote mixing and reduce the time for amorphization to occur. The BPR ratios used to produce amorphous metallic alloys in several studies was at least 10:1.[13, 28, 68]

During milling, powders go through a morphological change as milling time is increased, as seen in WNi powder agglomerates studied at MIT (Figure 2). The initial laminar structure is coarse and becomes finer with longer mill times. After 10 hours, the WNi powder particles have lost the laminar structure. MA has been used to produce amorphous and nanocrystalline powders for many material systems: $Nd_{16}Fe_{76}B_8$ [37], NiW [66], $Ti_{50}Cu_{23}Ni_{20}Sn_7$ [67], $Fe_{52}Nb_{48}$ [68], W [69], and NiTi [69].

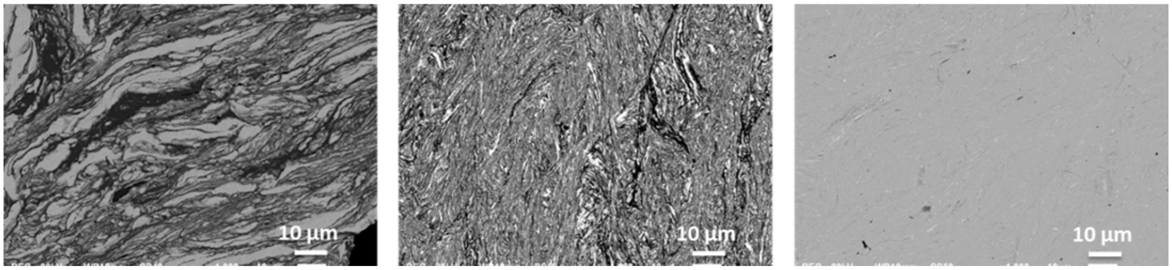

Figure 2 Powder morphology change in WNi alloy during milling for 1, 5, and 10 hours (left to right). Laminar structure is coarse at 1 hour becoming finer as milling time is increased. At 10 hours milling time, the powder appears to be completely mixed, though some defects can be seen from the high-energy milling. Contributed by Zachary Cordero.

2.4.2 Solid-State Amorphization

Solid-state amorphization can occur in alloys during high-energy ball milling. Molecular simulations of solid-state amorphization can help identify which alloying elements could produce amorphous or nanocrystalline tungsten through mechanical alloying.[15] Performing simulations of solid-state amorphization can suggest the best candidates, reduce the number of elements that are investigated experimentally, and ultimately save time and cost by avoiding elements that would perform poorly.

Simulations are composed of three steps in which elements are layered together, compressed from two parallel ends, and then cropped to form another square area. [15] This process is repeated until the system reaches a disordered state. The strain-and-stack simulation progresses through iterations and the potential amorphization of the alloy can be determined. Iterations are examined by the radial distribution function and the direct Fourier transformation produced by the atomic positions. The atomic radius mismatch is one of the most crucial factors in amorphization when ball milling. Other factors include crystal structure, heat of formation, and compositional range (discussed in section 2.4.1).

A large negative heat of formation has been suggested as the driving force for solid-state amorphization in the Au-La system; the large atomic size difference was also a contributing factor.[70] Other studies show that small negative heat of formation, such as in Ni-Mo, and even almost identical atomic radii and positive heat of formation, in Cu-Ta, can produce amorphous alloys through solid-state amorphization.[71, 72] Many binary systems show solid-state amorphization takes place with either positive or negative heat of formations; this criteria for the formation of amorphous alloys is still being discussed.[16]

2.4.3 Sintering

Sintering is a process to produce solid compacts from powder by increasing the temperature to levels where efficient mass transport and diffusion can occur.[73] Many different diffusion paths can be taken during sintering, such as surface, bulk, volume, or grain-boundary diffusion or even evaporation and condensation.[74] Sintering is traditionally divided into three stages: initial, intermediate, and final. Each stage has different characteristics that define what occurs as the powder particles evolve into dense solid compacts. The initial stage of sintering is when particles begin to form necks with other particles and pores become angular.[75] Neck formation is driven by the curvature of the particles, though this stage does not contribute to significant shrinkage.[76] The intermediate stage of sintering involves the shrinkage of pores and grain growth. Pores become rounded and form tubular networks on grain boundaries. Pore shrinkage occurs due to vacancy migration to annihilation sites such as grain boundaries and free surfaces.

The final stage of sintering is associated with pore localization and grain growth. Pores become localized at grain boundaries, especially triple junctions.[75] Rapid grain growth can occur in the final stage of sintering, which can trap pores inside grains. Diffusion mechanisms can be different for each sintering stage. The determination of which sintering mechanism is more prevalent can be difficult and is not the primary focus of this study.

Sintering methods are also divided into two categories: pressureless and pressure-assisted. Pressure-assisted sintering is more effective at creating near full density specimens [73], while pressureless sintering is sufficient for many applications like pottery and ceramics [77, 78]. There are many types of pressure-assisted sintering techniques, which include hot pressing [79], pulsed electric current sintering [80, 81, 82], super high-pressure sintering [83, 108], and hot isostatic pressing [84, 85, 86].

2.4.4 Pulsed Electric Current Sintering

Pulsed electric current sintering (PECS) is a relatively new technique that can produce nearly full density compacts in short times and lower temperatures, which can keep grain growth to a minimum.[87] PECS may be referred to by many different names listed in Appendix A, and though many different names are used, the process is the same; electric current, direct or alternating, is used for heating and uniaxial pressure is applied to assist the consolidation of specimen powder. Direct current can be constant or pulsing, typically below 1000 A, with low applied voltages, normally below 25 V.[87] Chamber atmosphere, typically inert gas such as Ar [87], can be varied to reduce corrosion during sintering; H is used to reduce oxides on the powders surfaces.[88] Graphite is mainly used for dies and punches due to its tolerance of rapid heating, but ceramics or steels can also be used.[87] Applied pressures during PECS are typically below 100 MPa, due to the mechanical strength of the graphite used.[87, 89, 90]

The combination of the electric current and the applied pressure can drastically reduce the time and temperature needed to sinter many materials systems.[91] Reduction in sintering time compared to hot pressing or hot isostatic pressing is seen in Si_3N_4 [92], Al_2O_3-$Y_3Al_5O_{12}$ [93], $Fe_{0.91}Mn_{0.09}Si_2$ [94], $Si_2N_2O_3$-CaO-Al_2O_3 [95], Y_2O_3-ZrO_2-ZrB_2 [96], Cr_2AlC [97], and hydroxyapatite powder [98]. Lower sintering temperatures have also been observed in Si_3N_4 [92], Al_2O_3-$Y_3Al_5O_{12}$ [93], $Si_2N_2O_3$-CaO-Al_2O_3 [95], Y_2O_3-ZrO_2-ZrB_2 [96], ZrB_2-$MoSi_2$ [99], and Nb/Nb_5Si_3.[100] Additionally, compared to hot pressing or hot isostatic pressing, PECS can provide finer microstructures [92, 93, 96, 101], more homogeneous microstructure [100], higher density [102], higher densification rate [99], improved mechanical properties [28, 97, 101, 103, 104, 105], improved electrical properties [106, 107], and improved bioactivity.[98] The improved properties seen when PECS is used make it an ideal processing route for the production of new materials for KEPs.

2.4.5 Pulsed Electric Current Sintering of Amorphous and Nanocrystalline Powders

Many sintering studies have been performed with amorphous and nanocrystalline powders consolidated with pulsed electric current sintering with little or no grain growth: $Fe_{48}Cr_{15}Mo_{14}Y_2C_{15}B_6$ [55, 109], $Al_{65}Cu_{20}Ti_{15}$ [56], $Cu_{47}Ti_{33}Zr_{11}Ni_6Sn_2Si_1$ [58, 107], NiTi [70], $Al_{88}Ni_6Ti_6$ [101], and $Zr_{57}Cu_{20}Al_{10}Ni_8Ti_5$.[106] The key to avoiding grain growth in consolidation of amorphous powders is to process the powders at temperatures below the crystallization temperature of the material and minimizing dwell time. The crystallization temperature of an amorphous material can be found using differential scanning calorimetry. Crystallization temperatures for many refractory metallic glasses containing 37-54 at.% tungsten are between 776-1025 °C.[18] After the crystallization temperature is exceeded in an amorphous alloy, grains begin to nucleate and grain growth occurs.[32, 33, 34, 35, 108, 109, 110]

CHAPTER THREE: EXPERIMENTAL

3.1 Mechanical Alloying

High purity tungsten (99.95%, Alfa Aesar, Ward Hill, MA, USA), chromium (99+%, Sigma-Aldrich Co. LLC, St. Louis, MO, USA), and molybdenum (99.9%, Sigma-Aldrich Co. LLC, St. Louis, MO, USA) powders were alloyed using a SPEX 8000 high-energy ball mill (SPEX SpecimenPrep, LLC, Metuchen, NJ, USA) at MIT. Initial powder size varied for each element: tungsten powder size was between 44 to 74 μm, molybdenum powder size was under 150 μm, and chromium powder size was under 44 μm. The alloy compositions to be processed were determined by molecular simulations at MIT. Chromium or molybdenum were added to tungsten in nominal amounts (10 at.% and 20 at.%) to keep a high final density. The high-energy ball mill was run at 1020 RPM in a glove box with an argon atmosphere. Powders were milled with 5:1 and 5:2 charge ratios (mass of media to mass of powder) for 10 and 20 hours, respectively. The vial was made of S5 steel, a shock resistant steel, and the media were E52100 carbon steel ball bearings with a 10 mm diameter. Additionally, tungsten was milled without Cr or Mo. Candidate alloys are labeled for the starting atomic concentrations of the metallic species before milling (W9Mo1, W8Mo2, W9Cr1, and W8Cr2). Tungsten milled without Cr or Mo is labeled W+.

3.2 Die Assembly

For PECS consolidation, two die sets were used, one with a 5.5 mm punch diameter and one with an 8 mm punch diameter, to vary the applied pressure during sintering (Figure 3). Isocarb I-85 graphite dies from Electrodes, Inc. (Largo, FL, USA), and AXF-5Q dies from POCO Graphite Inc. (Decatur, TX, USA) were used with compressive strengths of 138 and 150 MPa, respectively.[89, 90] Both of these die sets are made of high quality graphite, which allows for applied pressure during sintering, high temperatures, and repeated usage. TZM, a molybdenum alloy containing 0.5 at.% Ti and 0.08 at.% Zr (EagelAlloys, Talbott, TN, USA) was used for the 5.5 mm punches due to increased pressure attributed to the smaller radius. TZM is a particle-strengthened alloy that maintains excellent high-temperature tensile and compressive strength [111]. Temperatures with this die set were limited to below 1200 °C due to plastic deformation from the applied force of 5 kN.

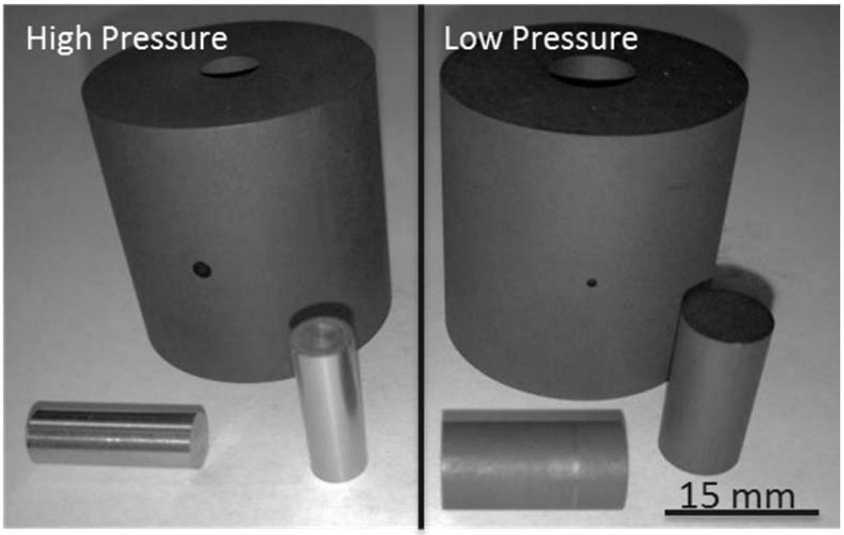

Figure 3 High-pressure 5.5 mm die set with TZM punches (left) and all-graphite low-pressure 8 mm die set (right). The thermocouple hole (left) and optical pyrometer black-body hole (right) can be seen in each die.

Graphite punches with a diameter of 8 mm allowed higher temperatures but lowered the allowable pressure from ~210 to ~100 MPa. The two die sets and specimens processed will be labeled after their pressure parameter as high pressure (HP) for the small diameter set and low pressure (LP) for the larger diameter set. Grafoil® (GrafTech International, Lakewood, OH, USA) was used as a gasket material between the powder and the cylinder walls of the die and the top and bottom of each punch. The flexible carbon foil was essential to avoid bonding of the powders with the die wall and for removing the specimen.

3.3 Pulsed Electric Current Sintering

Pulsed electric current sintering (PECS) was carried out in a Dr. Sinter SPS-515S (SPS Syntex Inc., Kanagawa, Japan) at the Center for Advanced Energy Studies (CAES) in Idaho Falls, Idaho. The 515S uses a 12:2 ms pulse ratio (ON: OFF) of direct current to heat specimens through resistance heating. Pressure and temperature profiles can be adjusted independently with the Chino KP1000 programmable controllers (Chino Corporation, Tokyo, Japan).

Alloy powders were loaded into the die assembly in a fume hood and pressed to 5 kN to form a green compact, 2 g for the HP die set and 4 g for the LP die set. Green compact densities were ~69-72% of the theoretical density calculated from the energy dispersive spectroscopy (EDS) compositional results. The die was wrapped in carbon felt to reduce heat loss and placed into the sintering chamber (Figure 4). Graphite spacers were used to avoid damage to the rams and center the die in the chamber. Tungsten carbide spacers were also used to reduce pressure on the graphite with the HP setup. After aligning the die into the center of the rams, the chamber was closed and evacuated

Figure 4 Sintering chamber die set up with felt wrapped around graphite die and tungsten carbide spacers (left). Pulsed electric current sintering machine at CAES in Idaho Falls, Idaho (right).

using a vacuum pump. Argon gas was used to purge the chamber three times and provide an inert low vacuum atmosphere during sintering. Low vacuum remained throughout the sintering process at pressures between 10-20 Pa.

A Chino IR-AH optical pyrometer was used to measure the temperature for the LP specimen series. After an initial 3 min ramp to 570 °C to reach the temperature range of the optical pyrometer, the heating rate for the LP die set was 100 °C/min. An Omega type-K thermocouple was used to measure the temperatures for the HP series. A heating rate of 100 °C/min was used for specimens consolidated for the HP die set. The minimum applied force during sintering was 5 kN and this was applied after die alignment in the sintering chamber. The applied force was held during the heating and dwell times then released after the dwell time was completed. Cooling was not controlled; the machine was water-cooled and temperature decreased initially at rates greater than 200 °C/min and then slowed to below 40 °C/min after 1-3 min. Typical heating and pressure profiles for the HP and LP series are shown in Figure 5.

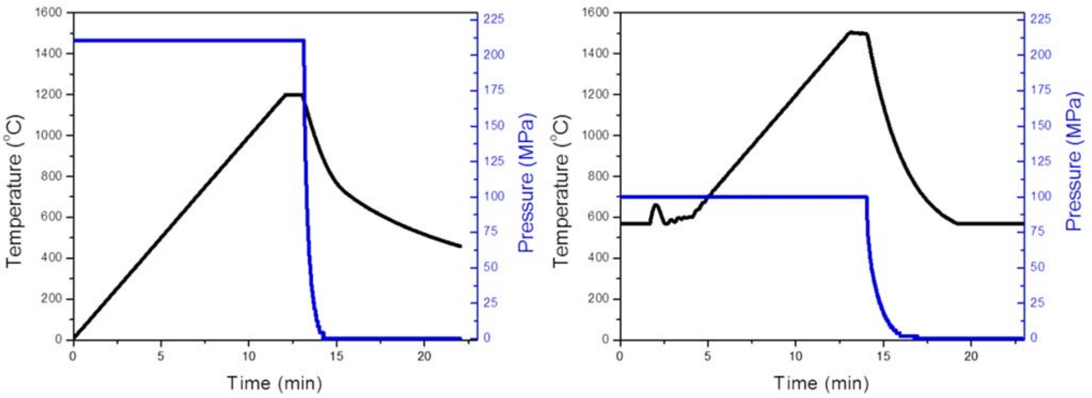

Figure 5 Typical heating and pressure profiles for HP (left) and LP (right) PECS. HP profile (left) heats to 1200 °C with 100 °C/min heating rate. LP profile (right) heats to 1500 °C with 100 °C/min heating rate after temperature of optical pyrometer is reached. Pressure is released after dwell time is completed.

Temperature and dwell time were varied to determine the best parameters for processing these new alloys for hardness, porosity, and grain size. Specimen matrices with consolidation temperature and dwell time for the HP and LP series are shown in Tables 1 and 2.

Table 1 HP specimen matrix for 1 min and 20 min dwell times.

HP Specimens	W+	W9Cr1	W8Cr2	W9Mo1	W8Mo2
1000°C 1min	2	2	2	1	2
1050°C 1min	0	1	1	1	2
1100°C 1min	2	1	2	2	2
1200°C 1min	1	1			

HP Specimens	W+	W9Cr1	W8Cr2	W9Mo1	W8Mo2
1000°C 20min	1	1	2	1	2
1100°C 20min	1	1	1	1	2

Table 2 LP specimen matrix for 1 min and 20 min dwell times.

LP Specimens	W+	W9Cr1
1100°C 1 min	1	1
1200°C 1 min	1	1
1300°C 1 min	1	1
1400°C 1 min	1	1
1500°C 1 min	1	1
1600°C 1 min	0	1
1700°C 1 min	0	1

LP Specimens	W+	W9Cr1
1100°C 20 min	1	1
1200°C 20 min	1	1
1300°C 20 min	1	1
1400°C 20 min	1	1

The die set was removed from the sintering chamber when the temperature was below 300 °C and placed on a metal surface to cool further. The specimen was removed from the die with a hydraulic press and spare punch and placed into a labeled specimen container.

3.4 Specimen Preparation

After consolidation, each specimen was ground with SiC grit paper to remove the carbon layer left from Grafoil® on the specimen's outer surface. Sectioning of the consolidated specimens was performed using a TechCut 4™ (Allied High Tech Products Inc., Rancho Dominguez, CA, USA) low-speed saw with a high-concentration diamond blade. After sectioning, part of the specimen was mounted in KonductoMet® (Buehler, Lake Bluff, IL, USA) conductive phenolic mounting compound with a SimpliMet® 1000 (Buehler) automatic mounting press. Consolidated specimens were prepared for stereology using Buehler SiC grit polishing paper from 120 to 800 grit then polished with LECO® (LECO, St. Joseph, MI, USA) 1 μm alumina slurry. Final polishing was completed in a VibroMet® 2 (Buehler) vibratory polisher at amplitudes between 20-30% for 3 hours with a 0.05 µm MasterPrep® (Buehler) alumina polishing suspension.

Powder scanning electron microscopy (SEM) specimens were prepared by suspending < 0.5 g of powder in 5 mL of methanol. The suspension was then agitated for five min in an ultrasonicator. After sonication, a drop of suspension was place on an SEM stage with double-sided carbon tape and allowed to dry for 15- 20 min. Once the suspension completely dried, compressed air was used to blow off any loose particles remaining on the surface. Specimens were imaged immediately after preparation.

Powder cross-section SEM specimens were prepared by mixing alloy powder and mounting powder. The mixture was poured into a small-diameter washer to confine the particles during mounting, which was conducted as described above. The specimen was then polished using steps described for consolidated specimens except vibratory polishing.

TEM specimens were prepared by polishing a thin disc to approximately 20 µm with a Model 623 Disc Grinder (Gatan, Inc., Pleasanton, CA, USA). Specimens were then mounted with epoxy onto a copper disc with a 1 by 2 mm hole. Next, the specimen was thinned further with the disc grinder to below 5 µm. Final thinning was performed using a Model 691 Precision Ion Polishing System (Gatan, Inc., Pleasanton, CA, USA) at 5 keV with an angle of 6° for several hours until perforation. Once the hole in the specimen formed, the specimen was removed and analyzed or stored in a vacuum desiccator to avoid any surface oxidation prior to imaging.

3.5 Analysis Techniques

The consolidated specimens were analyzed via Vickers hardness tests, Archimedes-principle density determinations, SEM micrographs, scanning transmission electron and transmission electron micrographs, EDS in SEM and STEM, x-ray diffraction and quasi-static compression. These methods were used to determine the hardness, density, porosity, composition, crystallite size, and compression strength of the consolidated specimens.

3.5.1 Vickers Microhardness

A DM-400FT (Leco Corp., St. Joseph, MI, USA) microhardness tester was used to determine the hardnesses of all specimens after polishing. Five random indents were made on each specimen with a diamond-pyramid indenter set at 1 kg for 15 s. The indent diagonals were measured and averaged. Eq. (1) was used to calculate the hardness, where *F* is the force applied in kilograms, *d* is the average diagonal width of the indent in millimeters, and 1.8544 is the diamond indenter constant.

$$HV = \frac{1.8544\,F}{d^2} \tag{1}$$

Hardness was plotted versus the dwell temperature of the specimens and compared against the two baseline tungsten alloys. Hardnesses were also used to create a Hall-Petch relationship between the inverse root grain size and the hardness.

3.5.2 Archimedes Principle

Archimedes principle is a method to accurately determine the density of a material based on its weight in and out of water. The density of each consolidated specimen was determined, after removing Grafoil®, using the ASTM B311-93 water-displacement method.[112] A density measurement kit and AB-54S/Fact digital analytical scale (Mettler Toledo Inc., Columbus, OH, USA) allowed accurate density measurements with estimated errors below 0.005 g/cm^3. Each specimen's weight was measured five times, in and out of water, to determine the density, and then an average density was calculated.

3.5.3 Scanning Electron Microscopy

Secondary electron imaging of powders and consolidated specimens was completed using an S-3400N-II (Hitachi Ltd., Tokyo, Japan) analytical scanning electron microscope, operated at 30 kV. Micrographs were taken of the polished specimen surfaces and used for porosity measurements and phase fraction percentages. Five selected SEM micrographs of each specimen, taken at 1000 magnification, were converted into black-and-white images using MATLAB (Figure 6). By carefully selecting the threshold of each image, the porosity was calculated from the fraction of black and white pixels. The threshold of each image was analyzed to avoid including the intermetallic phase in the porosity measurement.

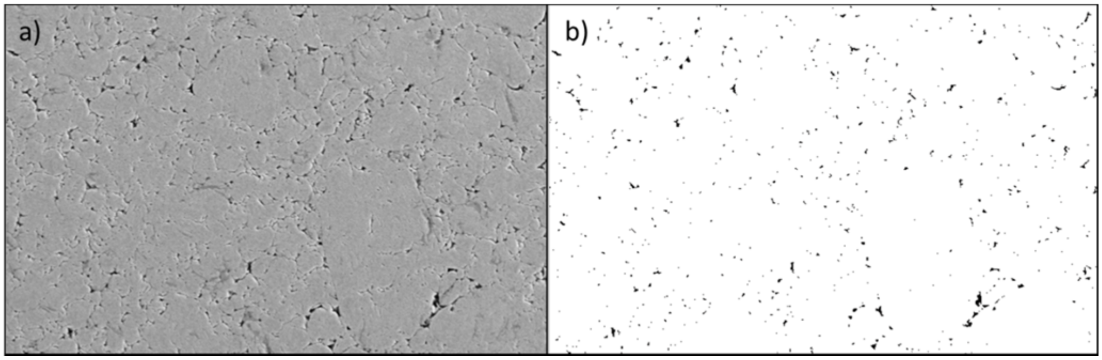

Figure 6 Example of image analysis to calculate the porosity of consolidated specimens using MATLAB, a) original SEM micrograph and b) binary image.

Energy dispersive spectroscopy (EDS) was performed on powders and consolidated specimens to understand any compositional separation that might occur during the sintering process. EDS was optimized for dead times of 30-40% and compositional optimization on copper tape preceded any compositional analysis of specimen alloys. The probe size for spot scans is approximately 1μm for SEM EDS. Quantitative analysis of the EDS spectra was completed by INCA Software, which uses the intensities of the peaks along with a coefficient based on the atomic number, absorption, and fluorescence of the x-rays in the specimen.

3.5.4 Grain Size Analysis

An average grain size was calculated using the line intercept method on SEM micrographs of the consolidated specimens. The ASTM standard E112-96 test method for determining average grain size was used.[113] Two SEM micrographs of the selected specimens were used. Each SEM micrograph had 15 lines measured and the number of grain boundaries crossed by each line was counted. Similar grain size analysis was performed at MIT with a measured circle and the number of grain boundaries crossed was counted.

3.5.5 Transmission Electron Microscopy

A JEM-2100 HR (JEOL Ltd., Tokyo, Japan) analytical transmission electron microscope was used to verify the nanocrystalline microstructure in select consolidated specimens. Specimens were analyzed using an accelerating voltage of 200 kV. Analysis was performed in transmission and scanning transmission mode for both high-resolution micrographs and analytical measurements. Selected-area diffraction patterns of the specimens were taken to analyze the crystallographic structure of the alloys and compared to x-ray diffraction data. Compositional measurements were performed in the scanning transmission mode with a typical probe size of 2-10 nm depending on the magnification. Quantitative analysis of the STEM-EDS spectra was completed with Thermo Scientific software, which utilizes the Cliff-Lorimer ratio and the peak intensities.

3.5.6 X-ray Diffraction

X-ray diffraction was used on all powders and consolidated specimens to determine crystallographic structure. An AXS D8 Discover (Bruker, Inc., Madison, WI, USA) x-ray diffractometer was used in point detection mode from 20-100° 2θ, with a 0.02° step size. The diffractormeter uses a Cu K_α x-ray source with a characteristic wavelength of 1.5418 Å. Scherrer's formula was used with x-ray diffraction data to estimate the crystallite size[114], Eq. (2), which is a function of the full peak width at half maximum, β, Scherrer's constant, K, x-ray wavelength, λ, and Bragg angle, θ:

$$Crystallite\ Size = \frac{\mathrm{K}\lambda}{\beta\ Cos\ \theta} \tag{2}$$

Additionally, the lattice parameters, a, of the powders and consolidated specimens were calculated using the miller indices (h, k, l) of the (110) plane, and d-spacing, d, using Eq. (3) and Eq. (4):

$$a = d\sqrt{h^2 + k^2 + l^2} \tag{3}$$

$$d = \frac{\lambda}{2\sin\theta} \tag{4}$$

3.5.7 Williamson-Hall Technique

The Williamson-Hall technique was used to determine the crystallite size of milled powders.[115] The broadening of x-ray diffraction peaks is due to the small crystallite size and strain in the powders after mechanical alloying. The strain and crystallite size can be estimated with a Williamson-Hall plot using Eq. (5), which is a function of the full peak width at half maximum, β, x-ray wavelength, λ, Bragg angle, θ, and the strain in the material, ε:

$$\frac{\beta\cos\theta}{\lambda} = \frac{1}{D} + \frac{4\varepsilon\sin\theta}{\lambda} \tag{5}$$

By plotting β cos θ/ λ vs. sin θ/ λ for multiple reflections and using a linear fitting of the data points, the crystallite size can be calculated, from the y-intercept, and the average strain in the material from the slope.

3.5.8 Lattice-Parameter Determination

X-ray diffraction peaks, (200) and (211), were used for lattice-parameter calculations and compared against Vegard's Law.[116] Vegard's Law states that the lattice constant of alloy, a_{AB}, is dependent on the atomic concentrations, *[A]* and *[B]*, of the constituent elements, Eq. (6):

$$a_{AB} = a_A * [A] + a_B * [B] \tag{6}$$

d-spacings were calculated using Bragg's Law (Eq. 4) by taking the peak angle, *θ*, and finding the *d*-spacing, *d*, of the selected peak using the known x-ray wavelength, *λ*. XRD spectra were used to determine the crystallographic structure of the alloys by indexing peaks and the lattice parameter was then calculated using the *d*-spacing, *d*, and the Miller indices of the corresponding plane (Eq. 3).

3.6 Baseline Kinetic Energy Penetrator Materials

Two baseline materials, supplied by the ARL, were used to compare with the mechanical properties of the candidate alloys: wrought tungsten and WHA1450, Figure 7. Wrought tungsten has been heavily worked to reduce grain size and improve mechanical properties. WHA1450 is a tungsten heavy alloy containing Ni and Co for a binder phase. WHA1450 is processed by liquid-phase sintering and has a two-phase microstructure as seen in Figure 7. Pure tungsten particles (light gray and circular) are surrounded by a W/Ni/Co phase (dark gray). The hardnesses of these alloys will be compared to specimen materials produced in this study.

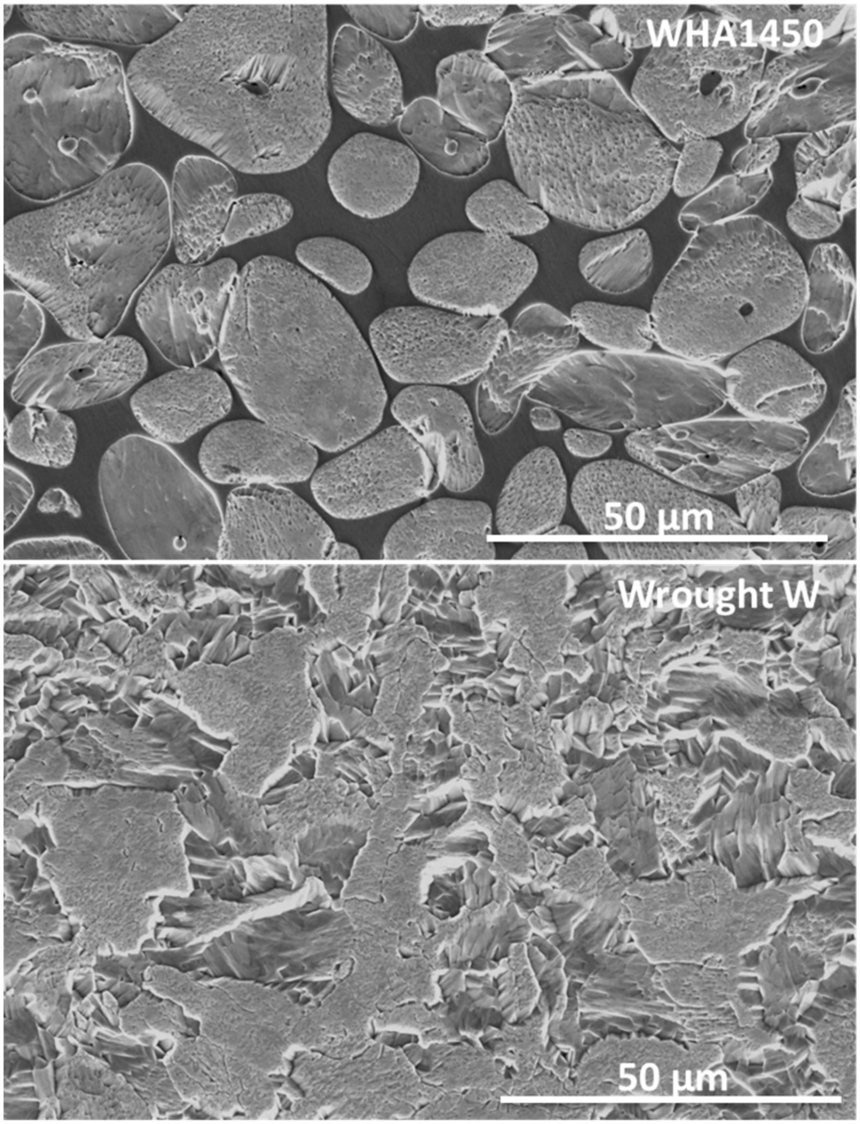

Figure 7 SEM micrographs of two baseline tungsten alloys used for mechanical property comparison in this study. WHA1450 (top) and Wrought W (bottom).

CHAPTER FOUR: RESULTS AND DISCUSSION

4.1 Powder Analysis

The W+, W9Cr1, W8Cr2, W9Mo1, and W8Mo2 powders were analyzed after high-energy ball milling to determine the composition and crystallite size prior to consolidation. High charge ratios and long milling times were necessary to produce powders that had nanocrystalline microstructures; however, a consequence of long milling times and high charge ratios was increased media incorporation, especially iron from the hardened steel media, into the powder. Media wear has been known to occur when milling tungsten to promote amorphization in high-energy ball mills.[30] Iron incorporation was analyzed using SEM with energy dispersive spectroscopy (EDS) on the powders; the pickup varied from 6-15 at.% (Table 3). EDS spectra for W9Mo1 and W+ powders are shown in Figure 8. In general, the iron was incorporated homogenously throughout the powder particles; however, some areas of unmixed iron were found and could be from chipping of media (Figure 9). All powders milled for 10 hours were used for HP specimens, and all powders milled for 20 hours were used for the LP specimens.

Table 3 Powder composition measured by EDS in at.% for candidate alloys milled for 10 and 20 hours, estimated error +/- 0.5 (at.%).

Element	W+ 10 hr	W+ 20 hr	W9Cr1 10 hr	W9Cr1 20 hr	W8Cr2 10 hr	W9Mo1 10 hr	W8Mo2 10 hr
W	88	90	84	84	71	77	70
Fe	12	10	6	9	12	15	13
Mo	-	-	-	-	-	8	17
Cr	-	-	10	7	17	-	-

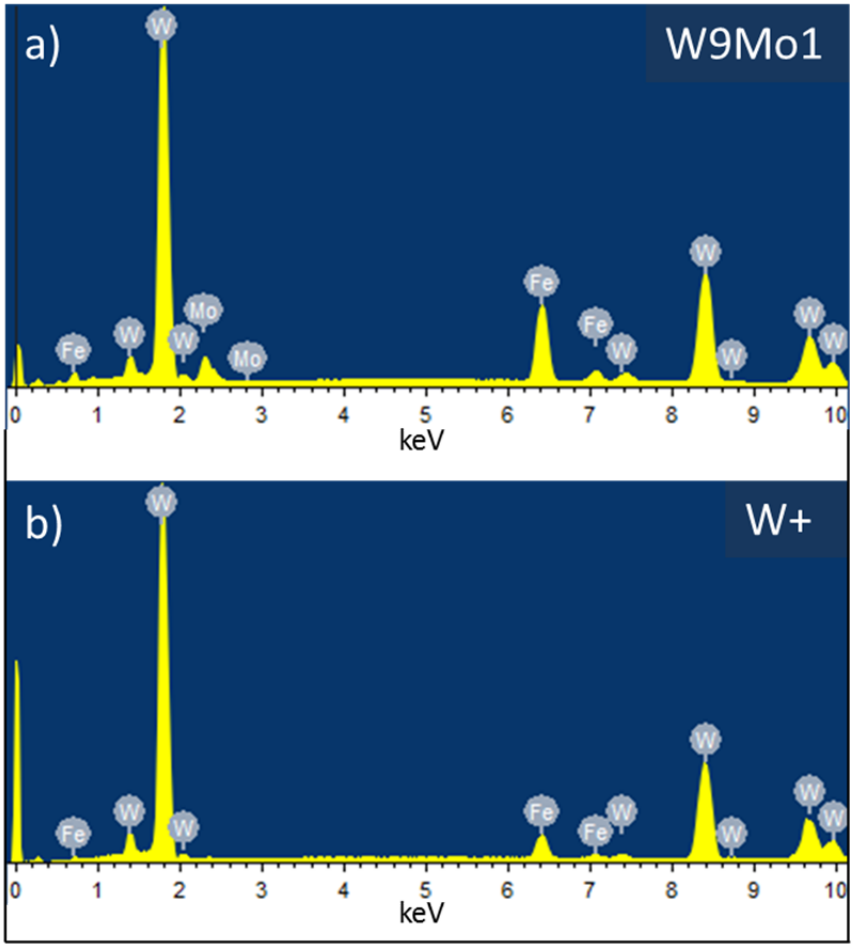

Figure 8 SEM EDS spectra for a) W9Mo1 and b) W+ powders.

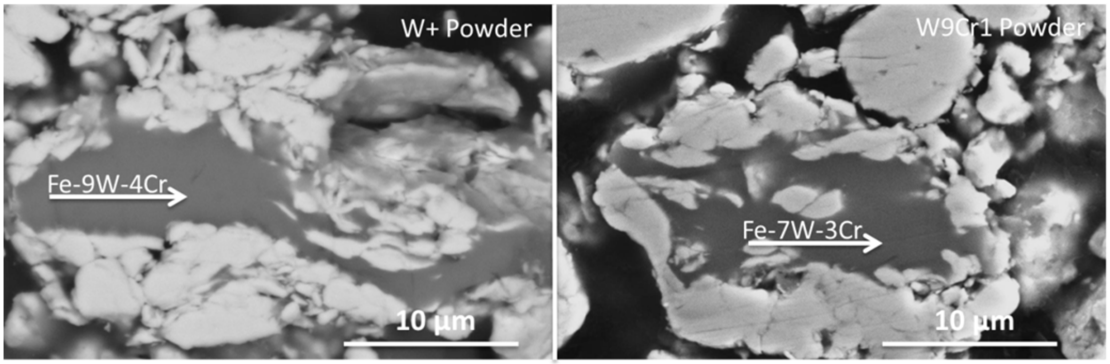

Figure 9 Non-mixed iron in powder particles, W+ (left) and W9Cr1 powder (right). Darker gray regions, pointed out by the white arrows, contained 87-90 at.% Fe and 3-4 at.% Cr, as determined by EDS.

Since the high-energy ball milling resulted in alloying W even without additional alloying elements, it is important to examine the binary phase diagram for the W-Fe system. The binary phase diagram for the W-Fe system is presented in Figure 10. The initial powder composition is shown as a black line and is labeled on the diagram. The W+ initial composition, W-12Fe, is in a two-phase region with a W solid solution and an intermetallic phase ($W_{5.1}Fe_{7.9}$), also known as a μ-phase. Multiple binary systems can form a μ-phase including W-Fe, Mo-Fe, Mo-Co, W-Co, Ta-Co, Nb-Fe, Nb-Zn, Ta-Fe, Nb-Ni, Nb-Co, and Ta-Ni.[117] The μ-phase is considered detrimental when it precipitates as it is a hard-brittle intermetallic phase, which can deplete strengthening elements out of the bulk.[117] The initial powder is at a composition that is not in equilibrium due to the high-energy ball milling. The solubility limit for Fe in the equilibrium W solid solution is less than 4 at.%. It would be expected that the two equilibrium phases would begin to develop out of the initial composition of the bulk as the powders are processed.

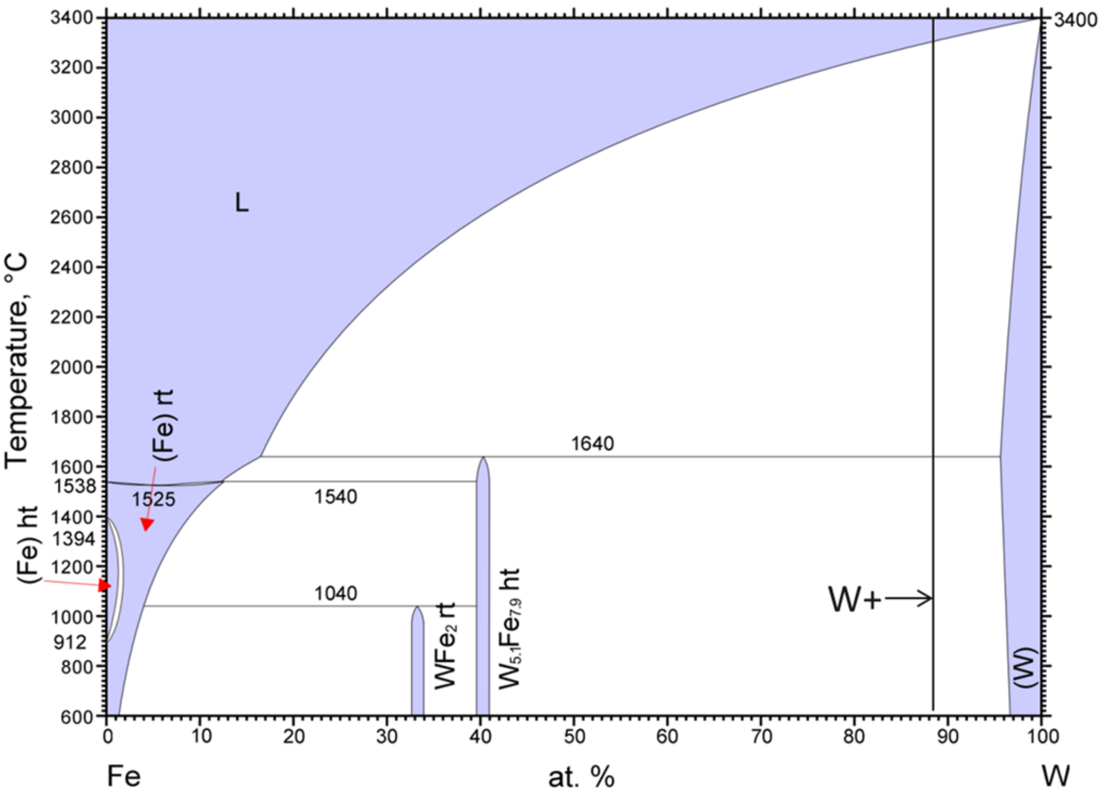

Figure 10 Binary phase diagram for the W-Fe system.[118] Initial powder milled for 20 hrs has a composition of W-12Fe, shown as a black line. Reprinted with permission of ASM International. All rights reserved.

Due to the Fe pickup from the milling of WCr and WMo alloys, it is necessary to examine the ternary phase diagrams for these alloys. The ternary phase diagram for W-Cr-Fe at 1100 °C is presented in Figure 11. The W9Cr1 (W-7Cr-9Fe) and W8Cr2 (W-17Cr-12Fe) initial compositions are marked on the ternary phase diagram. The WCr alloys are in a two-phase region consisting of a W solid solution and an intermetallic μ-phase, labeled $W_{5.1}Fe_{7.9}$. Separation towards the two equilibrium phases is expected during the processing of these compositions.

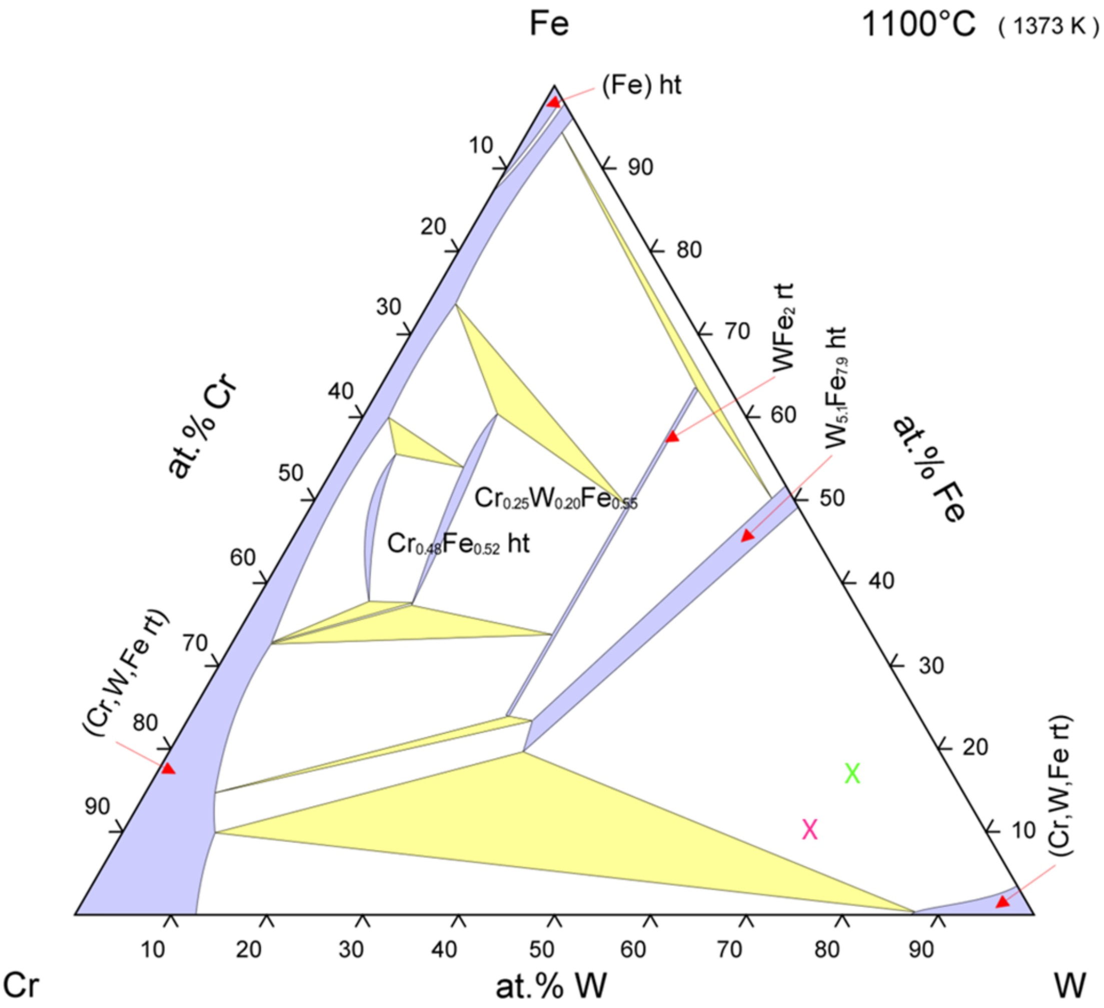

Figure 11 Isothermal section of the ternary phase diagram for the W-Cr-Fe system at 1100 °C.[119] Initial powder compositions of W9Cr1 (green X) and W8Cr2 (magenta X) are marked. Reprinted with permission of ASM International. All rights reserved.

The ternary phase diagram for W-Mo-Fe at 900 °C is presented in Figure 12. The W9Mo1 (W-8Mo-15Fe) and W8Mo2 (W-17-Mo-13Fe) initial compositions are marked on the ternary phase diagram. The WMo alloys are in a two-phase region consisting of a W solid solution and an intermetallic μ-phase, labeled $W_{5.1}Fe_{7.9}$ and $Mo_{5.1}Fe_{7.9}$. Molybdenum and tungsten are fully soluble as an alloy but have a low solubility for Fe, ~2 at.%. The composition of the WMo alloys should separate into the two equilibrium phases, a W solid solution and the intermetallic μ-phase.

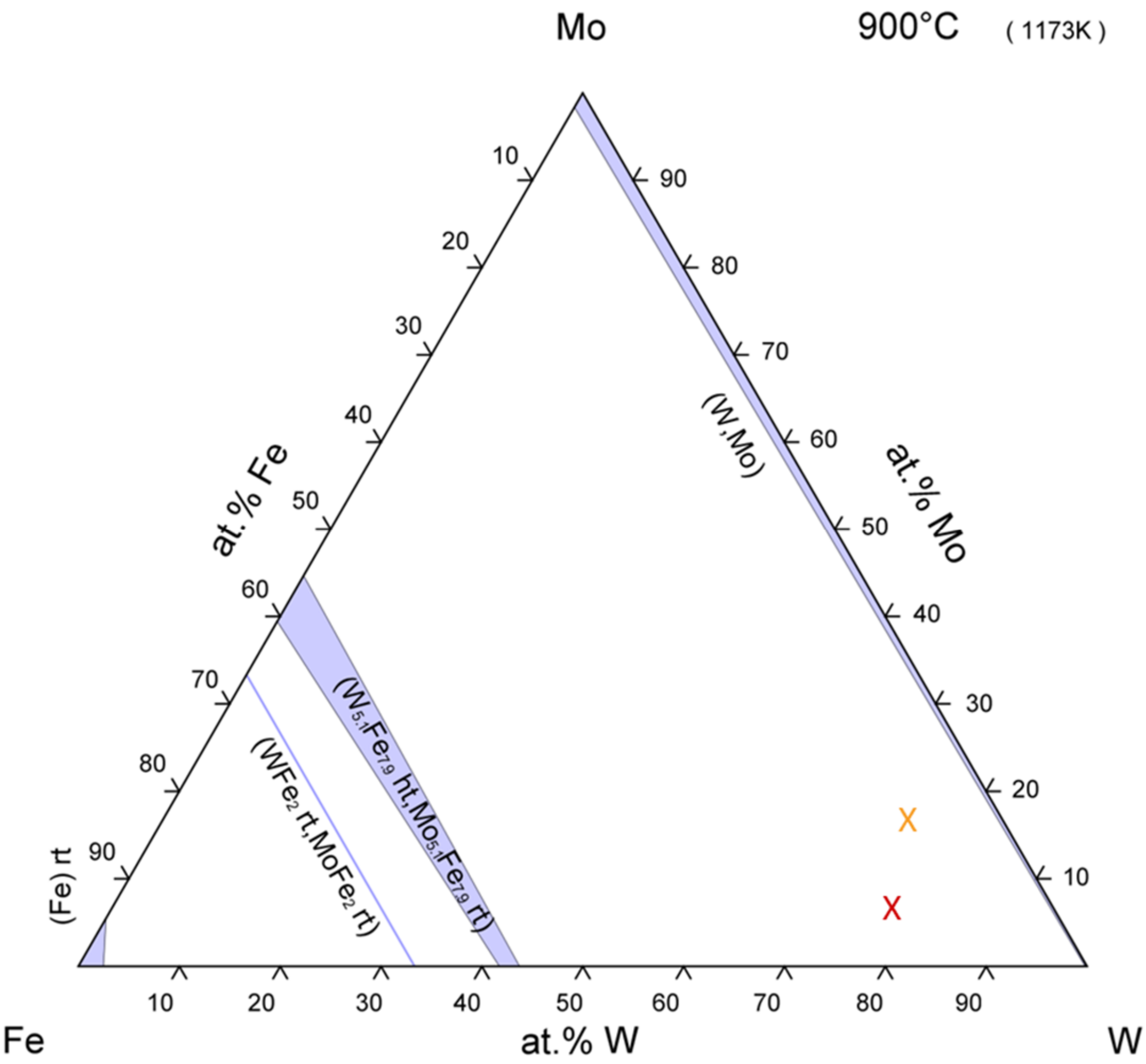

Figure 12 Isothermal section of the ternary phase diagram for the W-Mo-Fe system at 900 °C.[120] Initial powder compositions for W9Mo1 (red X) and W8Mo2 (orange X) are marked. Reprinted with permission of ASM International. All rights reserved.

The powder crystallite size was measured with the Williamson-Hall technique from XRD data at MIT; the crystallite sizes are shown in Table 4, along with the mean particle diameter calculated by laser scattering. Select SEM micrographs of the W9Cr1 and W8Cr2 powders show that the particle size varied compared to the laser scattering method and particles greater than 20 μm in width can be seen (Figure 13).

Table 4 Crystallite size and mean particle diameter for initial powders.

Alloy	Crystallite size (nm)	Powder Particle Mean Diameter (μm)
W+	31	6.7
W9Cr1	13	6.6
W8Cr2	13	-
W9Mo1	15	6.5
W8Mo2	13	-

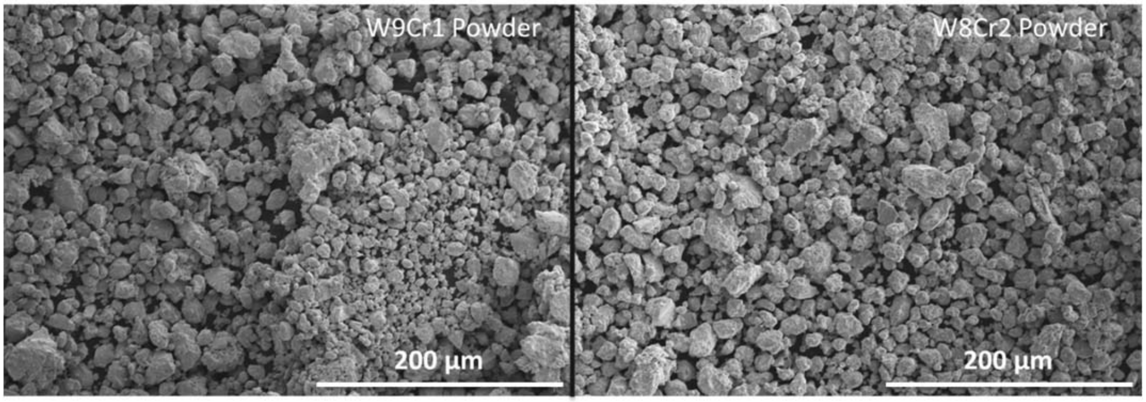

Figure 13 SEM micrographs of W9Cr1 and W8Cr2 powders milled for 20 hours at a 5:2 charge ratio.

The estimated crystallite size for tungsten alloyed with Cr or Mo was below 15 nm for all compositions. The milled tungsten with only media incorporation for alloying had an estimated grain size of 31 nm. The nanocrystalline microstructure was validated in TEM powder studies at MIT. The TEM micrograph in Figure 14 of W9Cr1 shows grain sizes below 40 nm and shows the highly deformed nature of the powder particles.

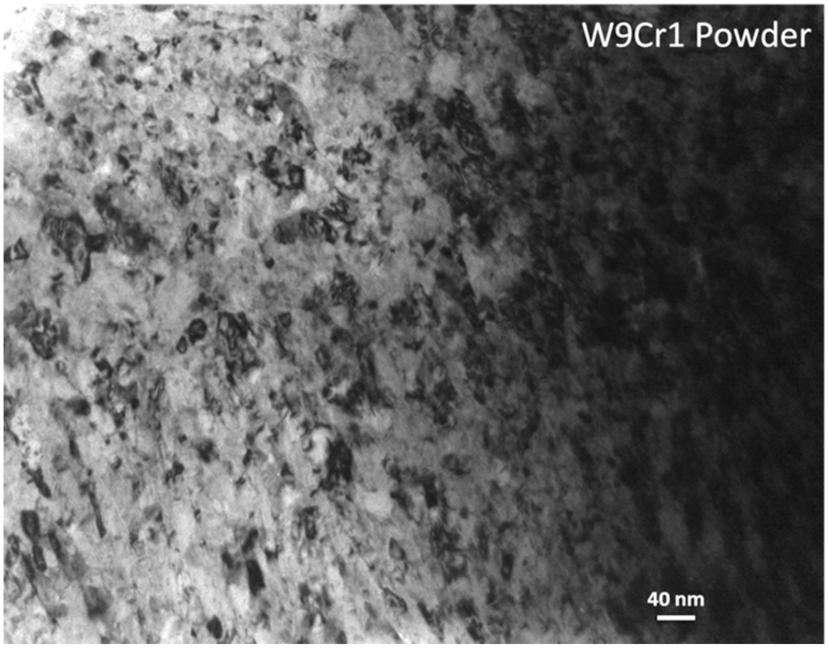

Figure 14 TEM micrograph of W9Cr1 powder. Contributed by Zachary Cordero.

4.2 Density of Consolidated Alloys

The densities of the alloys after consolidation are given in Figure 15. Density increased with increasing dwell temperature for HP specimens. Specimen densities were all below those of pure W and depleted uranium, 19.25 and 19.1 g/cm^3, respectively. The WMo alloys had higher densities than WCr, which is expected due to alloying with a higher-density element. For specimens sintered for 1 min, W+ had the highest density due to its composition. Density overlap between 1 and 20 min dwell time for W9Mo1 and W8Mo2 specimens consolidated at 1100 °C can be seen and suggests that these alloys reached full density due to the lack of additional improvement in density with increased dwell time.

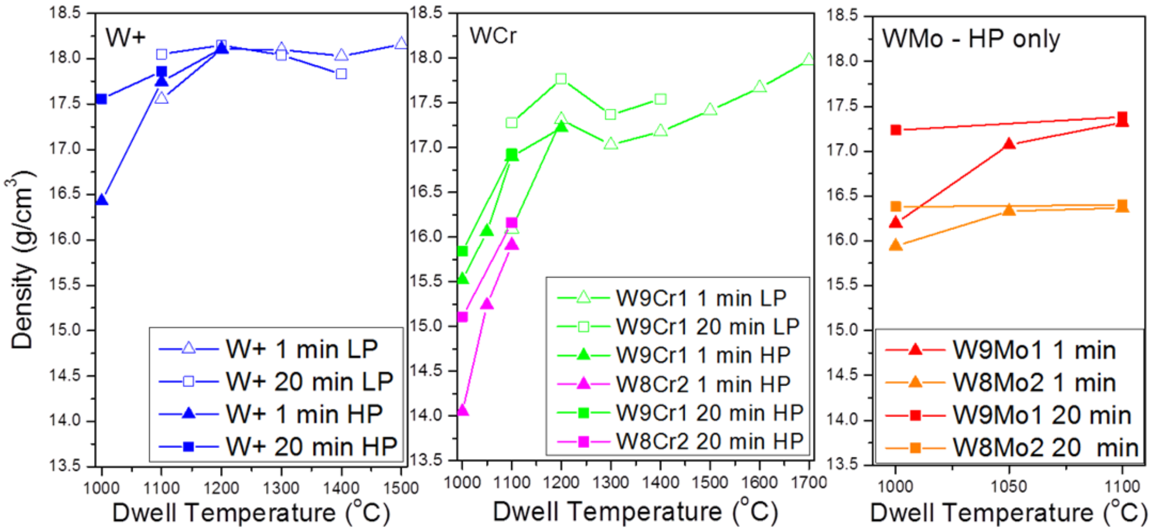

Figure 15 Densities of W+, WCr, and WMo alloys. Density overlap in 1 and 20 min specimens seen in W8Mo2 and W9Mo1 suggests complete densification occurred at 1100 °C.

The density of both W+ and W9Cr1 increased from 1100 °C to 1200 °C for both 1 and 20 min dwell times. In the LP specimens, density slightly decreased for W9Cr1 from 1200 °C to 1300 °C, and then increased from 1300 °C to 1700 °C. At 1700 °C, the density of W9Cr1 was similar to that of the W+ alloy. The increase in density is due to a compositional change that occurred as some of the material is pressed out of the bulk, as discussed in detail in Section 4.5.4.

Density increased from 1100 °C to 1200 °C in both 210 MPa and 100 MPa pressure consolidations for W+ and W9Cr1 alloys (Figure 15). Overlap of density for consolidation at 1200 °C for 1 and 20 min dwell time suggests that full densification occurred at this temperature for both 100 MPa and 210 MPa consolidation pressures. The increased pressure does not affect the density at 1200 °C; however, at 1100 °C, the increase in pressure increased the density of both W+ and W9Cr1. The increased pressure can be beneficial to sintering by directly effecting particle re-arrangement and by destroying agglomerates, which may be present in the powder.[121] The pressure effects are also dependent on the powder particle size; Skandan *et al.*[122] reported no pressure effect for 6 nm zirconia powders until above 35 MPa, at which point density increased sharply when sintered at 950 °C. Increasing the zirconia particle size to 12 nm, the sharp increase in densification was seen at 10 MPa.[122] This increase in density as a result of increased applied pressure is dependent on the material and varies with particle size. The particle size and uniformity was not varied in this study and the effect of additional pressure resulted in increased specimen density mainly by enhancing particle re-arrangement and destroying agglomerations during the initial stage of sintering. Near full densification, the particles have transformed into grains and the additional pressure showed no effect on the density. Specimen densities were in line with other WHAs, which range from 16.2 – 18.6 g/cm^3.[1] The absolute density of these alloys is one of the most important factors for KEPs to be able to deliver the most kinetic energy to the target. The relative densities of these alloys are not presented due to variation in compositions and phase fractions; the porosity measurements of these alloys can be used to determine whether the specimens reached their theoretical density.

4.3 Porosity

Image analysis, as discussed in Section 3.5.3, was performed on the SEM micrographs of the consolidated specimens to calculate the porosity. Average porosities as a function of dwell temperatures are shown in Figure 16 for W+, WCr, and WMo specimens. Overall, WMo alloys had lower porosities than WCr alloys. In the W9Mo1 alloy, consolidation at 1100 °C for 1 min dwell time produced a specimen with negligible porosity. In the W8Mo2 alloy, negligible porosity was found at 1050 °C with 1 min dwell time. W8Cr2 had the highest porosity of all alloys in the HP specimen series. Increasing the temperature or the dwell time reduced the porosity of all the HP alloys. In the LP specimens, all porosities were below 3%. All alloys had negligible porosity at a consolidation temperature of 1200 °C (Figure 16). Specimen porosity increased above 1200 °C in all LP alloys, up to 1% for W9Cr1 consolidated at 1700 °C for 1 min. The increase in porosity at dwell temperatures above 1300 °C was unexpected and is discussed in detail in Section 4.5.4.

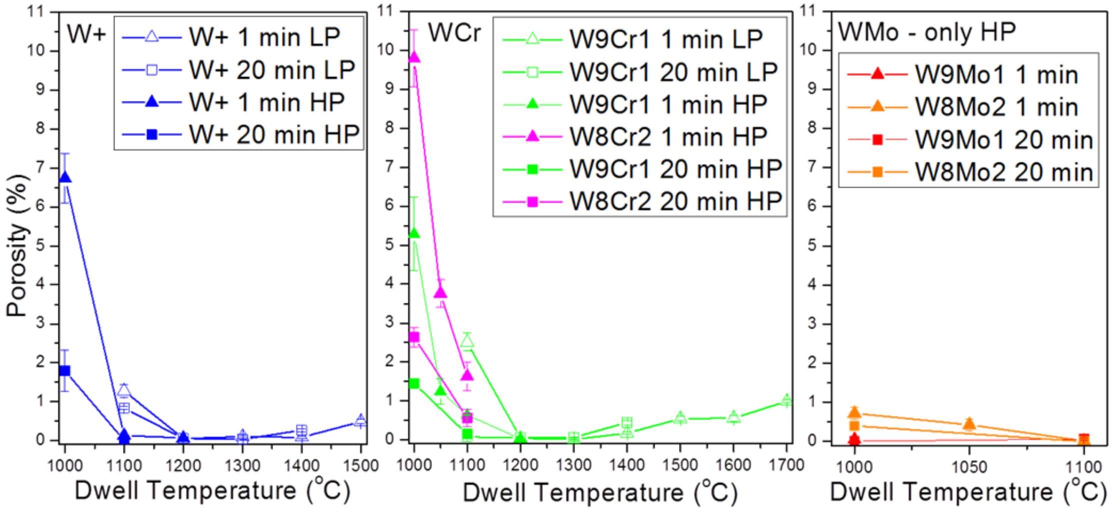

Figure 16 Calculated porosities for W+, WCr, and WMo alloys.

Increasing the pressure of consolidation from 100 MPa to 210 MPa reduced the porosity in W+ and W9Cr1 consolidated at 1100 °C. All W+ and W9Cr1 specimens consolidated at 1200 °C for both 100 MPa and 210 MPa showed negligible porosity. Increased pressure during consolidation is beneficial at 1100 °C; however, increasing the pressure at 1200 °C is not beneficial to reducing porosity and resulted in similar porosities for applied pressure of 100 MPa and 210 MPa during consolidation.

In both W+ and W9Cr1, the increased pressure resulted in lower porosities at 1100 °C. The porosity is improved at the lower temperatures in the same manner as the density is increased, discussed in Section 4.2. The increased pressure was only achieved by using smaller specimen dimensions, which required advanced materials and pushed the mechanical limits of the material. Processing at the limits could make it difficult to scale up specimen size while retaining the increased pressure of 210 MPa. Increasing the pressure further could be possible with an elaborate die set and may improve the hardness and lower porosities, but the specimen size would most likely remain small.

The high porosities seen in the WCr alloys could be the result of increased activation energy of sintering when W is alloyed with Cr. Studies performed on WC, with a binder containing Ni and Cr, have shown an increased activation energy of sintering when more Cr is added.[123] Cooper *et al.*[123] varied the Cr content in the binder from 0.1-5 wt.% and heated specimens to 1500 °C in an induction furnace, which caused liquid-phase sintering to occur. Another study with pure W and a NiCr binder performed by Srikanth and Upadhyaya[124], showed that additional Cr content also reduced the densification during liquid-phase sintering at 1500 °C, due to reduced liquid-phase formation and grain boundary penetration. In this study, the WCr alloys remained more porous, up to 10% porosity, in the HP consolidations compared to WMo alloys, which had less than 1% porosity. Previous studies on the W-Cr-Ni system have reported that an intermediate precipitate can occur, specifically σ-phase, which further hinders densification by altering interface energies and/or interfering with interfacial dissolution/reprecipitation.[125, 126, 127] Evidence of an intermetallic phase forming between particles with high Cr and Fe composition is seen in WCr alloy specimens consolidated above 1100 °C; further discussion on this subject is in Section 4.5.2.

4.4 Vickers Microhardness

Vickers microhardness as function of dwell temperatures are shown in Figure 17. For WMo alloys with 1 min dwells, Vickers microhardness was the highest at 1050 °C then decreased at an 1100 °C consolidation temperature due to grain growth. WCr alloys increased in hardness with increasing temperature for the HP specimens with the highest hardness of 1520 HV for the W8Cr2 specimen consolidated at 1100 °C with a dwell time of 1 min. With the exception of W9Cr1 consolidated at the lowest temperature and shortest dwell time, all consolidated specimens had hardness values above the baseline materials, WHA 1450 and wrought W (Figure 17). The LP specimen series showed a decreasing trend in hardness with temperature above 1100 °C for W+ 1 and 20 min and W9Cr1 20 min. The highest hardness of the LP W9Cr1 specimens was at a 1200 °C consolidation temperature, after which, W9Cr1 decreased in hardness with increasing temperature. Increasing dwell time lowered the specimen hardness at and above 1100 °C in the W+ alloy due to an increase in grain size, Figure 17. In the W9Cr1 alloy, specimens consolidated at and above 1200 °C had higher hardness with the shorter dwell time. Excluding W9Cr1-1100C-1min-LP, all W9Cr1 specimens had higher hardnesses when compared to the W+ alloy with the same processing parameters.

In general, the remaining porosity and reduction in density of the specimens caused the lower hardnesses until negligible porosity was reached. At higher temperatures, the increased grain size reduced the hardness, which is an expected behavior (Figure 17). The addition of Cr to the W alloys reduced the hardness compared to the W+ alloy at lower temperatures because of the reduced densification that occurred during processing. Once the W9Cr1 alloy had reached near full densification at higher temperatures, the hardness was improved over the W+ alloy. With the addition of Cr to W, the increased hardness is attributed to the grain growth inhibition of Cr, which would lower the grain size in consolidated specimens.[128]

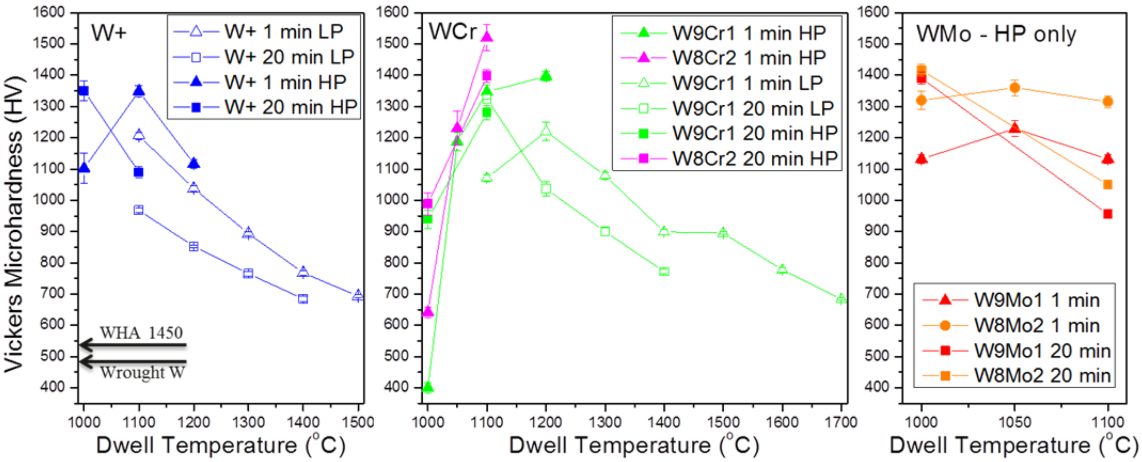

Figure 17 Measured Vickers microhardness vs. dwell temperature for W+, WCr, and WMo alloys. Baseline KEP materials, WHA1450 and Wrought W, are also shown for comparison.

The HP W9Cr1 alloy specimens increased in hardness as temperature and pressure increased (Figure 17). The highest hardness for W+ was at 1100 °C and the highest hardness for W9Cr1 was at 1200 °C for both applied pressures. The increased pressure during consolidation resulted in improved hardnesses for both W+ and W9Cr1. In both W+ and W9Cr1, the increased pressure resulted in improved hardness at both 1100 °C and 1200 °C. The improvements in hardness with increased pressure during consolidation are between 7-25 % (Figure 17). The highest hardnesses of HP W+, W9Cr1, W8Cr2, W9Mo1, and W8Mo2 with the consolidation temperature and dwell time are shown in Table 5.

Table 5 Highest hardnesses of HP W+, W9Cr1, W8Cr2, W9Mo1, and W8Mo2 alloys with consolidation temperature, dwell time and homologous temperature.

	W+	W9Cr1	W8Cr2	W9Mo1	W8Mo2
Highest Hardness (HV)	1350	1394	1520	1391	1397
Consolidation Temperature (°C)	1000	1200	1100	1000	1000
Dwell Time (min)	20	1	1	20	20
Porosity (%)	1.79	0.03	1.63	0.01	0.39

4.5 Consolidated Specimen Morphology

In what follows, SEM micrographs of consolidated W+, W9Cr1, W8Cr2, W9Mo1, and W8Mo2 specimens will be presented. Specimen micrographs of each alloy are presented in groups with varying dwell temperature and dwell time. To facilitate comparison, each micrograph is at the same magnification. Black regions of the micrographs are pores, dark gray regions are intermetallic phases, and the lighter gray regions are the bulk specimen. Consolidated specimens may also be referred to by the alloy, temperature, dwell time, and pressure in the form of alloy-temperature-dwell time-pressure (e.g., W9Cr1-1200C-20min-LP).

4.5.1 W+ Alloy Morphology

SEM micrographs of HP W+ specimens consolidated at 1000 °C and 1100 °C for 1 and 20 min are shown in Figure 18. W+-1000C-1min-HP (Figure 18a) shows the most porosity, seen as black regions. Increasing temperature and dwell time reduced the pore size and porosity in W+. Negligible porosity is seen in specimens prepared at 1100 °C, Figure 18b and Figure 18d, at both short and long dwell times. The W+-1100C-20min-HP specimen (Figure 18d) shows some intermetallic phase separation out of the bulk, seen as dark gray regions. The increase in intermetallic phase fraction found in W+ consolidated at 1100 °C for 20 min is due to the additional dwell time, which allowed more separation towards equilibrium composition to occur. Specimens are polycrystalline with grain sizes not visible at this scale. The increased atomic migration at 1100 °C resulted in increased separation towards the equilibrium phases, a W solid solution and the μ-phase, shown in Figure 19. The STEM-EDS results (Table 6), with corresponding image (Figure 19a), show the two phases that are consistent with the equilibrium phases of the binary W-Fe system (Figure 10). STEM-EDS mapping of the same region shows Fe separation, with W spread throughout the region (Figure 19b-c).

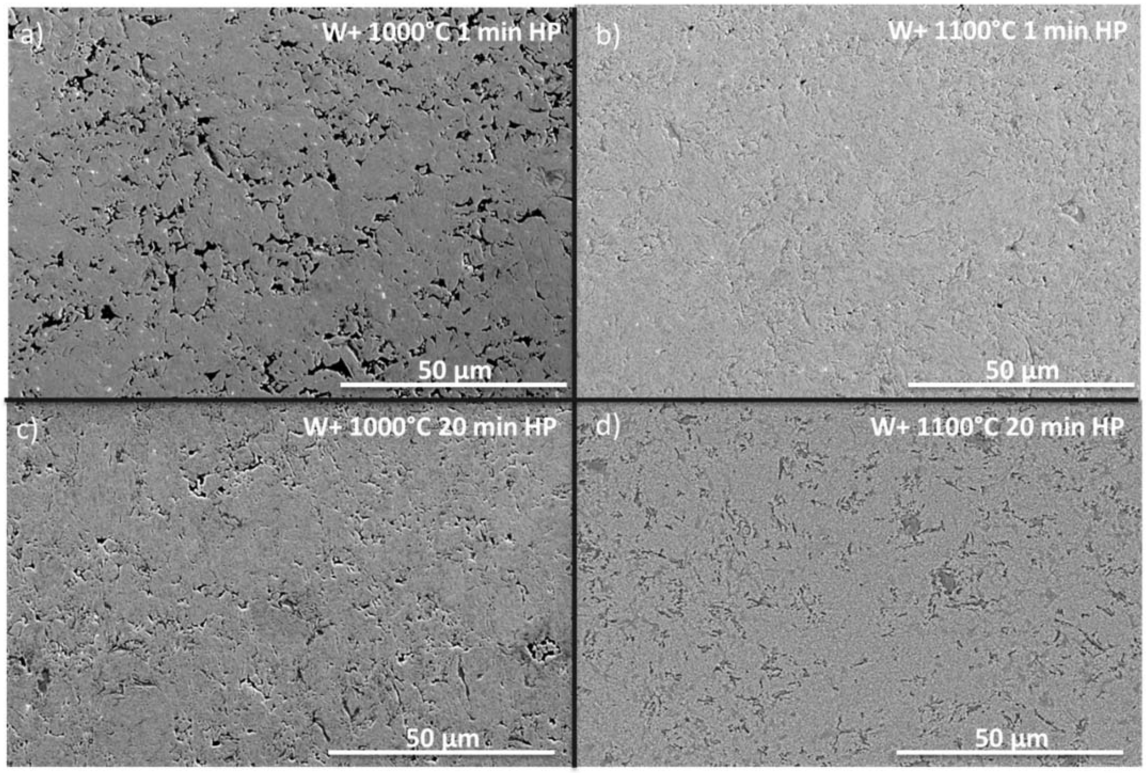

Figure 18 W+ alloy consolidated in HP die set. a) W+ 1000 °C 1min HP, b) W+ 1100 °C 1 min HP, c) W+ 1000 °C 20 min HP and d) W+ 1100 °C 20 min HP. Black regions are pores and dark gray regions are intermetallic phases.

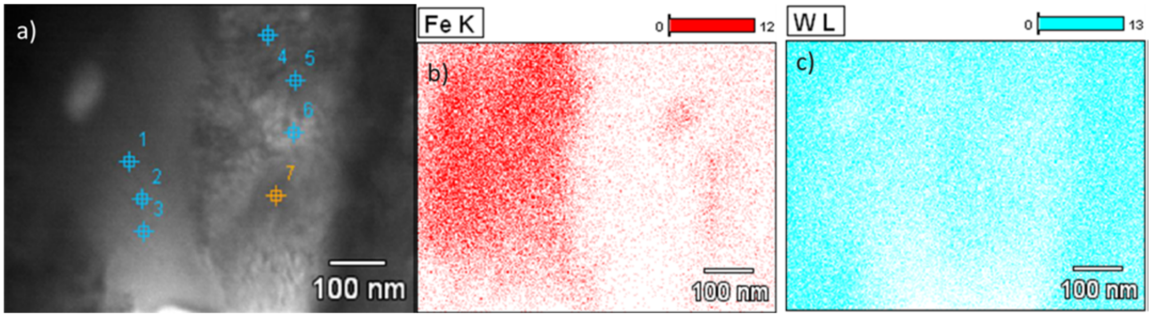

Figure 19 STEM of W+ consolidated at 1100 °C for 1 min (a), corresponding to the EDS data points in Table 6. STEM-EDS mapping of the region shows Fe separation, Fe-K (b) and W-L (c).

Table 6 EDS results in at.% for W+-1100C-1min-HP, corresponding with Figure 19a.

Data Point	Fe (at.%)	EE (at.%)	W (at.%)	EE (at.%)
1	55.85	+/- 0.93	44.15	+/- 0.82
2	54.06	+/- 1.26	45.94	+/- 1.14
3	41.56	+/- 1.81	58.44	+/- 1.75
4	2.86	+/- 0.51	97.14	+/- 1.38
5	35.17	+/- 1.16	64.83	+/- 1.20
6	4.18	+/- 0.65	95.82	+/- 1.66
7	2.78	+/- 0.72	97.22	+/- 2.01

SEM micrographs of LP W+ specimens consolidated at 1100 °C, 1200 °C, 1300 °C, 1400 °C and 1500 °C for 1 min dwell time are shown in Figure 20. Porosity can be seen in W+-1100C-1min-LP (Figure 20a). At 1300 °C and 1400 °C (Figure 20c and Figure 20d), there is significant intermetallic phase separation with negligible porosity. At 1500 °C (Figure 20e), some porosity is returning and less intermetallic phase is present as compared to lower temperatures. A detailed discussion on the intermetallic phase separation is in Section 4.8. The additional time needed to reach higher temperatures caused an increase in the intermetallic phase separation towards equilibrium compositions. The intermetallic phase initially forms along particle boundaries and begins to coalesce at triple junctions by 1300 °C in the W+ specimens. The lack of intermetallic phase seen in W+ consolidated at 1500 °C for 1 min is discussed in Section 4.5.2, as this character is also seen in WCr alloys.

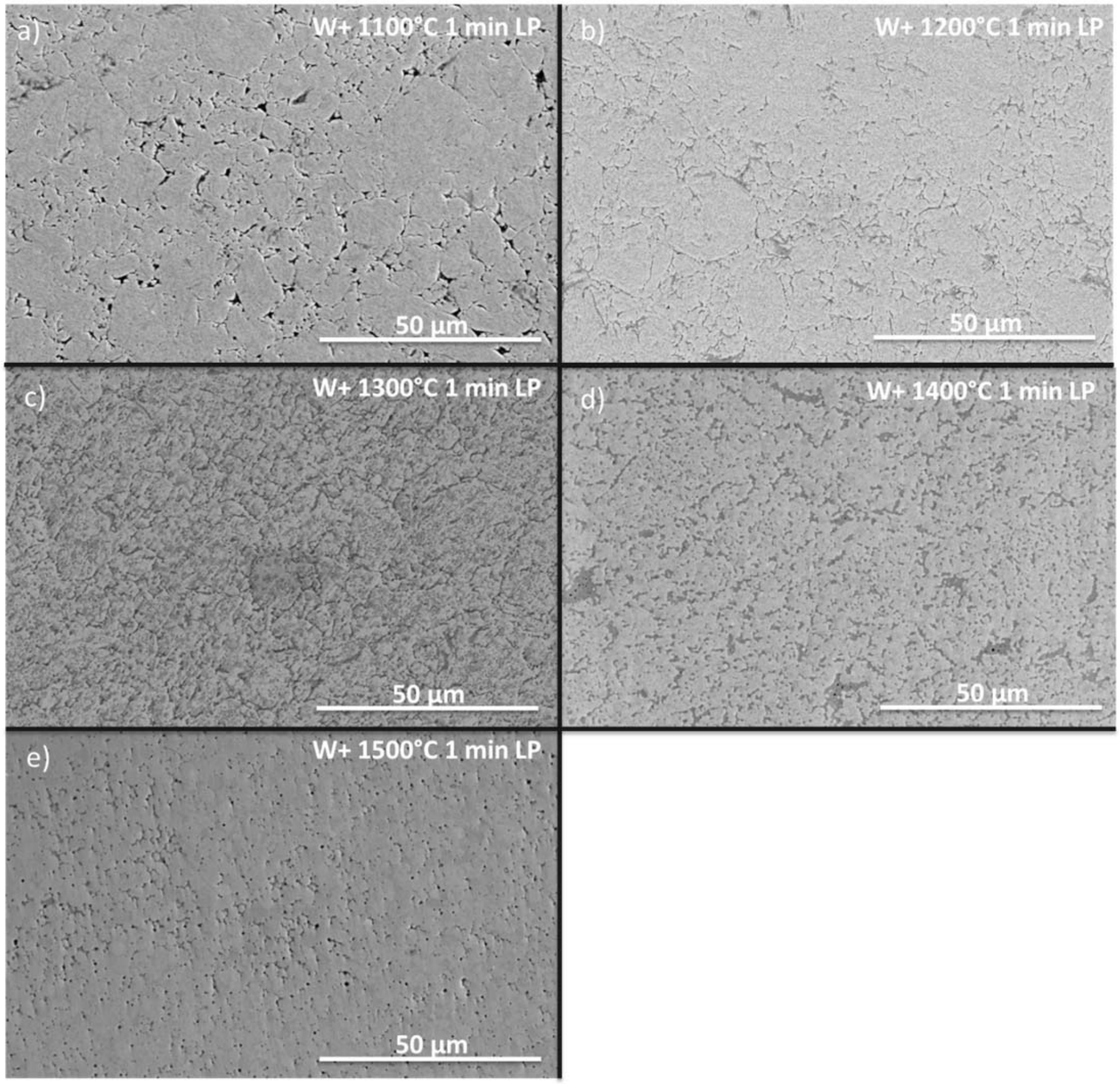

Figure 20 W+ alloy consolidated in LP die set. a) W+ 1100 °C 1 min LP, b) W+ 1200 °C 1 min LP, c) W+ 1300 °C 1 min LP, d) W+ 1400 °C 1 min LP and e) W+ 1500 °C 1 min LP.

SEM micrographs of LP W+ specimens consolidated at 1100 °C, 1200 °C, 1300 °C, and 1400 °C for 20 min dwell time are shown in Figure 21a-d. W+-1200C-20min-LP shows negligible porosity (Figure 21b). Significant intermetallic phase separation out of the bulk occurred in W+ consolidated at 1300 °C and 1400 °C (Figure 21c and Figure 21d). Intermetallic phase regions grew and began to coalesce as the temperature increased from 1300 °C to 1400 °C (Figure 21c-d). Increased dwell time allowed for more intermetallic phase separation and grain growth to occur. The W+ consolidated for 20 min at 1200 °C shows a more homogenous microstructure than compared to the W+ 1 min specimen, which has the intermetallic phase remaining at particle boundaries (Figure 20b and Figure 21b). Increasing the pressure of consolidation from 100 MPa to 210 MPa in W+ reduced the porosity at 1100 °C (Figure 20a and Figure 18b). W+ consolidated at 1200 °C for 1 min for both 100 MPa and 210 MPa had similar porosities, 0.0527 and 0.0648, respectively, revealing that the increased pressure did not have an effect on porosity when specimens were consolidated at 1200 °C (Figure 20b and Figure 21b).

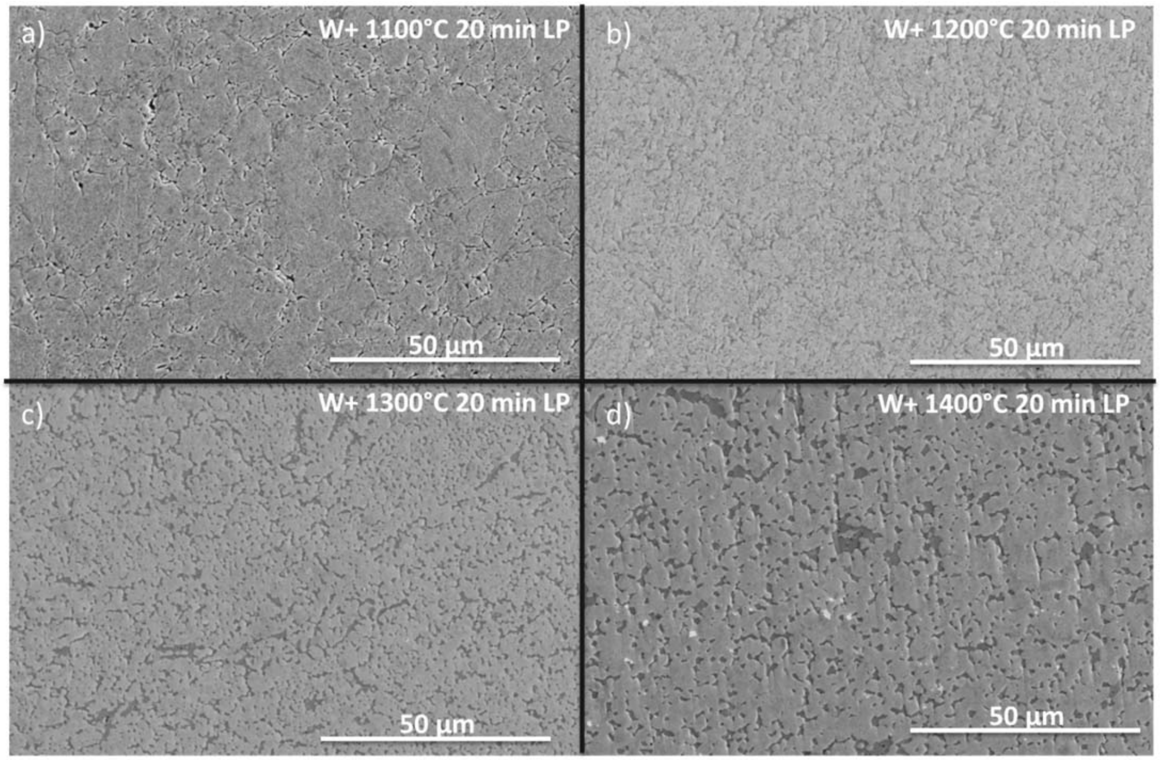

Figure 21 W+ alloy consolidated in LP die set. a) W+ 1100 °C 20 min, b) W+ 1200 °C 20 min, c) W+ 1300 °C 20 min and d) W+ 1400 °C 20 min.

4.5.2 WCr Alloy Morphology

SEM micrographs of HP W9Cr1 specimens consolidated at 1000 °C and 1100 °C for 1 and 20 min dwell times are shown in Figure 22. W9Cr1-1100C-20min-HP (Figure 22d) was the only W9Cr1 specimen that reached negligible porosity. W9Cr1 specimens with lower temperature and shorter dwell times had significant porosity (Figure 22a-c). Remaining porosity (black) and some intermetallic phase separation (dark gray) were seen in the specimen consolidated at 1100 °C for 1 min (Figure 22b). The STEM-EDS results for W9Cr1 (Table 7), with corresponding image (Figure 23), show that multiple phases are present in the specimen and are not consistent with the equilibrium phase assemblage of the ternary W-Cr-Fe system (Figure 10). The W solid solution, data points 3 and 7, in this specimen has a composition of W-14Cr-4Fe, which is above the equilibrium concentrations for Cr and Fe, ~12 at.% and ~3 at.%, respectively (Figure 11). The EDS data also show that the intermetallic phase seen in this specimen are not at compositions predicted by the equilibrium phase diagram, data points 1, 2, 4, 5, 6, and 8. The short dwell time limited the separation from the starting composition into the equilibrium phases. STEM-EDS mapping of the regions shows Fe-rich and Cr-rich regions, with W present throughout (Figure 23c-d).

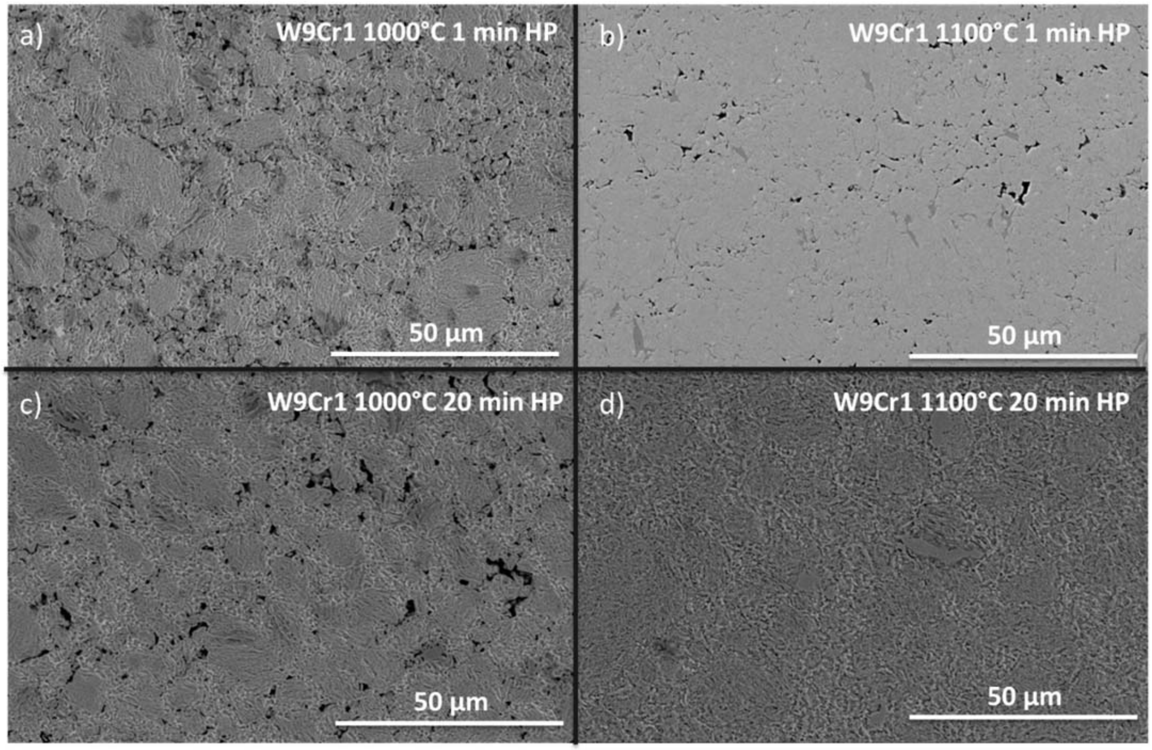

Figure 22 W9Cr1 alloy consolidated in HP die set. a) W9Cr1 1000 °C 1 min HP, b) W9Cr1 1100 °C 1 min HP, c) W9Cr1 1000 °C 20 min HP and d) W9Cr1 1100 °C 20 min HP.

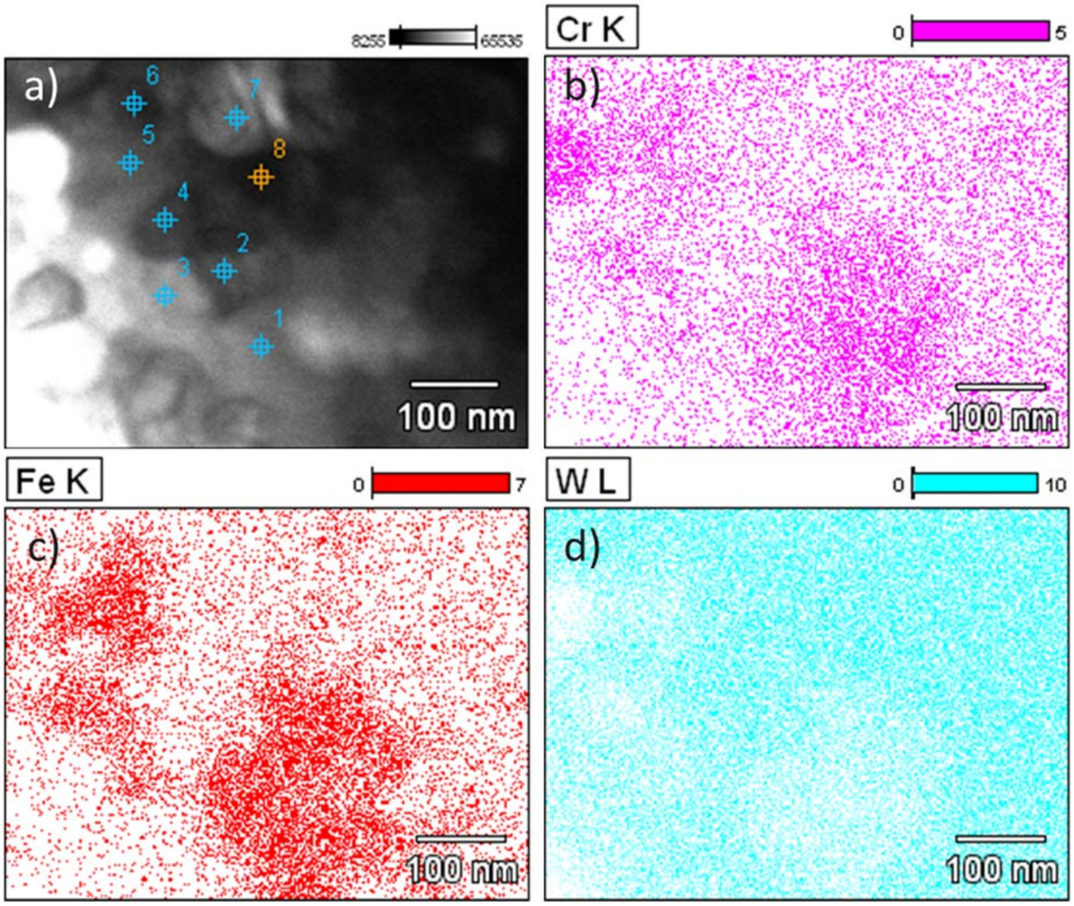

Figure 23 STEM of W9Cr1 consolidated at 1100 °C for 1 min (a), corresponding to the EDS data points in Table 7. STEM-EDS mapping of the region shows Cr-rich (b) and Fe-rich (c) areas, and the W is present throughout the region (d).

Table 7 EDS results in at.% for W9Cr1-1100C-1min-HP, corresponding to Figure 23.

Data Point	Cr (at.%)	EE (at.%)	Fe (at.%)	EE (at.%)	W (at.%)	EE (at.%)
1	17.76	+/- 1.23	18.90	+/- 1.09	63.34	+/- 1.22
2	22.56	+/- 0.92	44.34	+/- 1.06	33.10	+/- 0.87
3	12.71	+/- 1.71	3.08	+/- 0.64	84.21	+/- 1.70
4	14.11	+/- 1.43	12.07	+/- 1.16	73.82	+/- 1.44
5	23.40	+/- 0.86	41.17	+/- 0.95	35.43	+/- 0.82
6	21.82	+/- 0.84	36.58	+/- 0.88	41.60	+/- 0.81
7	14.33	+/- 1.26	4.87	+/- 0.87	80.81	+/- 1.25
8	24.86	+/- 1.27	7.27	+/- 0.86	67.87	+/- 1.11

SEM micrographs of HP W8Cr2 specimens consolidated at 1000 °C and 1100 °C for 1 and 20 min dwell times are shown in Figure 24a-d. Significant porosity remained in W8Cr2 specimens when consolidated at 1000 °C for both 1 and 20 min dwell times (Figure 24a and Figure 24c). Negligible porosity remained in the W8Cr2 specimen consolidated at 1100 °C for 20 min (Figure 24d). In specimens consolidated at 1100 °C (Figure 24b and Figure 24d), intermetallic phase regions can be seen as dark gray regions. Specimen porosity decreased with increasing dwell temperature and dwell time. Figure 24a shows initial particle bonding with a large amount of porosity remaining in the specimen consolidated at 1000 °C for 1 min dwell time. Increasing the dwell time to 20 min increased particle bonding at 1000 °C and resulted in increased intermetallic phase separation at 1100 °C. The additional Cr content in the WCr alloys reduced the overall densification compared to W+. The reduction in densification could be due to Cr inhibiting grain growth in W, as discussed in Section 4.3.

The STEM-EDS results (Table 8) for W8Cr2-1100C-20min-HP, with corresponding image (Figure 25), show that multiple compositions are present in the specimen and are not completely consistent with the equilibrium compositions of the ternary W-Cr-Fe system (Figure 10). The presence of a W solid solution beginning to form is shown in data points 2-6 and 10-13 with a mean composition of W-21Cr-6Fe. Data points 14-16 suggest another composition that has not reached an equilibrium phase, of approximately W-40Cr-30Fe. Data points 1 and 7-9 could be on grain boundaries or areas in transition between the intermetallic phase and the W solid solution. The presence of non-equilibrium phases can be expected when consolidating highly deformed non-equilibrium powders. The additional dwell time in the W8Cr2 specimen consolidated at 1100 °C resulted in near-equilibrium concentrations of the W solid solution (Table 8) compared to the W9Cr1 specimen consolidated at 1100 °C (Table 7). STEM-EDS mapping of the region shows Cr-rich and Fe-rich regions consistent with EDS spot analysis of the area (Figure 25b-d).

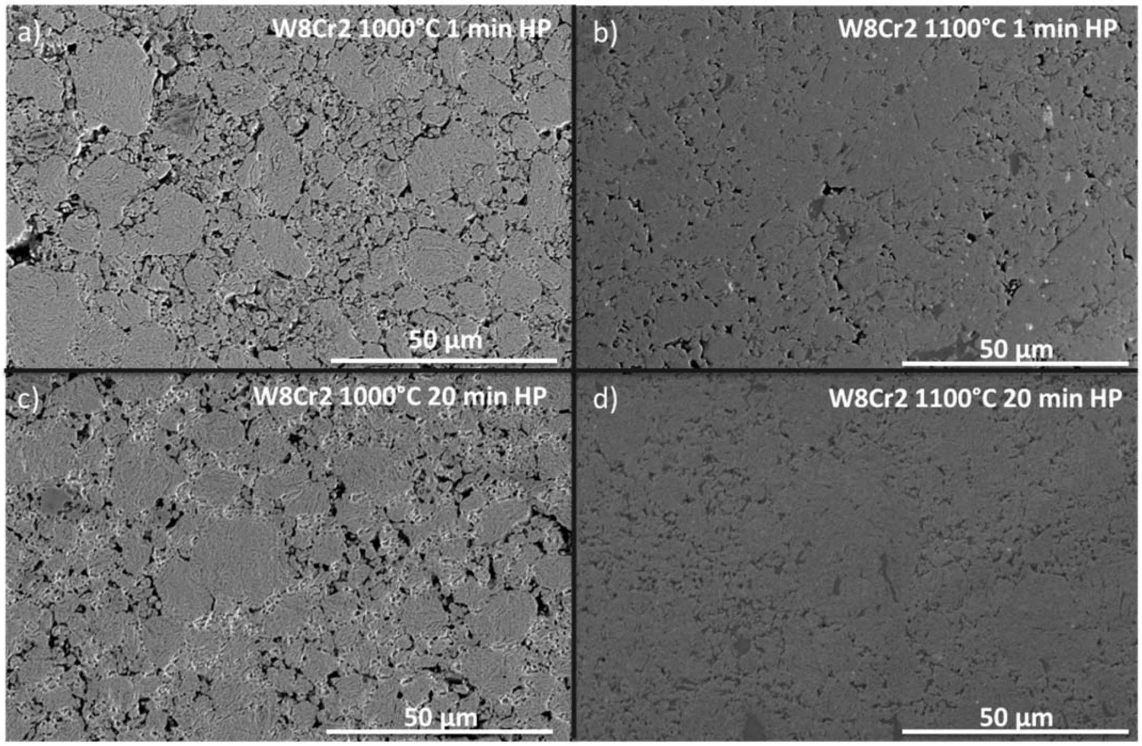

Figure 24 W8Cr2 alloy consolidated in HP die set. a) W8Cr2 1000 °C 1 min, b) W8Cr2 1100 °C 1 min, c) W8Cr2 1000 °C 20 min, and d) W8Cr2 1100 °C 20 min.

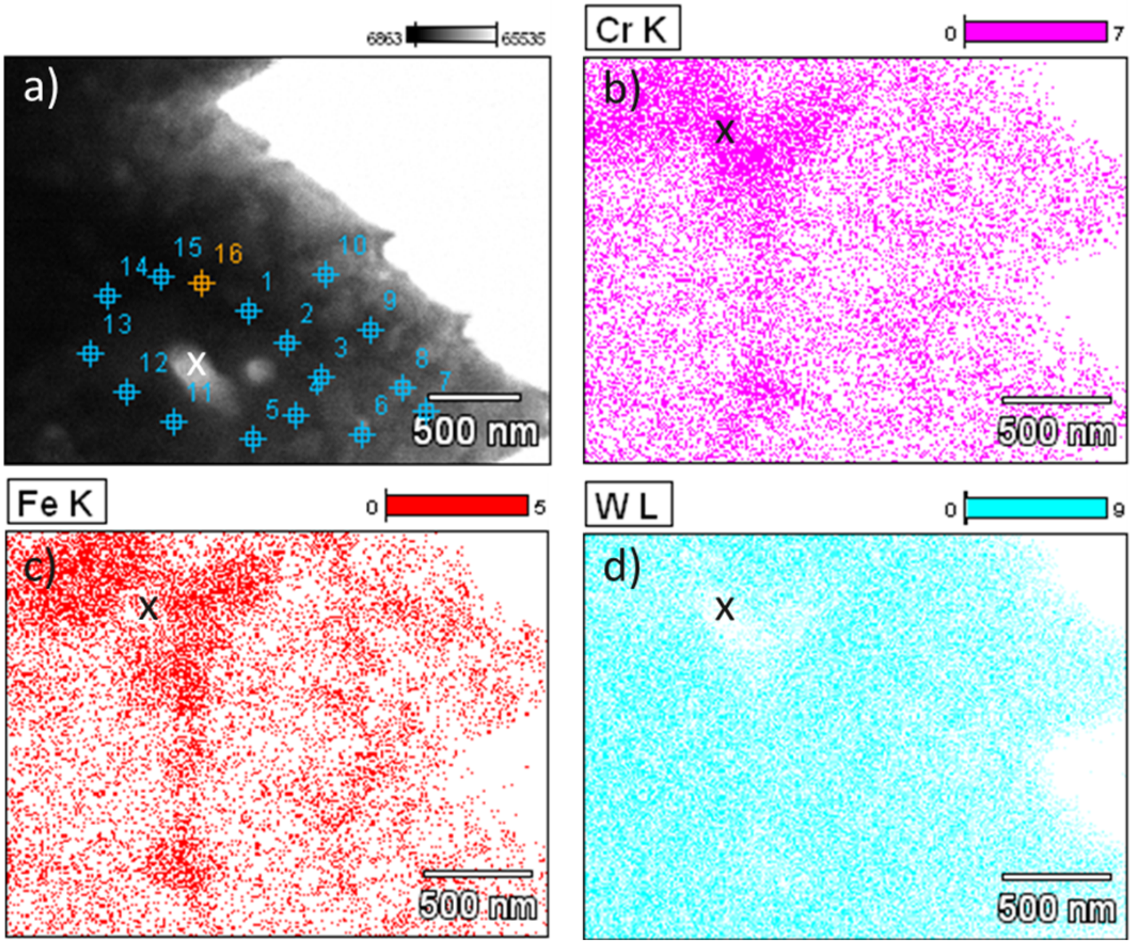

Figure 25 STEM of W8Cr2 consolidated at 1100 °C for 20 min, corresponding to the EDS data points in Table 8. STEM-EDS mapping of the region shows Cr-rich (b) and Fe-rich (c) regions, with W spread throughout (d). The white X in (a) corresponds to the black X in b-d.

Table 8 EDS results in at.% for W8Cr2-1100C-20min-HP, corresponding to Figure 25.

Data Point	Cr (at.%)	EE (at.%)	Fe (at.%)	EE (at.%)	W (at.%)	EE (at.%)
1	28.93	+/- 0.95	22.86	+/- 0.86	48.21	+/ -0.82
2	19.05	+/- 1.38	2.84	+/- 0.51	78.10	+/- 1.24
3	20.78	+/- 1.46	5.63	+/- 1.02	73.59	+/- 1.35
4	20.86	+/- 1.35	6.94	+/- 0.96	72.20	+/- 1.21
5	20.88	+/- 1.24	5.50	+/- 0.88	73.62	+/- 1.13
6	22.11	+/- 1.44	5.93	+/- 1.01	71.96	+/- 1.28
7	27.01	+/- 1.51	19.73	+/- 1.31	53.26	+/- 1.37
8	22.64	+/- 1.66	9.33	+/- 1.22	68.03	+/- 1.47
9	28.34	+/- 1.22	18.50	+/- 1.07	53.16	+/- 1.10
10	21.70	+/- 1.19	3.19	+/- 0.46	75.11	+/- 1.10
11	20.68	+/- 1.13	4.48	+/- 0.79	74.85	+/- 1.04
12	19.74	+/- 1.08	5.39	+/- 0.75	74.88	+/- 1.00
13	22.08	+/- 0.96	10.61	+/- 0.74	67.31	+/- 0.88
14	34.20	+/- 0.65	32.99	+/- 0.65	32.81	+/- 0.53
15	35.68	+/- 0.63	36.35	+/- 0.66	27.97	+/- 0.52
16	47.21	+/- 0.88	18.98	+/- 0.74	22.20	+/- 0.56

SEM micrographs of LP W9Cr1 specimens consolidated between 1100 °C and 1700 °C for 1 min dwell time are shown in Figure 26. The W9Cr1 specimens consolidated at 1200 °C and 1300 °C showed negligible porosity (Figure 26b and Figure 26c). At 1400 °C, a homogenous microstructure is seen with grain sizes between 1-2 μm and minimal intermetallic phase remaining (Figure 26d). No intermetallic phase remained in the W9Cr1 specimen consolidated at 1700 °C for 1 min, which showed grain sizes between 6-10 μm (Figure 26f). The W9Cr1 specimen consolidated at 1500 °C shows a spheroid grain microstructure associated with liquid-phase sintering (Figure 26e).[5] Higher temperatures caused the liquid phase to be pressed out of the specimen, evidence of which can be seen in the displacement data (Figure 27) and is discussed further in Section 4.5.5. Not all specimen displacement curves were recorded successfully due to software error, specifically W9Cr1 consolidated at 1500 °C and 1600 °C would have provided additional information. The displacement shows a steady increase until the dwell time is reached, then sharp increases in displacement are seen, which is due to the squeezing out of the liquid-phase, which can escape along the sides of the die wall (Figure 27). The presence of a liquid-phase is expected above 1500 °C, discussed further in Section 4.5.5; however, at 1400 °C, material was being pressed down the sides of the die.

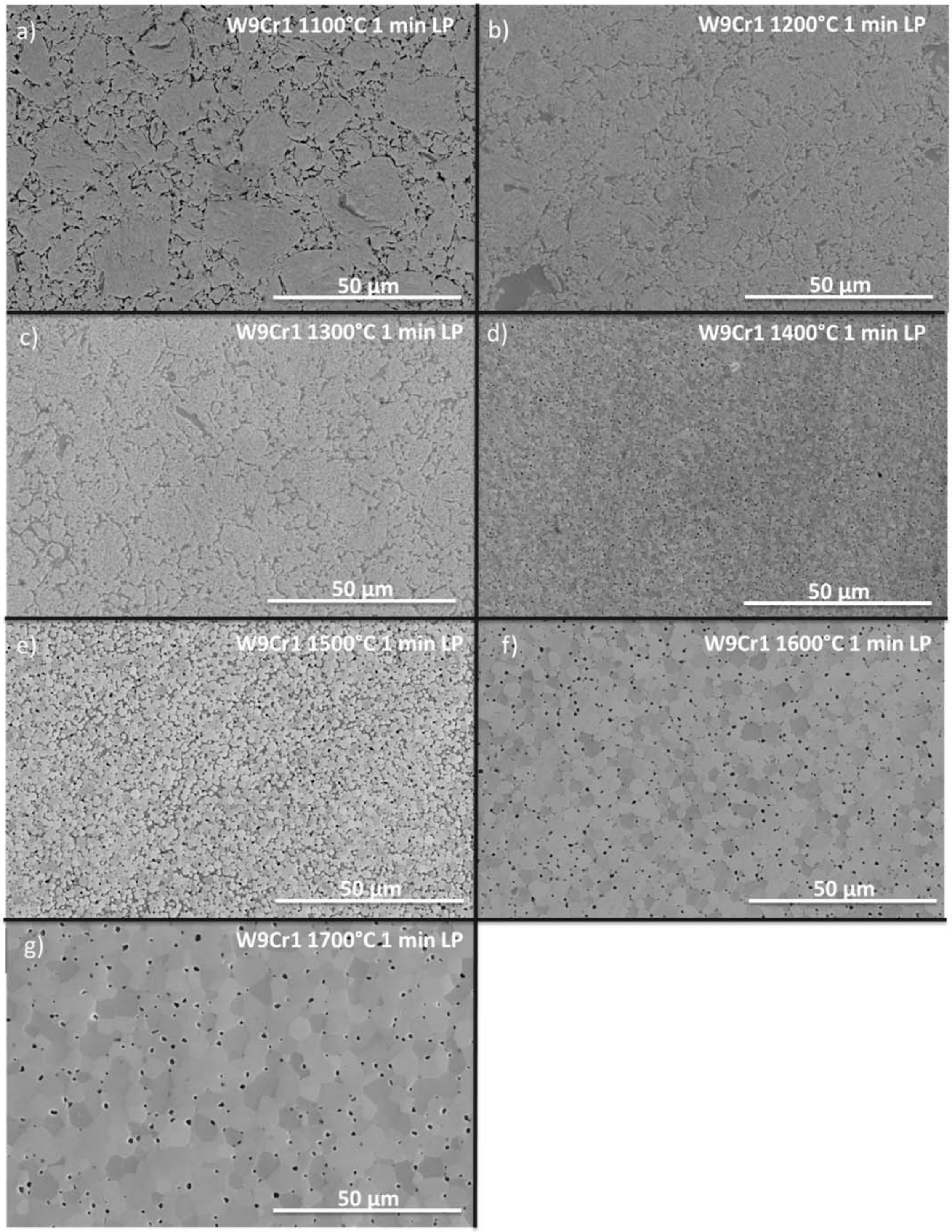

Figure 26 W9Cr1 alloy consolidated in LP die set. a) W9Cr1 1100 °C 1 min LP, b) W9Cr1 1200 °C 1 min LP, c) W9Cr1 1300 °C 1 min LP, d) W9Cr1 1400 °C 1 min LP, e) W9Cr1 1500 °C 1 min LP, f) W9Cr1 1600 °C 1 min LP, and g) W9Cr1 1700 °C 1 min LP.

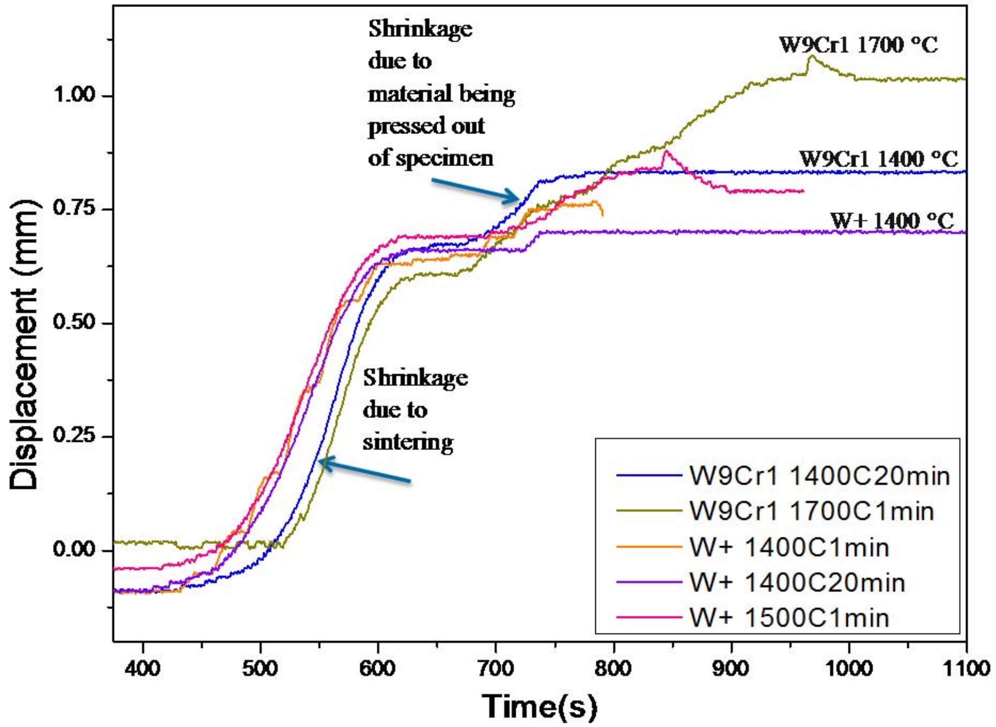

Figure 27 Displacement curves for specimens showing addition displacement occurred when material was pressed out of specimen and down sides of the die wall.

SEM micrographs of LP W9Cr1 specimens consolidated at 1100 °C, 1200 °C, 1300 °C, and 1400 °C for 20 min dwell time are shown in Figure 28. The W9Cr1 specimen consolidated at 1100 °C for 1 min (Figure 28a) shows remaining porosity and some intermetallic phase separation occurred. At 1300 °C, the intermetallic phase occurred at grain boundaries and triple junctions (Figure 28c), by 1400 °C large intermetallic phase regions had coalesced (Figure 28d). A large change in the intermetallic phase distribution can be seen between the specimens consolidated at 1300 °C and 1400 °C (Figure 28b and Figure 28d). An intermetallic phase composition has separated out of the bulk at 1200 °C (Figure 28b) and then begins to coalesce, leaving behind pores at grain boundaries by 1400 °C (Figure 28d).

Comparison between consolidation at 210 MPa and 100 MPa in W+ and W9Cr1 alloys with temperatures at 1100 °C and 1200 °C for 1 min dwell time was made to determine the effect of applied pressure during consolidation of these alloys. Higher porosity can be seen in W9Cr1 consolidated at 1100 °C and 100 MPa as compared to 210 MPa (Figure 26a and Figure 22b). Minimal difference is seen in SEM micrographs between specimens consolidated at 1200 °C for both 100 MPa and 210 MPa (Figure 26b and Figure 28b).

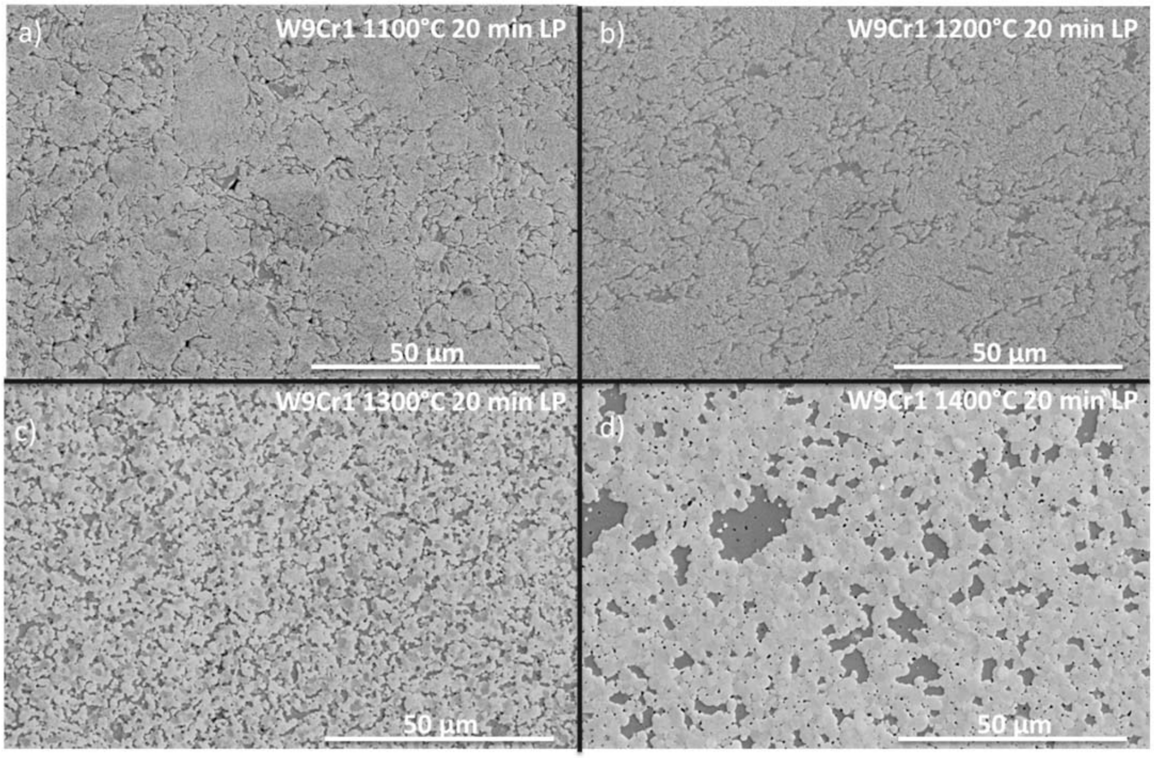

Figure 28 W9Cr1 alloy consolidated in LP die set. a) W9Cr1 1100 °C 20 min LP, b) W9Cr1 1200 °C 20 min LP, c) W9Cr1 1300 °C 20 min LP, and d) W9Cr1 1400 °C 20 min LP.

4.5.3 WMo Alloy Morphology

SEM micrographs of HP W9Mo1 specimens consolidated at 1000 °C and 1100 °C for 1 and 20 min dwell times are shown in Figure 29. W9Mo1-1000C-1min-HP and

W9Mo1-1000C-20min-HP (Figure 29a and Figure 29c) show some porosity. In W9Mo1-1100C-1min-HP and W9Mo1-1100C-20min-HP (Figure 29b and Figure 29d), negligible porosity remained in specimens prepared at 1100 °C. Increasing the temperature of consolidation and the dwell time reduced the porosity in W9Mo1. Contrast seen in W9Mo1-1100C-20min-HP (Figure 29d) is the start of grains becoming visible at this scale. Minimal intermetallic phase separation is seen in W9Mo1-1100C-20min-HP (Figure 29d), increasing the homogeneity of this specimen above WCr alloys and W8Mo2 specimens consolidated at 1100 °C for 20 min.

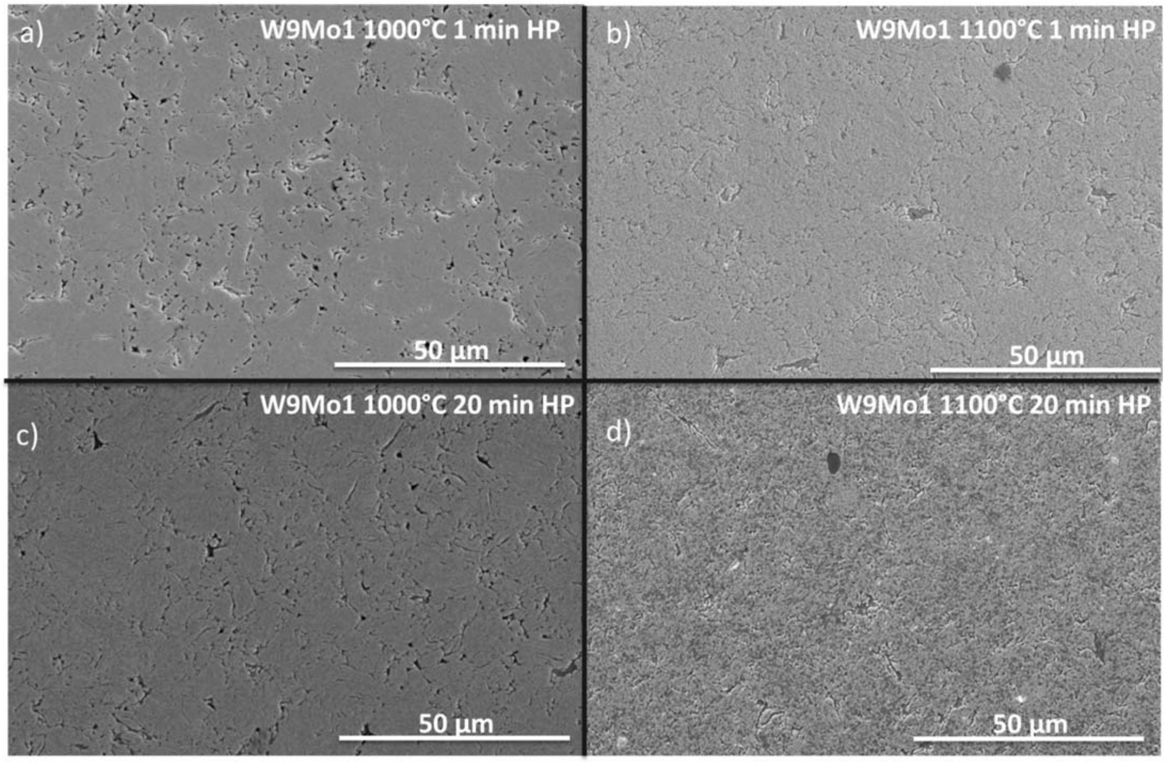

Figure 29 W9Mo1 alloy consolidated in HP die set. a) W9Mo1 1000 °C 1 min HP, b) W9Mo1 1100 °C 1 min HP, c) W9Mo1 1000 °C 20 min HP, and d) W9Mo1 1100 °C 20 min HP. Porosity can be seen in specimens consolidated at 1000 °C.

SEM micrographs of HP W8Mo2 specimens consolidated at 1000 °C and 1100 °C for 1 and 20 min dwell times are shown in Figure 30. W8Mo2-1000C-1min-HP

(Figure 30a) had more porosity than all of the specimens in this series. Consolidation at 1100 °C for 20 min resulted in nearly full densification (Figure 30c). Increasing the temperature and time reduced the porosity in the consolidated specimens of W8Mo2. The additional Mo content in W8Mo2, compared with W9Mo1, resulted in lower porosity in specimen consolidated at 1000 °C with a 1 min dwell time, 0.054% and 1.79%. Intermetallic phase separation out of the bulk can be seen (Figure 30c and Figure 30d) as dark gray regions and varied in composition due to the Fe pick up from high-energy ball milling. The larger regions of intermetallic phase seen in W8Mo2-1100C-20min-HP (Figure 30d) are attributed to Fe pick up in the powder as seen in Figure 9. SEM phase analysis (Figure 31) shows that the larger intermetallic phase regions have a composition consistent with the μ-phase, Fe-37Mo-5Mo (Table 9). Both W-Fe and Mo-Fe will form a μ-phase and have an extended homogeneity range, 39-44 at.% Mo and 40-43 at.% W [117, 129]; however, the smaller intermetallic phase regions seen in W8Mo2-1100C-20min-HP showed a higher concentration of W, approximately 50 at.% (Table 10).

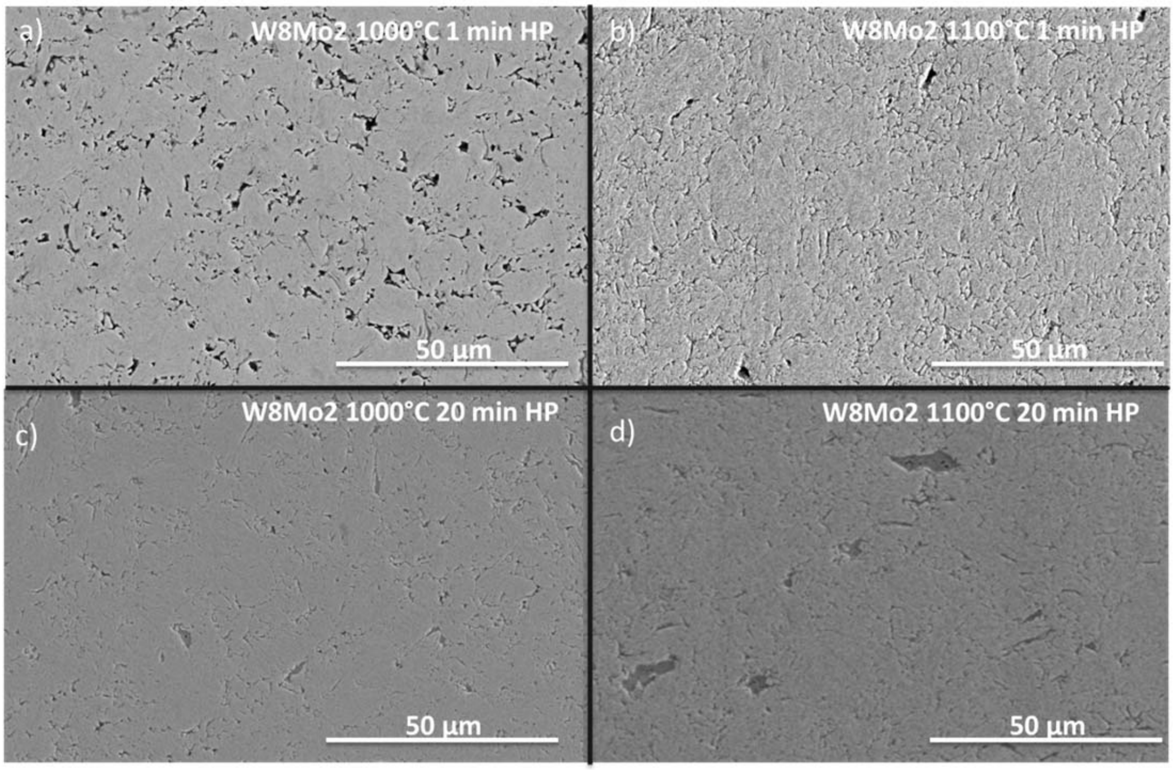

Figure 30 W8Mo2 alloy consolidated in HP die set. a) W8Mo2 1000 °C 1 min HP, b) W8Mo2 1100 °C 1 min HP, c) W8Mo2 1000 °C 20 min HP, and d) W8Mo2 1100 °C 20 min HP.

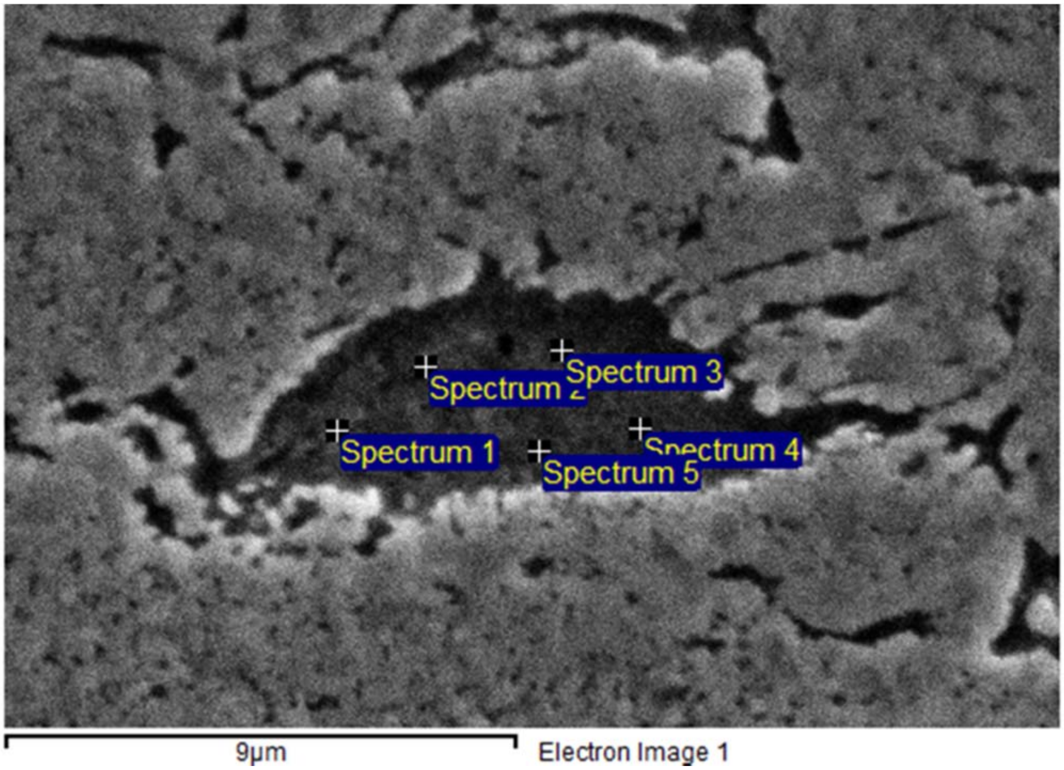

Figure 31 SEM micrograph of EDS spectrum points for W8Mo2-1100C-20min-HP, corresponding to Table 9.

Table 9 EDS results in at.% for the intermetallic phase seen in W8Mo2-1100C-20min-HP, corresponding to spectrum locations in Figure 31.

Spectrum	Fe	Mo	W
1	56.08	4.89	39.03
2	58.77	4.73	36.50
3	57.98	4.66	37.36
4	57.24	5.35	37.41
5	59.06	4.65	36.29
Mean	57.83	4.86	37.32
Std. Deviation	0.93	0.21	0.74

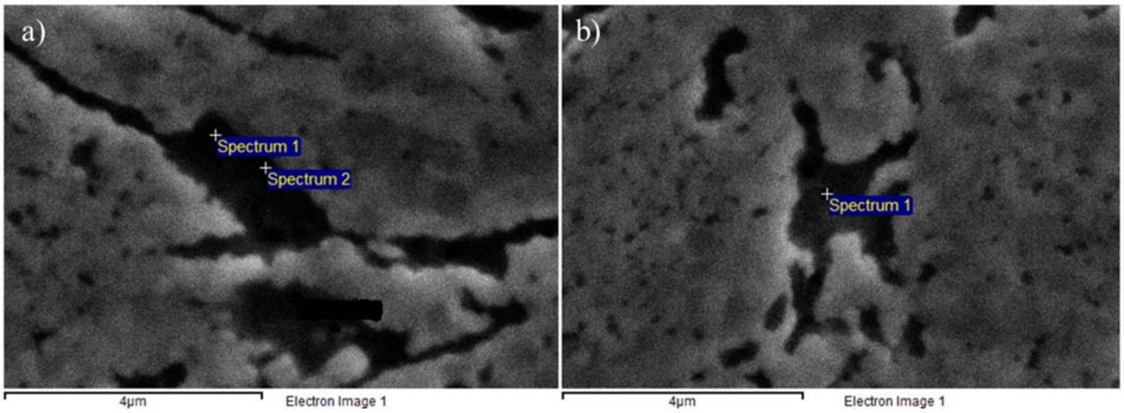

Figure 32 SEM micrograph of EDS spectrum points for W8Mo2-1100C-20min-HP, corresponding to Table 10.

Table 10 EDS results in at.% for the intermetallic phase seen in W8Mo2-1100C-20min-HP, corresponding to spectrum locations in Figure 32.

Spectrum	Fe (at.%)	Mo (at.%)	W (at.%)
1a	45.56	4.58	49.85
2a	45.87	4.87	49.26
1b	42.25	6.50	51.25
Mean	44.56	5.32	50.12
Std. Deviation	1.54	0.79	0.75

4.5.4 Intermetallic Phase Evolution

The compositions of the starting powders and the compacts studied were not in equilibrium as a consequence of the high-energy ball milling used to promote an amorphous microstructure. The non-equilibrium mixture also resulted in compositional evolution during sintering from the starting powder composition to many different compositions presented in previous sections. Phase separation from the initial composition was prevalent in specimens consolidated at 1100 °C with the presence of an intermetallic phase becoming more visible in SEM micrographs, and increased with higher temperatures of consolidation. A W solid solution and an intermetallic phase with varying composition developed out of the bulk powder composition based on EDS findings (Table 6, Table 7, Table, 8, Table 9, and Table 10). Most EDS data showed the intermetallic phase was inconsistent with the equilibrium phase compositions suggested by the phase diagrams, and as the consolidation temperature increased, higher Fe and Cr concentrations were found in the intermetallic phase, which caused it to become more saturated with Fe and Cr (Figure 33), although concentrations remained below those expected for the μ-phase. The EDS analysis of the intermetallic phase and the W solid solution seen in W9Cr1 consolidated at 1400 °C for 20 min is summarized in Table 11 and Table 12. Corresponding SEM micrographs are shown with data point location in Figure 33 and Figure 34.

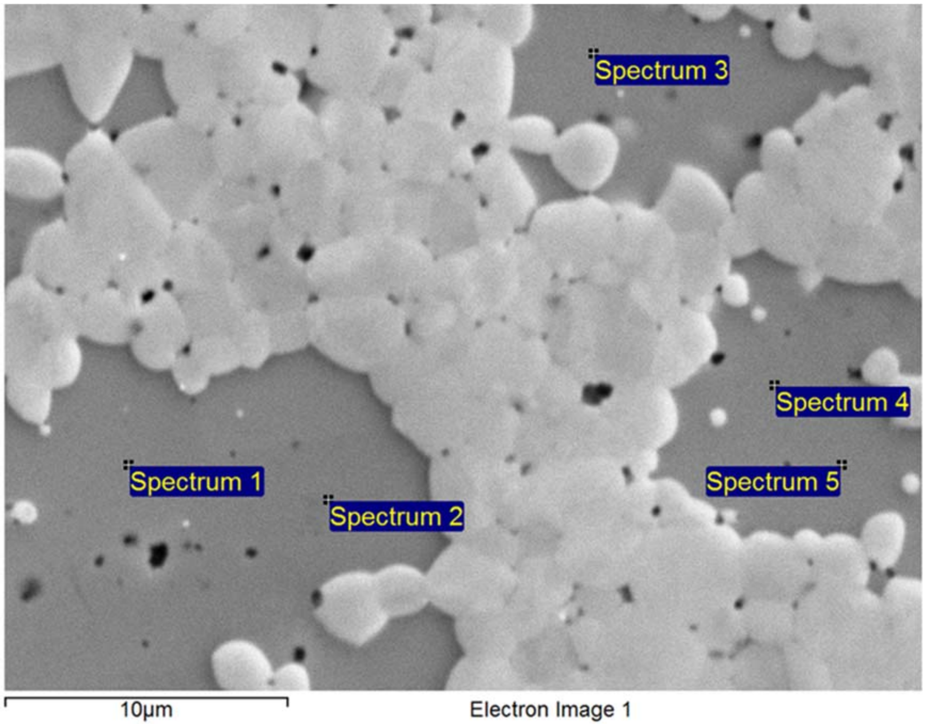

Figure 33 SEM micrograph of W9Cr1-1400C-20min-LP, corresponding to Table 11. The composition of the five spots was W-25Cr-25Fe in at.%, this composition is unexpected as it is not identified on phase diagrams.

Table 11 Selected point EDS analysis in at.% of the intermetallic phase in W9Cr1-1400C-20min-LP, corresponding to spectrum point in Figure 33.

Spectrum	Cr (at.%)	Fe (at.%)	W (at.%)
1	24.70	25.74	49.57
2	25.12	25.42	49.46
3	23.91	24.70	51.39
4	24.77	25.17	50.05
5	24.90	25.44	49.67
Mean	24.68	25.29	50.03
Std. Deviation	0.46	0.39	0.79

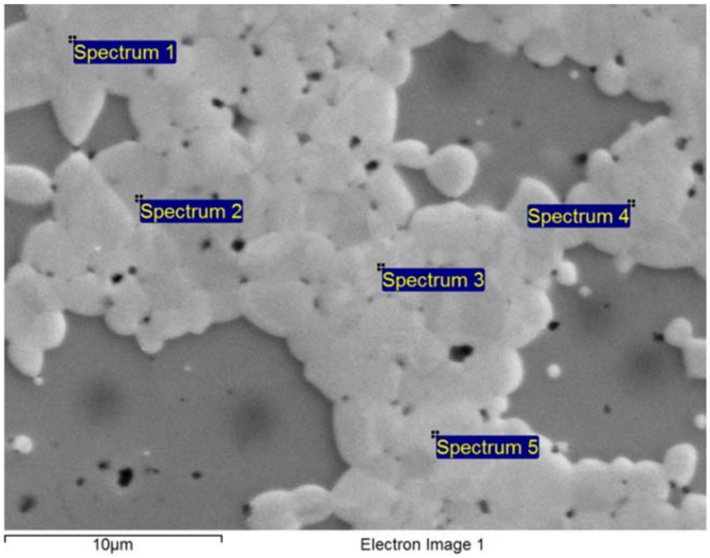

Figure 34 SEM micrograph of W9Cr1-1400C-20min-LP dwell time corresponding to Table 12. The composition of the five spots was W-6Cr-2Fe in at.%, this composition is expected and corresponds to the W solid solution.

Table 12 Selected point EDS analysis in at.% of the W solid solution in W9Cr1-1400C-20min-LP, corresponding to spectrum point in Figure 34.

Spectrum	Cr (at.%)	Fe (at.%)	W (at.%)
1	5.81	1.42	92.77
2	5.97	1.22	92.82
3	5.66	1.22	93.12
4	5.86	1.39	92.76
5	7.60	3.10	89.30
Mean	6.18	1.67	92.15
Std. Deviation	0.80	0.81	1.60

In Figure 35, a plot of the intermetallic phase percentage vs. dwell temperature is presented for W+ and W9Cr1, although the composition of the intermetallic phase varied with dwell temperature. The expected phase fractions for the intermetallic phase in equilibrium are ~14% for W+ and ~40% for W9Cr1, based off of tie line measurements from the initial powder compositions to the W solid solution and intermetallic phase. The μ-phase seen in W+ was more consistent with the equilibrium phase composition and phase fraction than was W9Cr1 at 1300 °C. As the intermetallic phase began to leave the specimen, discussed in Section 4.5.2 and 4.5.5, the density increased and at 1700 °C nearly all the intermetallic phase had been pressed out (Figure 26g and Figure 35). The W solid solution had only a few atomic percent of Fe and Cr, 2.5 at.% Fe and 4 at.% Cr, in W9Cr1-1700C-1min-LP (Figure 36). Additionally, porosity returned as the intermetallic phase was pressed out of the specimen and down the sides of the die wall, as suggested by the sintering displacement curves (Figure 27), but did not reduce the density due to the lower intermetallic phase fraction. The W9Cr1 bulk composition varied in the specimen consolidated at 1400 °C, and W9Cr1 specimens consolidated above 1500 °C continued to show loss of the intermetallic phase constituents as temperature was raised (Figure 36). Variation in W9Cr1-1400C-1min-LP could be due to reduced tolerances of Grafoil® cut by operator.

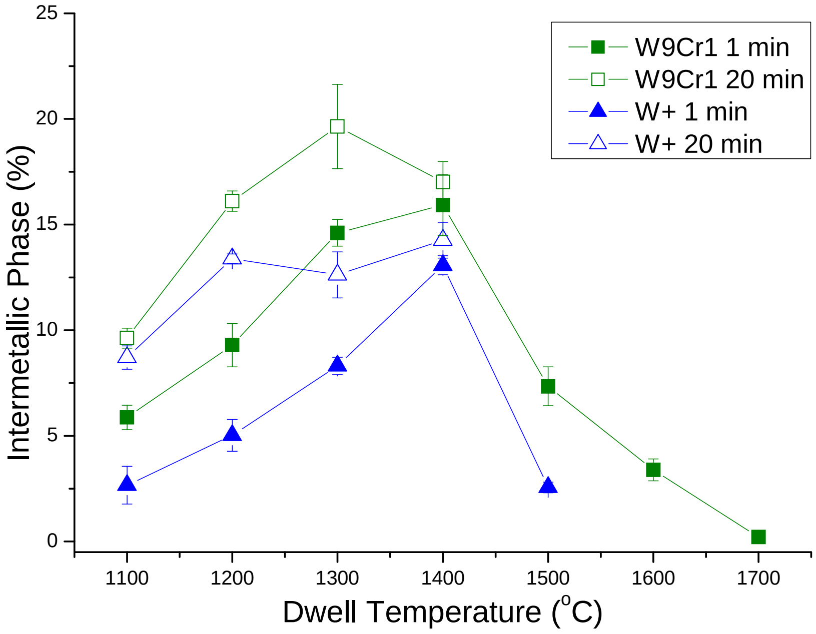

Figure 35 Intermetallic phase fractions in W+ and W9Cr1 alloys in the LP series.

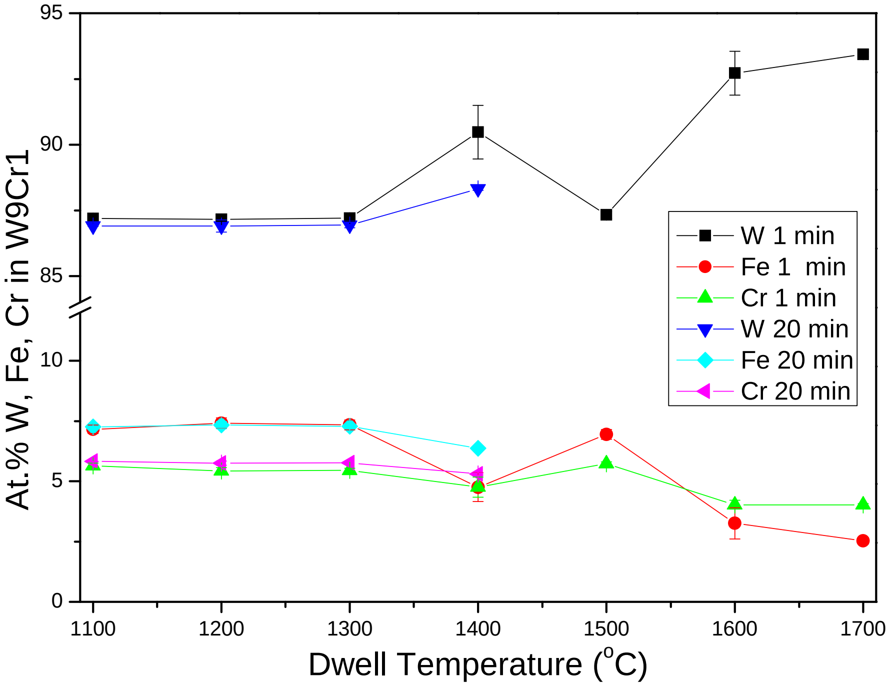

Figure 36 Atomic concentrations of W, Fe and Cr in W9Cr1 consolidated between 1100 °C and 1700 °C for 1 and 20 min. Variation of specimen at 1400 °C could be due to improper Grafoil® measurements. EDS data collected from two bulk area scans.

Porosity began to appear at grain boundaries as the intermetallic phase began to be pressed out of the compact during liquid-phase sintering. W9Cr1-1400C-1min-LP showed the movement of the intermetallic phase out of the bulk specimen, seen in Figure 37. The intermetallic phase has migrated out of the center of the specimen leaving behind some residual porosity. While the presence of a liquid-phase is not expected at this temperature, the intermetallic phase was pressed out of the bulk due to the applied pressure used during PECS and down the sides of the dies, which may have reduced tolerances due to thermal expansion. Residual porosity occurring at temperatures higher than 1300 °C is believed to be due to the separation of this phase. The separation does increase the density of the specimens as the intermetallic phase percentage is reduced; however, the high temperature increased the grain size and reduced the mechanical properties so these higher temperatures should be avoided when high hardness and small grain size are priorities.

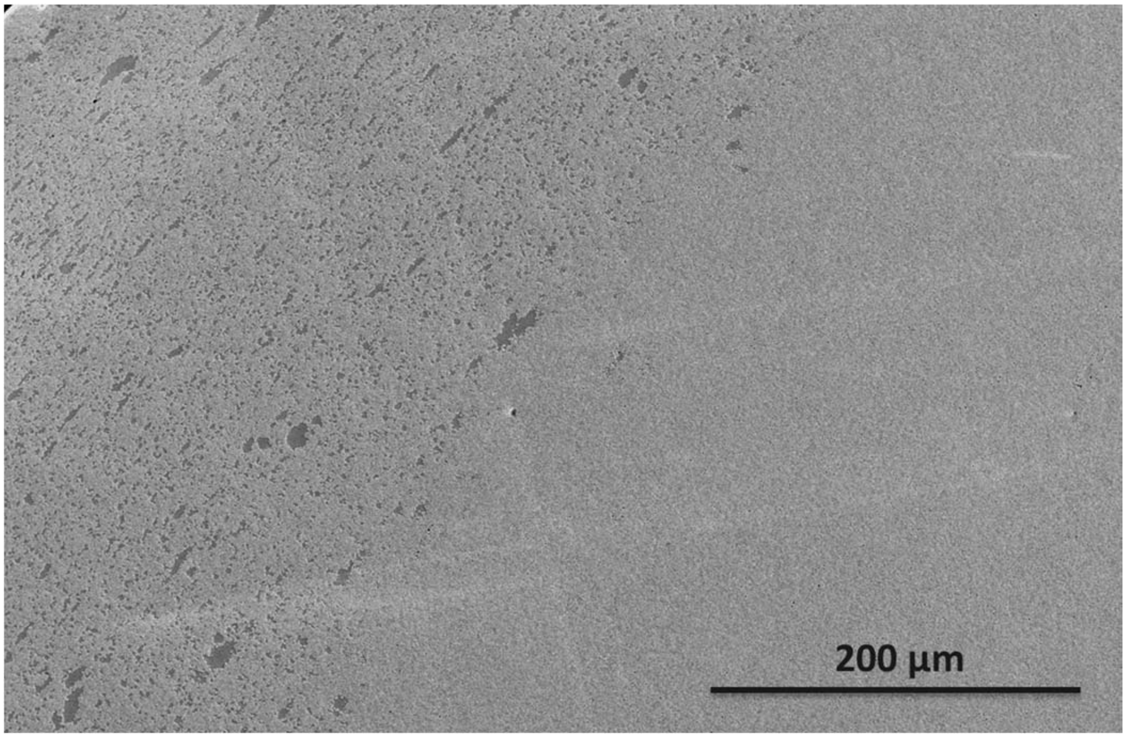

Figure 37 Intermetallic phase migration out of the bulk is seen in W9Cr1-1400C-1min-LP. The edge of specimen can be seen in upper left hand corner, and the center of the specimen has a minimal amount of intermetallic phase remaining.

4.5.5 Liquid-Phase Sintering

Liquid-phase sintering occurred in specimens consolidated at and above 1500 °C due to low melting points of several compositions being approached. Specimens above 1500 °C showed liquid-phase sintering characteristics such as spheroids and two-phase microstructure with a second phase filling the space in between particles, as seen in Figure 39. Fe has a melting temperature of 1538 °C and is seen in high concentration when not fully mixed into the bulk (Figure 9). Figure 38 shows the partial W-Cr-Fe ternary liquidus projection including additional compositions, µ-phase (labeled $W_{5.1}Fe_{7.9}$) and $Cr_{0.48}Fe_{0.52}$. Evidence of liquid-phase sintering is clearly visible at 1500 °C with the presence of spheroids in the microstructure (Figure 39a), though the congruent melting point of any composition has still not been reached.

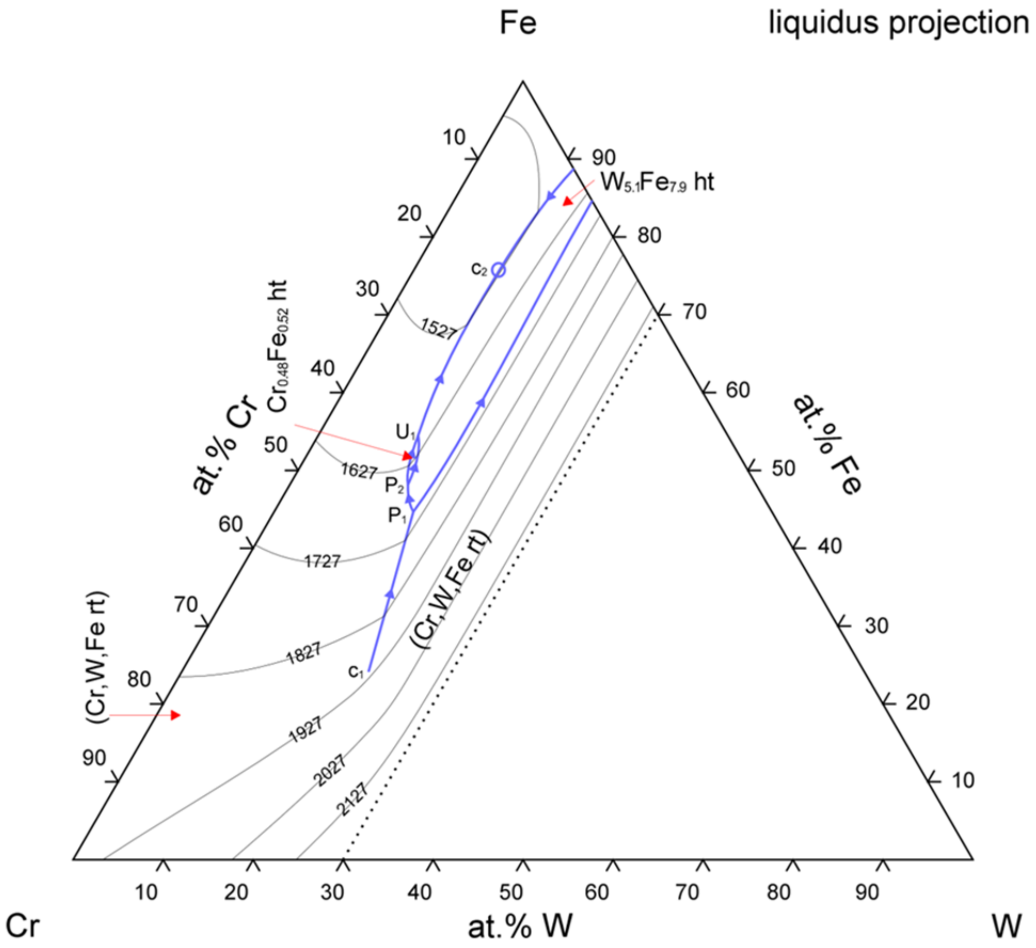

Figure 38 The partial W-Cr-Fe ternary liquidus projection.[130] Reprinted with permission of ASM International. All rights reserved. (#1200764)

Temperature distributions in the specimen and the die can vary depending on their distance from the die surface, which can cause temperatures in the specimen above that measured.[81, 131] Temperatures were measured in this study as close to the dies' inner diameter as possible, with either a thermocouple or optical pyrometer. Wang *et al*.[131] reported that temperatures inside the specimen were higher than the inner diameter of the die, and at the center of the specimen could be as much as 25-72 °C higher in computational studies with specimen sizes between 12-50 mm.

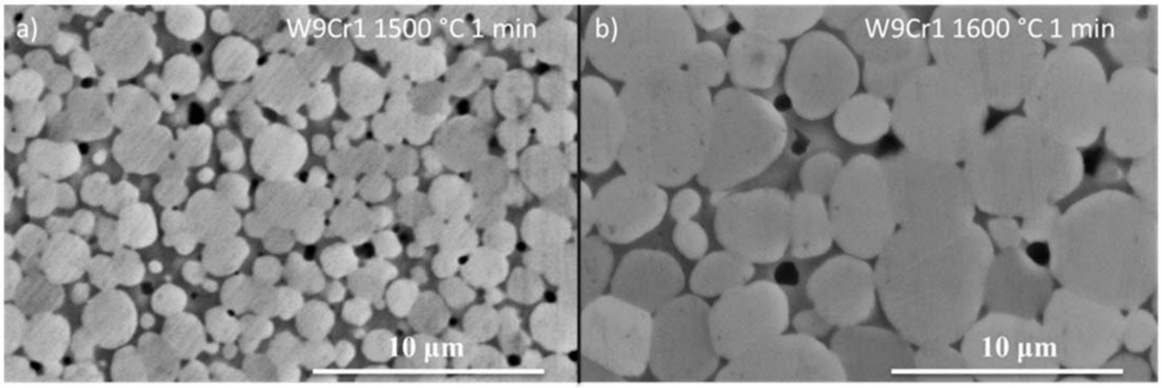

Figure 39 Liquid-phase sintering characteristics seen in a) W9Cr1 1500 °C 1 min and b) W9Cr1 1600 °C 1 min. Circular tungsten solid-solution spheroids are surrounded by a binder phase, which appears as dark gray regions.

Confirmation of a liquid present in W8Cr2 consolidated at 1600 °C for 1 min was shown in a drip, which came out of the specimen die (Figure 40). $Cr_{0.48}Fe_{0.52}$ has a melting temperature of 1627 °C, and evidence of a high Cr and Fe composition, Cr-44Fe-8W, was seen in the drip (Table 13). The majority of the drip is Cr-44Fe-8 with small regions containing higher concentrations of W (Figure 41). The µ-phase in the W-Cr-Fe system has a calculated melting temperature of 1527 °C, shown as an addition to the partial ternary liquidus projection (Figure 38). Less intermetallic phase remained in the specimen at 1600 °C due to the liquid-phase moving out of the compact and up the sides of the die due to reduced tolerances caused by thermal expansion. The spheroids evolved straight grain boundaries at 1700 °C due to the lack of binder remaining in the specimen at this temperature (Figure 26g).

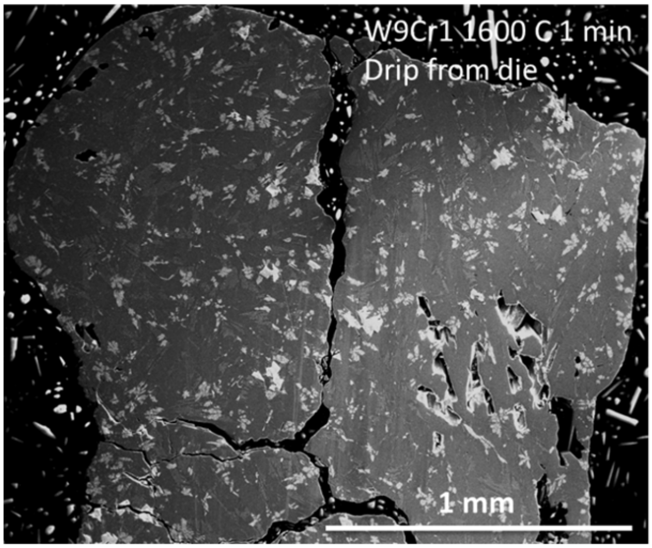

Figure 40 The polished solidified drip from specimen die of W9Cr1 consolidated at 1600 °C for 1 min, the majority of the drip was Cr-44Fe-8W.

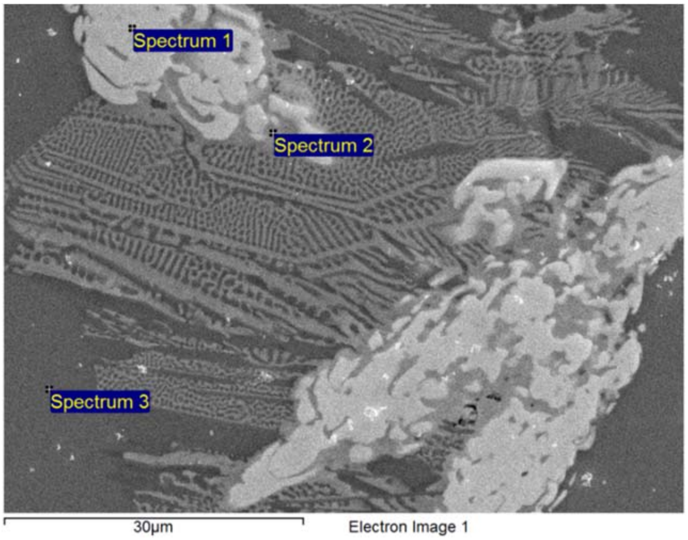

Figure 41 SEM micrograph of a drip from W9Cr1 consolidated at 1600 °C for 1 min, corresponding to EDS results in Table 13.

Table 13 EDS results in at.% of a drip from W9Cr1-1600C-1min-LP, corresponding to Figure 41.

Spectrum	Cr	Fe	W
1	27.19	8.53	64.28
2	19.58	47.13	33.29
3	47.71	44.28	8.01

4.6 Crystal Structure of Milled Powders and Consolidated Specimens

All specimens showed a bcc crystal structure based on peak position with the known lattice constant for tungsten. W+, W9Cr1, W8Cr2, W9Mo1, and W8Mo2 diffraction patterns are shown in Figure 42, Figure 43, Figure 44, Figure 45, and Figure 46, respectively. One pattern is of the powder and the other is from a specimen consolidated at 1100 °C for either 1 or 20 min. Lower peak intensity and broader peaks are seen in the powder specimen due to the smaller crystallite size and increased strain caused from mechanical alloying. Previous studies with the W-Ni-Fe system have shown that Ni and Fe dissolve into bcc tungsten producing a W-rich supersaturated solid solution.[132] A peak shift to the left can be seen in both the WCr and WMo alloys after consolidation, which is due to the formation of an intermetallic phase, which removes alloying elements out of the bulk, increasing the W content of the W solid solution and the bcc lattice parameter. The peak shift to the left is more predominant in W8Cr2 (Figure 44) and is attributed to the increased content of Cr in the bulk powder, which reduces the lattice parameter of the bcc structure. The intermetallic μ-phase is trigonal, which is highly distinguishable in the XRD patterns due to its complexity. In the specimen consolidated at 1400 °C for 20 min, the XRD pattern shows additional peaks that match the μ-phase, seen in Figure 47. The complex nature of these peaks corresponds to μ-phase studies by Joubert and Dupin,[117] with multiple peaks around 40 2θ in the MoCo system. Additional evidence that a μ-phase is present in specimens was found in TEM studies on W8Cr2 consolidated at 1100 °C for 20 min (Figure 48). Similar structures are seen in work on W_6Co_7 (μ-phase) by Carvalho and DeHosson,[133] and were used to help identify the μ-phase present in this study. The WMo specimens also showed additional peaks when consolidated (Figure 45) and the presence of the μ-phase was seen in EDS analysis (Table 9), as both W-Fe and Mo-Fe systems can form a μ-phase.[117]

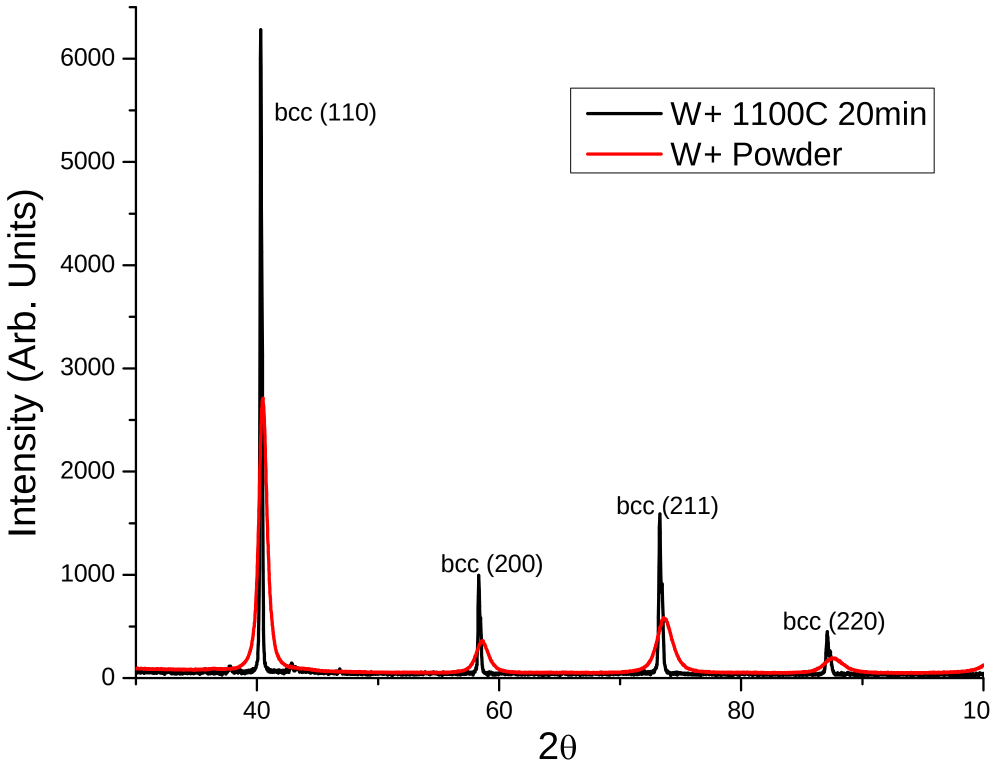

Figure 42 X-ray diffraction patterns for W+ powder and W+ consolidated at 1100 °C for 20 min dwell time. The y-axis has arbitrary units. The crystal structure is bcc and the corresponding alloy's bcc peaks are labeled.

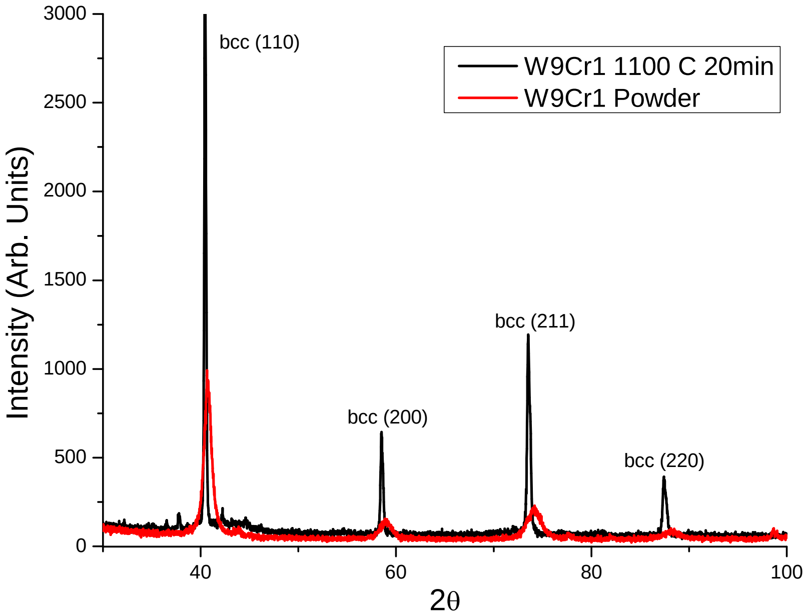

Figure 43 X-ray diffraction patterns for W9Cr1 powder and W9Cr1 consolidated at 1100 °C for 20 min dwell time. The y-axis has arbitrary units. The crystal structure is bcc and the corresponding alloy's bcc peaks are labeled.

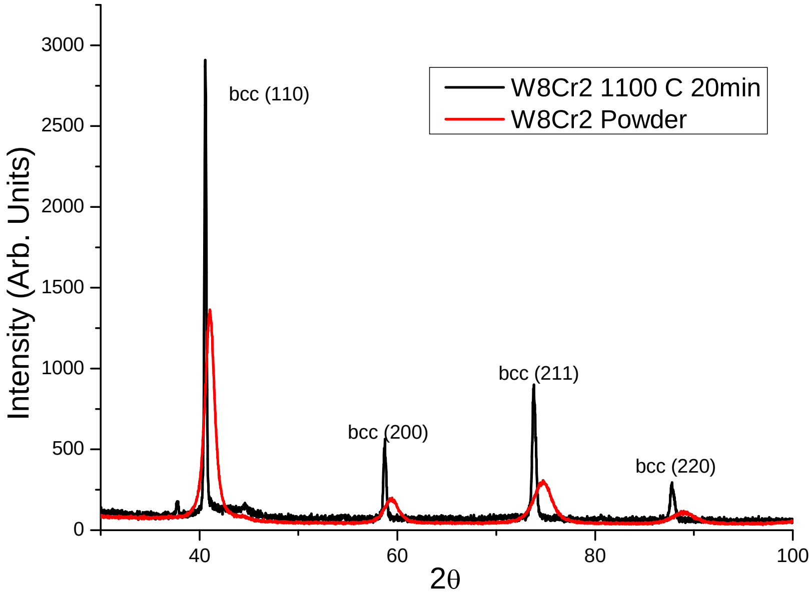

Figure 44 X-ray diffraction patterns for W8Cr2 powder and W8Cr2 consolidated at 1100 °C for 20 min dwell time. The y-axis has arbitrary units. The crystal structure is bcc and the corresponding alloy's bcc peaks are labeled.

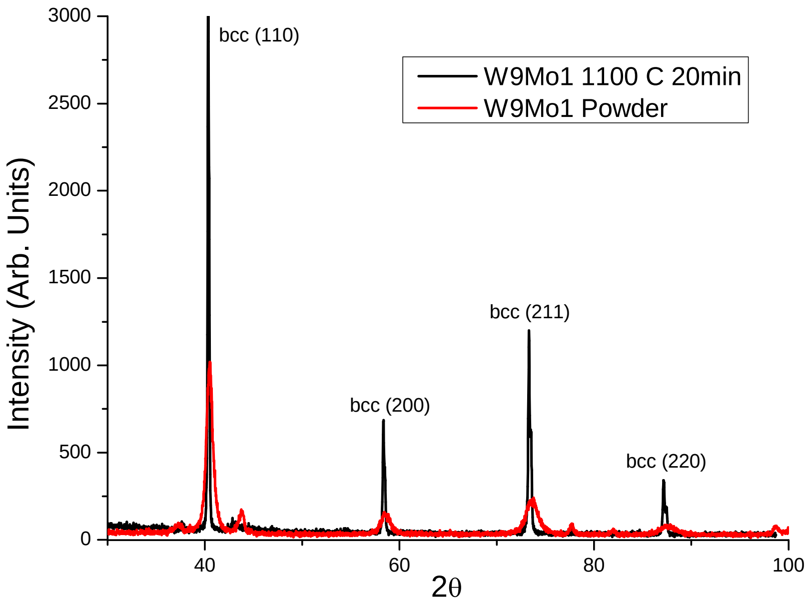

Figure 45 X-ray diffraction patterns for W9Mo1 powder and W9Mo1 consolidated at 1100 °C for 20 min dwell time. The y-axis has arbitrary units. The crystal structure is bcc and the corresponding alloy's bcc peaks are labeled.

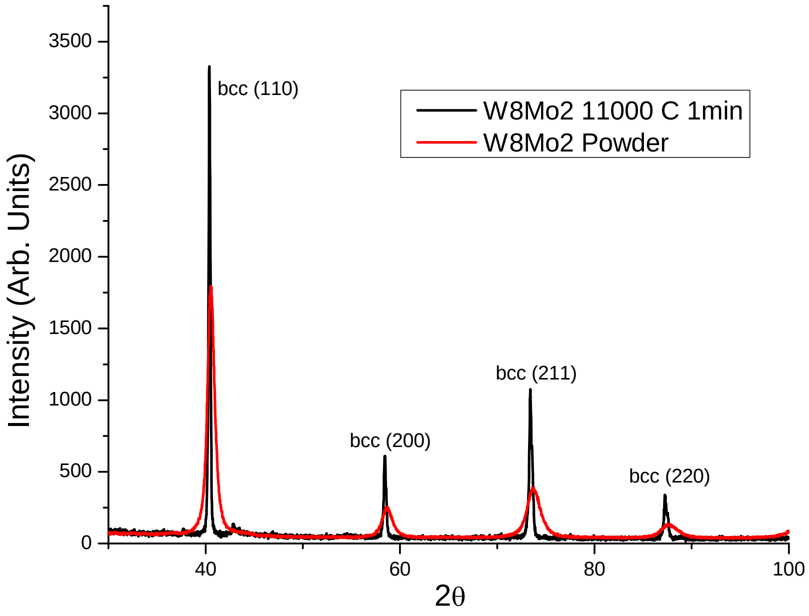

Figure 46 X-ray diffraction patterns for W8Mo2 powder and W8Mo2 consolidated at 1100 °C for 1 min dwell time. The y-axis has arbitrary units. The crystal structure is bcc and the corresponding alloy's bcc peaks are labeled.

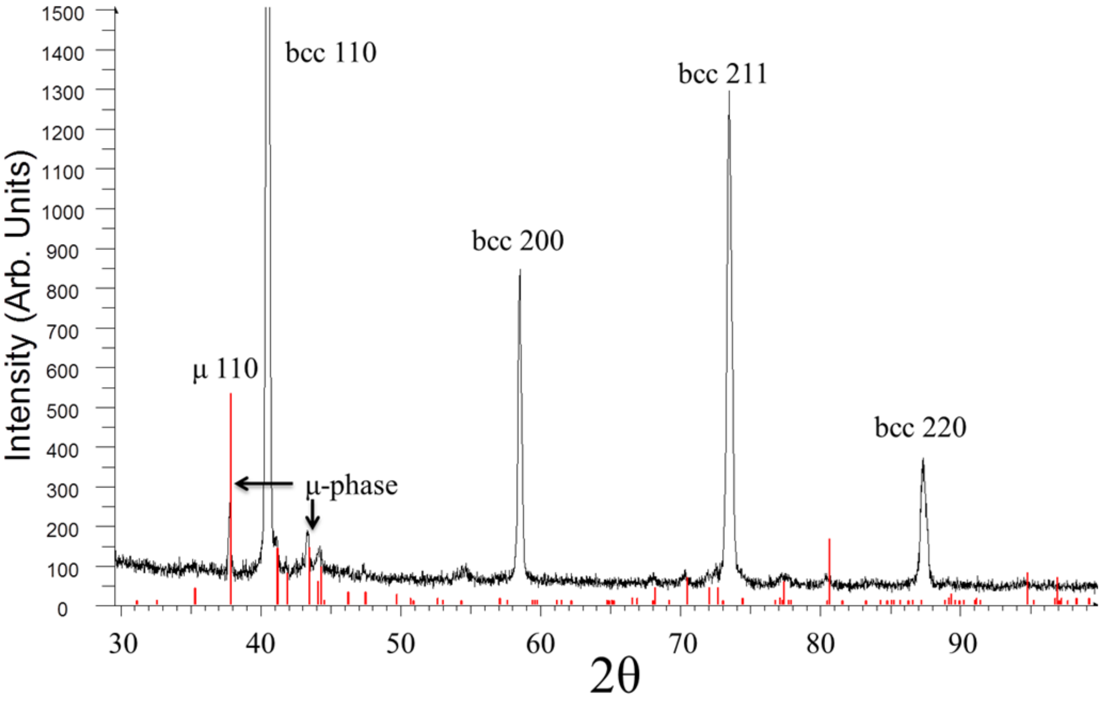

Figure 47 XRD pattern of W9Cr1 specimen consolidated at 1400 °C for 20 min, additional peaks correspond to a μ-phase; the diffraction pattern for $W_{5.1}Fe_{7.9}$ is seen in red. The y-axis has arbitrary units.

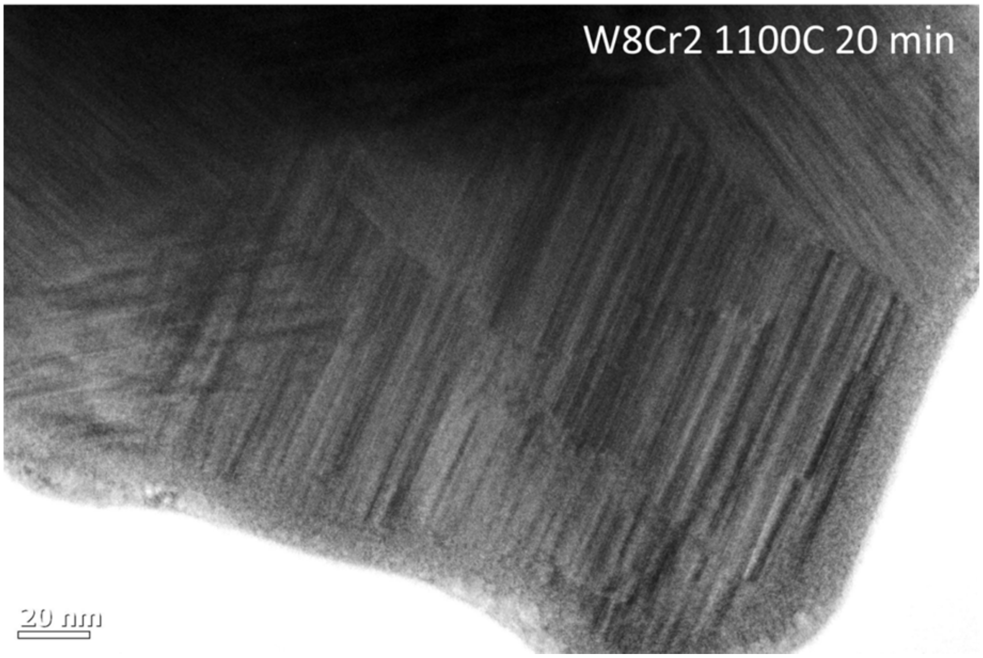

Figure 48 Transmission electron micrograph of the μ-phase found in W8Cr2 consolidated at 1100 C for 20 min.

4.6.1 Lattice-Parameter Determination

Figure 49 shows the HP specimen lattice parameters calculated by XRD and Vegard's Law from the powder compositions (Table 3). The similar lattice constants of pure W and Mo, 3.16 Å and 3.15 Å, respectively, result in similar lattice constants in the consolidated specimens. Conversely, the lattice constant of Cr is 2.88 Å and results in much lower lattice constants as suggested by Vegard's Law (Figure 49). All of the specimen powders have larger lattice parameters than suggested by Vegard's Law and the consolidated specimens deviated even further from Vegard's Law. Structural relaxation is seen with increased consolidated temperature; the lattice parameter increases. This relaxation is expected due to the induced lattice strain attributed to the high-energy ball milling. Previous studies have reported the expansion over-predicted lattice constants in annealed WCr alloys; however, the cause of the deviation has not been determined.[134] Deviation from Vegard's Law has been reported in several studies and Vegard's Law is now considered more of a generalization.[135, 136, 137, 138, 139] Lattice-parameter variation from Vegard's Law may be attributed to changes in the crystal structure.[140] In this study, all lattice parameters were calculated from bcc peaks, (200) and (211), though intermetallic phase trigonal peaks were present at low intensities in the XRD patterns of consolidated specimens. Due to the low peak intensity of the trigonal peaks present in diffraction patterns (Figure 45 and Figure 47), the lattice parameter calculated is from the W solid solution and may not be representative of the bulk composition.

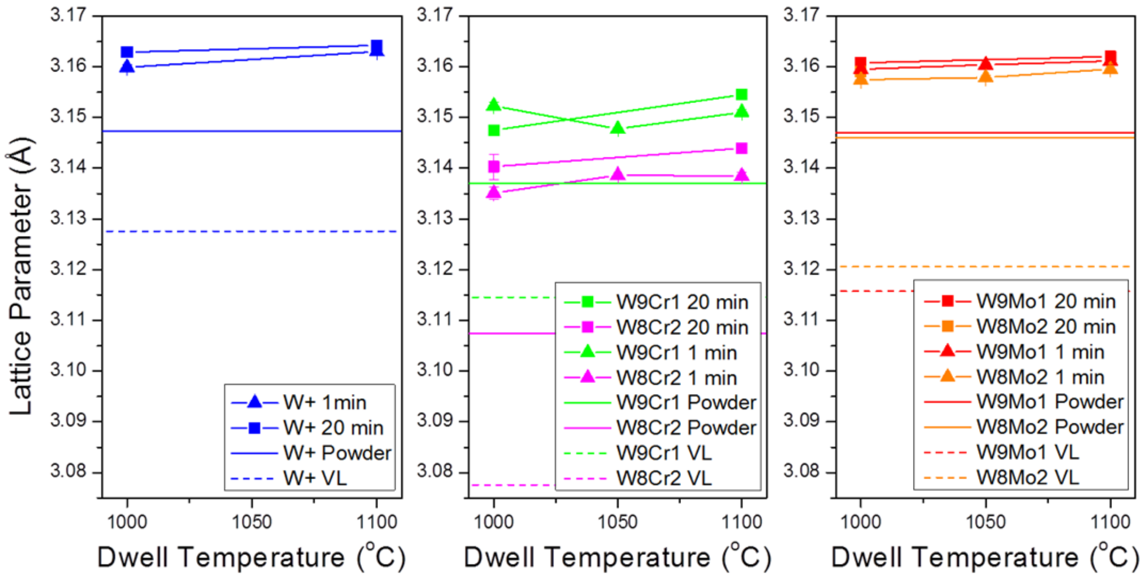

Figure 49 **Candidate alloy bcc lattice parameters for powder and consolidated specimen from XRD (200) and (211) peaks, along with lattice constants using Vegard's Law (labeled VL) calculated from powder EDS (Table 3).**

4.7 Grain Size Analysis

The grain size of selected LP specimens was measured using the line intercept method and plotted against dwell temperature as shown in Figure 50. Additional grain-size analysis using a circular intercept method was performed on the W solid solution phase in specimens at MIT. Grain size increased with increasing dwell temperature and dwell time. The grain size of specimens consolidated at 1200 °C is 1-2 µm, increasing to greater than 6 µm for the W9Cr1 alloy specimen consolidated at 1700 °C for 1 min. W+ had larger grain sizes than the W9Cr1 alloy at all temperatures for 1 and 20 min dwell times. The larger grain size of W+ specimens could be due to the larger initial grain size of the powder; however, Cr additions have also been known to be grain-growth inhibitors in tungsten carbide and WHAs containing Ni-Cr binder phases, as discussed in Section 4.3.[123, 124, 125, 141] To confirm grain-size measurements, complimentary analysis was performed at MIT on some selected overlapping specimens but excluding the intermetallic phase in measurements, which further reduced the grain-sizes calculated for specimens. From the MIT analysis, both W+ and W9Cr1 alloys had grain sizes below 1 μm for specimen consolidation temperatures below 1300 °C. A nanocrystalline grain size (79 nm) was achieved for W9Cr1 consolidated at 1100 °C for 1 min dwell time. For these LP specimens measured at MIT, the difference in grain size between W+ and W9Cr1 also increased with dwell temperature, in agreement with the observed increase in intermetallic phase separation with dwell temperature.

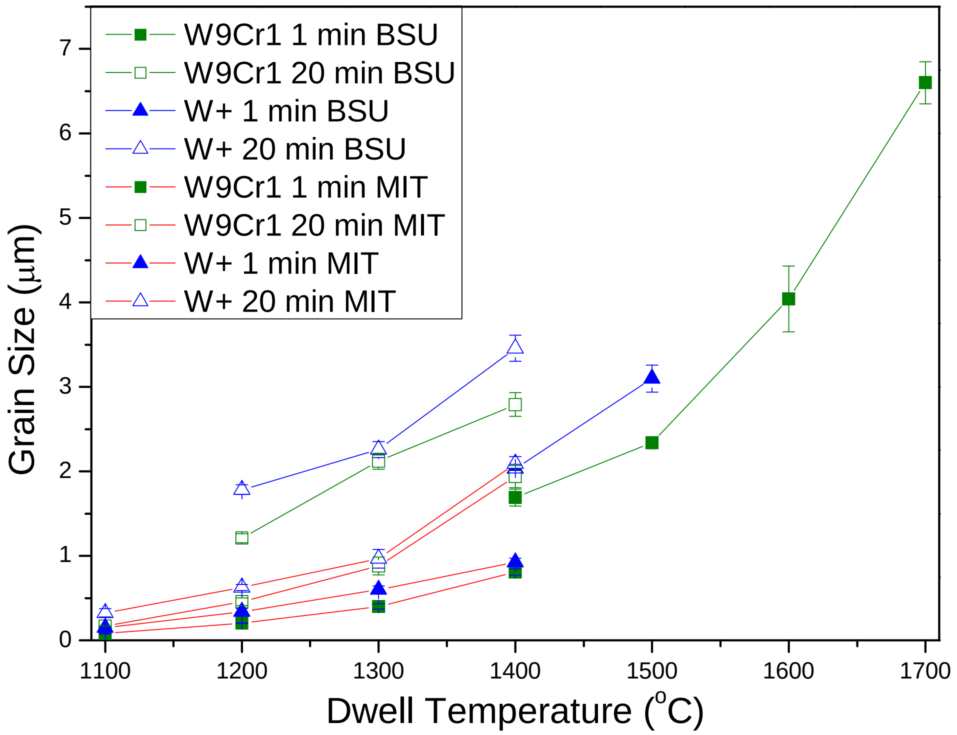

Figure 50 **Grain size vs. dwell temperature for LP W+ and W9Cr1 alloys. Lower grain sizes were calculated excluding the intermetallic phase. Specimen grain sizes increased with increased dwell temperature.**

4.7.1 Crystallite Size Analysis

X-ray diffraction peaks were also used to calculate the crystallite size using the Scherrer's formula for HP W+, W9Cr1, W8Cr2, W9Mo1, and W8Mo2 (Figure 51). The

Scherrer’s constant, *K* in Eq. (2), was varied from 0.9 to 1, to estimate an error in the crystallite size. Crystallite size estimates for consolidated HP specimens were all below 50 nm, in contrast to the measured grain sizes for the LP specimens (Figure 50). Increased crystallite size is seen with increasing temperature and dwell time. The smallest crystallite size estimate of 21.5 nm was the W8Cr2 alloy specimen consolidated at 1000 °C for 1 min dwell time.

Transmission electron micrographs of a few selected specimens were obtained to confirm nanocrystalline microstructures as calculated by the Scherrer’s equation in the HP series. SAED patterns of W8Cr2 and W9Cr1 consolidated at 1100 °C for 1 min dwell time show a bcc polycrystalline structure and corresponding micrographs show that the grain size is below 100 nm (Figure 52). The TEM micrographs confirm that the crystallite size of the WCr alloy was nanocrystalline and appeared consistent with the calculated crystallite size from XRD data. A SAED pattern forms Debye rings when multiple grains are included in the aperture. The Debye rings, shown in Figure 53, were determined to be bcc in nature through diffraction analysis of the plane *d*-spacings, which is consistent with XRD results.

Scanning transmission electron micrographs of W9Cr1 and W8Cr2 consolidated at 1100 °C for 1 min dwell time offer a different perspective of the crystallite size with increased contrast of the nanocrystalline microstructures seen in these alloys. Crystallite sizes below 100 nm can be seen in both W9Cr1 and W8Cr2 alloys consolidated at 1100 °C with a 1 min dwell time, as seen in Figure 54.

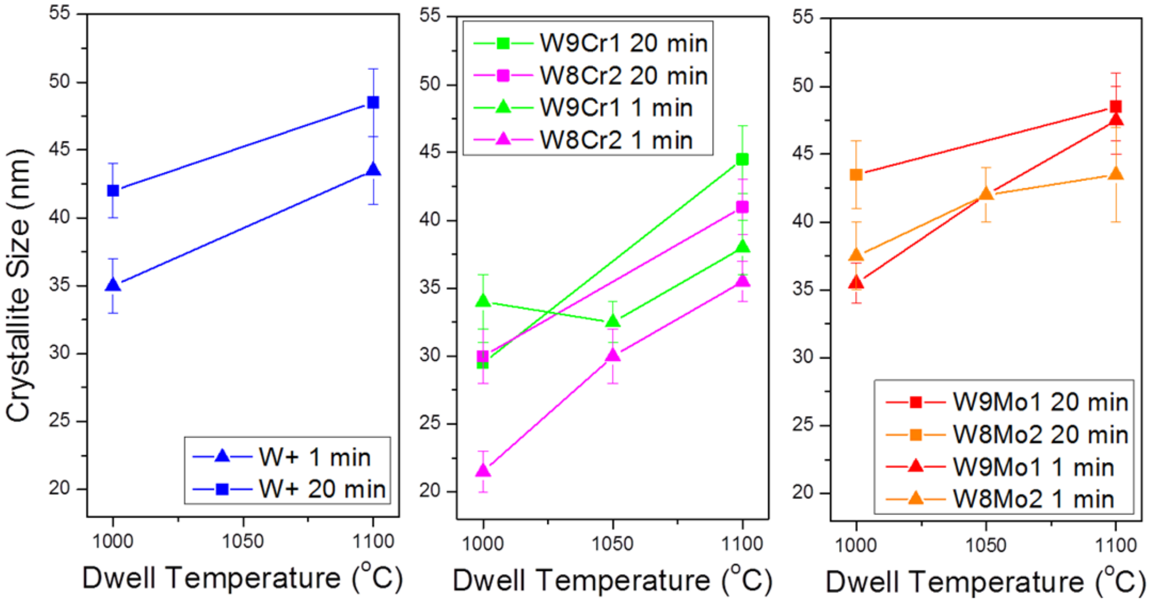

Figure 51 Crystallite size (nm) estimates from x-ray diffraction peaks using the Scherrer's equation (Eq. 2).

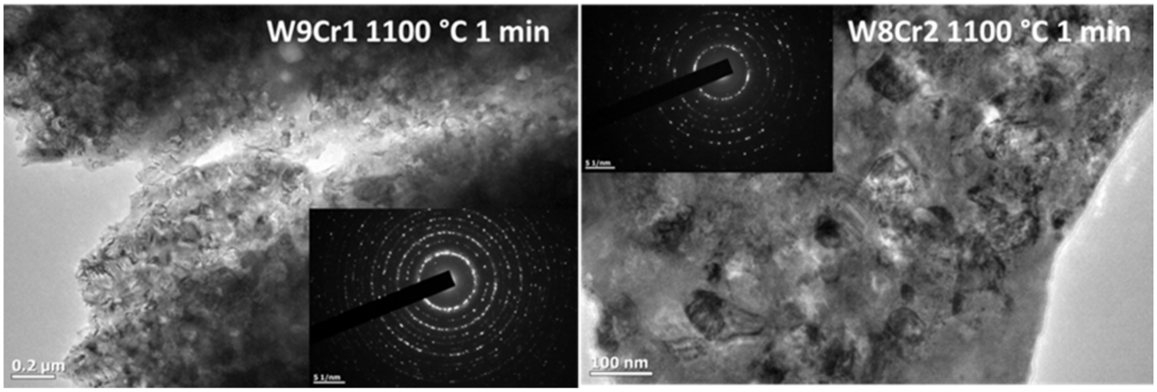

Figure 52 Transmission electron micrographs and SAED patterns of W8Cr2 1100 °C 1 min (left) and W9Cr1 1100 °C 1 min (right). SAED patterns show a bcc crystal structure is present. Debye rings seen in the SAED indicate multiple grains were included in the selected area.

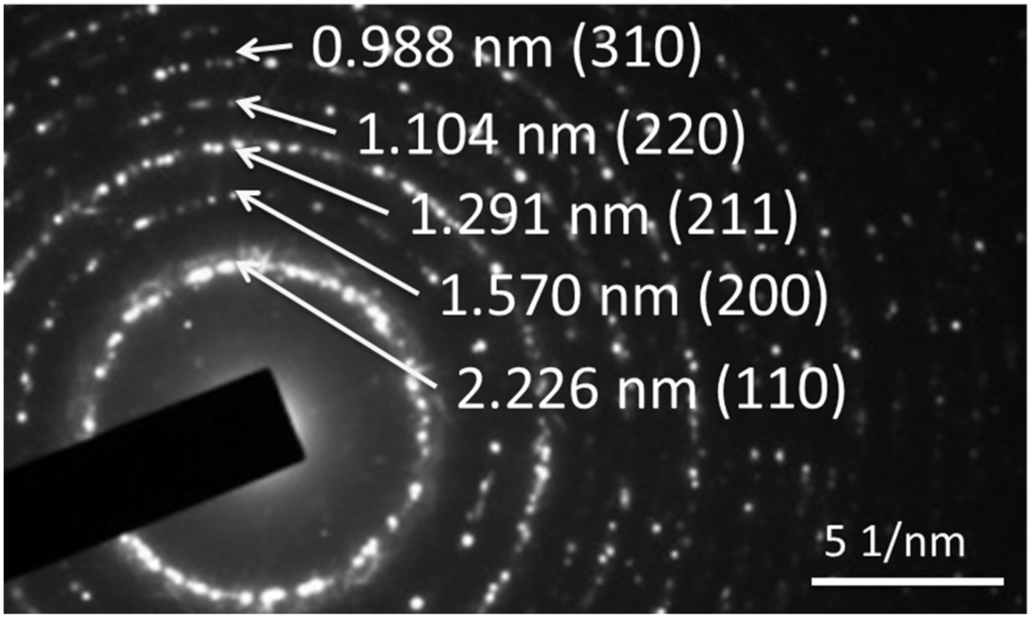

Figure 53 SAED of W9Cr1 1100 °C 1 min with *d*-spacings and bcc planes identified for the Debye rings.

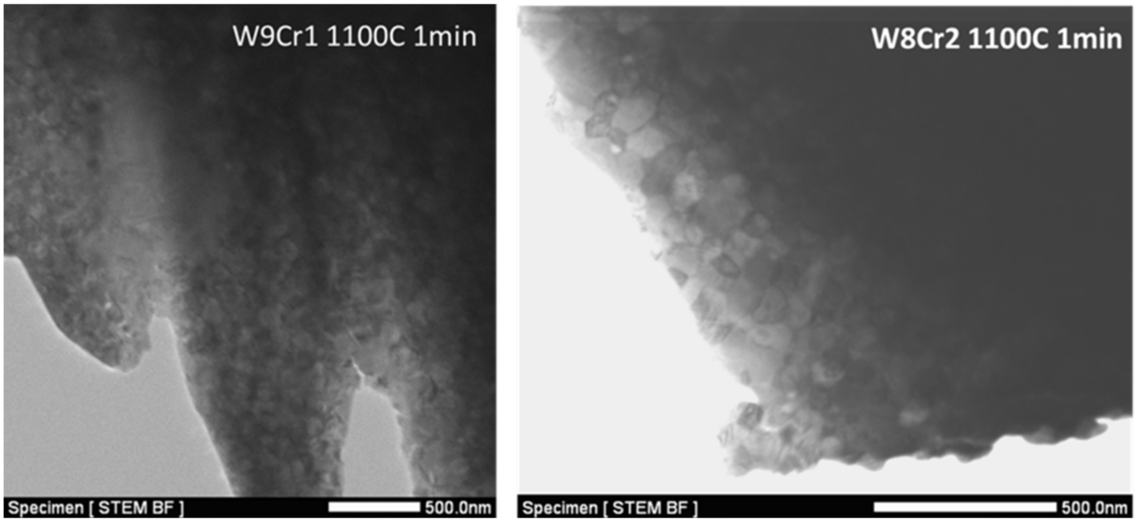

Figure 54 Scanning transmission electron micrographs of nanocrystalline microstructures in W9Cr1 (left) and W8Cr2 (right) consolidated at 1100 °C for 1 min dwell time.

4.7.2 Grain Size vs. Hardness

Vickers microhardness as a function of grain size for LP specimens analyzed with the line intercept method is shown in Figure 55. Generally, the expected behavior was observed and larger grain sizes resulted in lower hardness. The W9Cr1 alloy had higher hardnesses for comparable grain size, 2-3 μm, when compared to the W+ alloy. The increased hardness of W9Cr1 over W+ could be the result of a higher intermetallic phase fraction in consolidated compacts. Previous reports on W-Ni-Cr alloys have shown increased hardness in the intermetallic binder phase, ~500 HV, over the bulk W solid solution, ~400 HV.[124] Vickers microhardnesses reported in this study are higher than the W-Ni-Cr alloy reported by Srikanth and Upadhyaya[124] due to the smaller grain sizes in W+, WCr, and WMo specimens. Vickers microhardness of binder phase and W solid solution were not separated in this report due to grain sizes being too small to indent each phase separately. In another study, the hardness of tungsten processed by high-pressure torsion was close to 11 GPa, tested by nanoindentation. The high hardness is due to the nanocrystalline grain size produced by this processing method.[63] Collaborators at the ARL performed nanoindentation measurements on several HP W9Cr1 and W8Cr2 specimens and results ranged between 12-19 GPa.

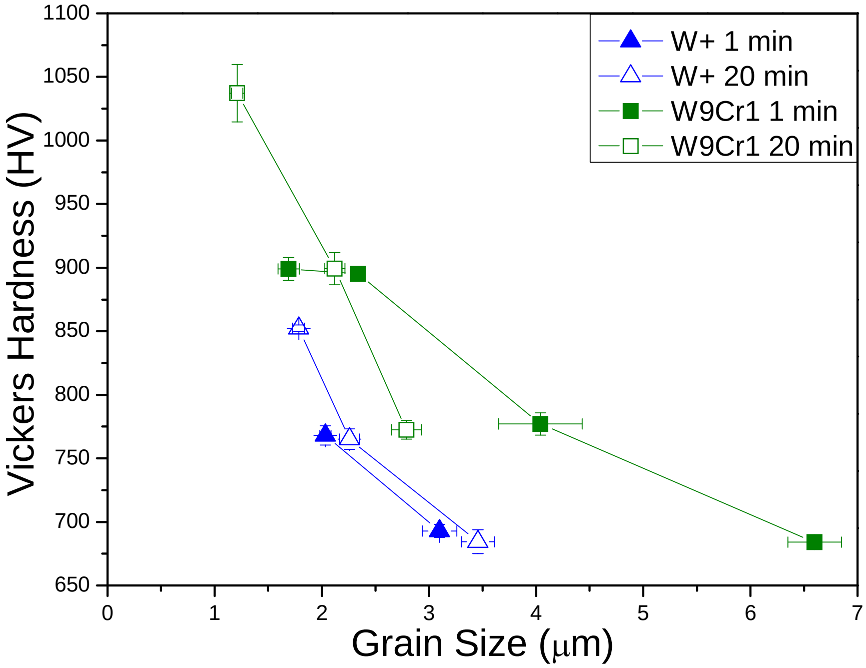

Figure 55 **Grain size vs. Vickers hardness for selected LP W+ and W9Cr1 for 1 and 20 min dwell times. Grain size increases corresponded to decreased hardnesses in both W+ and W9Cr1.**

4.7.3 Hall-Petch Relationship

Hardness vs. grain size$^{-1/2}$ can provide a linear relationship, which can illustrate the potential benefit of reducing the grain size of these alloys. A plot of the Vickers microhardness and the inverse root of grain size measured by line intercept at MIT or the inverse root of crystallite size by the Scherrer's formula is shown in Figure 56. Increased hardness was seen in specimens with reduced grain size until the porosity of the specimens became a factor at temperatures below 1100 °C. Specimens consolidated in the LP series showed a linear relationship with hardness and grain size, linear fits are shown for W+ 1 min, W9Cr1 20 min and previous work on nanocrystalline tungsten by Vashi *et al.*[142] Increased hardness was seen in W+ and W9Cr1 alloys specimens that had lower grain sizes in accordance to the Hall-Petch relationship. The highest hardness seen in the LP series was 1325 HV for W9Cr1 consolidated at 1100 °C for 20 min, compared to the highest hardness of the HP series, which was 1520 HV for W8Cr2 consolidated at 1100 °C for 1 min. The HP W8Cr2 alloy specimen had some remaining porosity, 1.38%, which could be reduced if higher temperatures were used during consolidation; however, the trend of the HP series shows a large grouping of specimens with similar hardnesses and grain sizes, ~1350 HV and 40 nm.

Reduction in grain size may not be achievable if powder crystallite size remains the same. At low temperatures, reduction in grain growth during consolidation is possible, but full densification, from powder to solid compact, may not be achievable. Further reduction in the grain size of initial alloy powders could reduce the grain size in consolidated specimens, increasing the hardness and potentially the mechanical properties of these candidate alloys. Production of an amorphous tungsten alloy powder could likely result in large increases in hardness for consolidated specimens and improve their deformation behavior for KEPs.

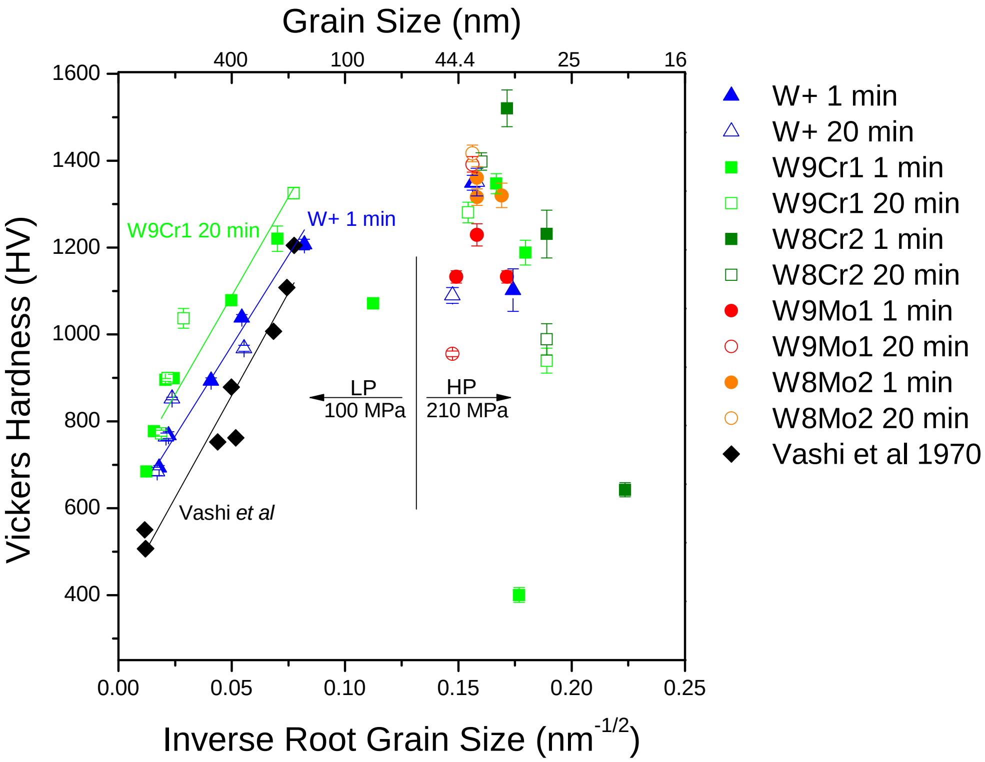

Figure 56 **Hardness vs. inverse root grain size for HP and LP specimens series of W+, WCr and WMo alloys. Included in the plot is previous work on nanocrystalline tungsten powders consolidated by Vashi *et al*.[142] Linear fittings are shown for W9Cr1 20 min, W+ 1 min, and nanocrystalline tungsten by Vashi *et al*.[142]**

CHAPTER FIVE: CONCLUSIONS

New nanocrystalline W-alloys were produced through high charge ratio mechanical alloying and pulsed electric current sintering. Increases in hardness and compressive strength over baseline W-alloys up to 275% were seen. W8Cr2 consolidated at 1100 °C for 1 min dwell time at 210 MPa had the highest hardness, 1520 HV, even with 1.63% porosity remaining. Higher temperatures during consolidation of W8Cr2 could potentially improve the hardness by lowering the porosity remaining after consolidation. Several alloys, including W9Cr1, W8Cr2, W8Mo2, and W+ had hardnesses above ~1340 HV; if ballistic performance were solely attributed to the materials hardness, these alloys have the potential to be effective KEPs. Ballistic testing of these alloys will ultimately determine whether they are suitable materials for KEPs.

Long hold times are not required for full densification of WMo and WCr alloys at 1050 °C and 1200 °C, respectively. WCr alloys require increased temperature to fully consolidate, and at 1200 °C the pressure applied during sintering becomes a nonfactor for porosity but can affect the hardness of the consolidated specimens. Increasing pressure from 100 MPa to 210 MPa increased the hardness in W+ and W9Cr1 alloys by 11-25%. Lowering porosity with increased temperature increased the hardness until significant grain growth occurred at 1100 °C for W+ and 1200 °C for W9Cr1.

Alloying elements provided enhanced sintering with the development of an intermetallic phase, which filled in pores and spaces between powder particles. At higher temperatures, the intermetallic phase melting point was reached and liquid-phase sintering was observed. Limited solubility resulted in an intermetallic phase compositional evolution as the alloying elements diffused out of the bulk and the remaining allowable concentrations for a tungsten solid solution were seen. Optimization of the intermetallic phase to promote homogeneous microstructures could be accomplished by reducing media contamination to improve powder uniformity, though this has proven difficult when alloying to promote amorphization. Lower intermetallic phase fractions would raise the overall density of the compact, but may result in reduced performance since the intermetallic phase is acting as a binder between the powder particles, especially at lower temperatures of consolidation.

Initial nanocompression testing performed by the ARL has shown that W9Cr1 deforms by shearing. This shearing could result in the chiseling of the munitions' tip during penetration and improve the ballistic performance of these alloys as KEPs. The ballistic performance of a few selected specimens is being currently investigated by the ARL.

PECS was a fast method for consolidation that can avoid the conventional final stage sintering effects of rapid grain growth, allowing the nanocrystalline microstructure to remain from specimen powders. Amorphous WHA powder could have the same success in avoiding crystallization and grain growth during consolidation with PECS, but the challenge of producing fully amorphous powders must first be addressed prior to optimizing consolidation parameters.

CHAPTER SIX: FUTURE WORK

High hardnesses seen in the specimens could be beneficial for many applications; however, ballistic impact can cause shattering and fracturing of very hard materials and could make them perform poorly in penetration studies. Ballistic testing is required to optimize the hardness and avoid shattering on impact. Increasing the bulk specimen size is necessary to test the change in up-scaling the materials for production. Testing these materials in high strain-rate dynamic conditions is essential to determine if they will be effective KEPs. Follow up testing of this nature is planned by the ARL.

Increasing the specimen size also increases the number of defects that may be present in the material; therefore, it is important to reduce the number of defects created during processing by optimizing milling and sintering parameters. Particle uniformity is an important part of milling and sintering studies. By increasing the particle uniformity in the powders, more uniform and homogenous microstructures can be produced and potentially improve performance.

Increasing the number of constituents in the alloy could lead to amorphorization, leading to improved mechanical properties and potentially reduce the grain size in sintered compacts. Additionally, combining an amorphous powder with the nanocrystalline powders studied in this report could provide more tailorable properties to improve the ballistic performance.

Comparison of WMo and WCr alloys as KEPs can be performed after their ballistic testing. Traditional WHA KEPs deform through uniform bulk deformation; however, the nanocrystalline microstructures seen in these alloys may cause shear band formation to occur and cause the chiseling that is desirable. Previous studies with U-8Mo have shown that chiseling will occur in this alloy.[3] The addition of Mo into the alloy may promote the chiseling in the WMo series of alloys and their ballistic performance should be evaluated in side-by-side comparisons. The homogeneity of these W-based alloys, WCr and WMo, needs to be evaluated for its effect on the ballistic performance. Variations in intermetallic phase development in WCr and WMo alloys may cause differences in the ballistic performance. Optimizing the compositions of the intermetallic phase and reducing inhomogeneity could result in improved ballistic performance. DU alloys have more homogenous microstructures and outperform WHAs by 10% in ballistic studies.[1] The homogeneity in DU alloys may be a significant factor for its improved performance.

Additional analysis on the sintering mechanisms could be performed to understand specifically what diffusion paths are occurring in WCr and WMo alloys. Kinetic analysis could be obtained through additional sintering studies to carefully examine the activation energy of sintering in these alloys and could be compared with literature to determine the diffusion path. Additionally, PECS activation energies could be compared to activation energies found with dilatometry and an estimate of which diffusion path is more prevalent in PECS could be determined.

REFERENCES

1. W. D. Cai, Y. Li, R. J. Dowding, F. A. Mohamed, and E. J. Lavernia, "A Review of Tungsten-Based Alloys as Kinetic Energy Penetrator Materials," *Reviews in Particulate Materials,* 3 [1] 71-131 (1995).
2. L. S. Magness, "High-Strain Rate Deformation Behaviors of Kinetic-Energy Penetrator Materials During Ballistic Impact," *Mechanics of Materials,* 17 [2-3] 147-54 (1994).
3. L. S. Magness, D. Kapoor, and R. Dowding, "Novel Flow-Softening and Flow-Anisotropy Approaches to Developing Improved Tungsten Kinetic-Energy Penetrator Materials," *Materials and Manufacturing Processes,* 10 [3] 531-40 (1995).
4. B. G. Spratt, "Depleted Uranium Munitions: Where are We Now?," *Journal of Radiological Protection,* 22 [2] 125-30 (2002).
5. A. Upadhyaya, "Tungsten Heavy Alloys for Ordnance and Thermal Management Applications," *Transactions of the Indian Institute of Metals,* 55 [1-2] 51-69 (2002).
6. A. Bose and R. M. German, "Matrix Composition Effects on the Tensile Properties of Tungsten-Molybdenum Heavy Alloys," *Metallurgical Transactions A,* 21 [5] 1325-27 (1990).
7. E. Lassner and W. D. Schubert, "Tungsten: Properties, Chemistry, Technology of the Element, Alloys, and Chemical Compounds." Kluwer Academic/Plenum Publishers: New York, (1999).
8. W. Klement, R. H. Willens, and P. Duwez, "Non-Crystalline Structure in Solidified Gold-Silicon Alloys," *Nature,* 187 [4740] 869-70 (1960).
9. C. A. Schuh, T. C. Hufnagel, and U. Ramamurty, "Overview No.144 - Mechanical Behavior of Amorphous Alloys," *Acta Materialia,* 55 [12] 4067-109 (2007).
10. W. H. Zachariasen, "The Atomic Arrangement in Glass," *Journal of the American Chemical Society,* 54 [10] 3841-51 (1932).

11. D. B. Miracle, W. S. Sanders, and O. N. Senkov, "The Influence of Efficient Atomic Packing on the Constitution of Metallic Glasses," *Philosophical Magazine,* 83 [20] 2409-28 (2003).

12. D. B. Miracle, O. N. Senkov, W. S. Sanders, and K. L. Kendig, "Structure-Forming Principles for Amorphous Metals," *Materials Science and Engineering A,* 375 [1] 150-56 (2004).

13. C. Suryanarayana and A. Inoue, "Bulk Metallic Glasses," pp. 27. CRC Press: Boca Raton, FL, (2011).

14. O. N. Senkov and D. B. Miracle, "Effect of the Atomic Size Distribution on Glass Forming Ability of Amorphous Metallic Alloys," *Materials Research Bulletin,* 36 [12] 2183-98 (2001).

15. A. C. Lund and C. A. Schuh, "Molecular Simulation of Amorphization by Mechanical Alloying," *Acta Materialia,* 52 [8] 2123-32 (2004).

16. J. H. Li, Y. Dai, Y. Y. Cui, and B. X. Liu, "Atomistic Theory for Predicting the Binary Metallic Glass Formation," *Materials Science and Engineering R,* 72 [1-2] 1-28 (2011).

17. W. L. Johnson and A. R. Williams, "Structure and Properties of Transition-Metal-Metalloid Glasses Based on Refractory Metals," *Physical Review B,* 20 [4] 1640-55 (1979).

18. R. Yoshimoto, Y. Nogi, R. Tamura, and S. Takeuchi, "Fabrication of Refractory Metal Based Metallic Glasses," *Materials Science and Engineering A,* 449 [1] 260-63 (2007).

19. M. Ohtsuki, R. Tamura, S. Takeuchi, S. Yoda, and T. Ohmura, "Hard Metallic Glass of Tungsten-Based Alloy," *Applied Physics Letters,* 84 [24] 4911-13 (2004).

20. O. Younes, L. Zhu, Y. Rosenberg, Y. Shacham-Diamand, and E. Gileadi, "Electroplating of Amorphous Thin Films of Tungsten/Nickel Alloys," *Langmuir,* 17 [1] 8270-75 (2001).

21. M. C. Chou, C. F. Chu, and S. T. Wu, "Phase Transformations of Electroplated Amorphous Iron-Tungsten-Carbon Film," *Materials Chemistry and Physics,* 78 [1] 59-66 (2003).

22. M. Emam-Ismail, E. R. Shaaban, M. El-Hagary, and I. Shaltout, "Optical Investigation of Electron-Beam-Deposited Tungsten-Tellurite $(TeO_2)_{100-x}(WO_3)_x$ Amorphous Films," *Philosophical Magazine,* 90 [25] 3499-509 (2010).

23. Y. Abe, N. Ishiyama, H. Kuno, and K. Adachi, "Amorphous Indium Tungsten Oxide Films Prepared by DC Magnetron Sputtering," *Journal of Materials Science,* 40 [7] 1611-14 (2005).

24. N. Radic, A. Tonejc, J. Ivkov, P. Dubcek, S. Bernstorff, and Z. Medunic, "Sputter-Deposited Amorphous-like Tungsten," *Surface & Coatings Technology,* 180 [1] 66-70 (2004).

25. R. F. Zhang, Y. X. Shen, H. F. Yan, and B. X. Liu, "Formation of Amorphous Alloys by Ion Beam Mixing and Its Multiscale Theoretical Modeling in the Equilibrium Immiscible Sc-W System," *Journal of Physical Chemistry B,* 109 [10] 4391-7 (2005).

26. T. H. Courtney, "Processing, Structure and Properties of Heavily Deformed In Situ Composites." in. Defense Technical Information Center, Ft. Belvoir, 1991.

27. T. H. Courtney, "Structure, Properties, and Processing of Two-Phase Crystalline-Amorphous W-Based Alloys." in. Defense Technical Information Center, Ft. Belvoir, 2000.

28. S. Mi and T. H. Courtney, "Processing, Structure and Properties of Ni-W Alloys Fabricated by Mechanical Alloying and Hot-Isostatic Pressing," *Scripta Materialia,* 38 [4] 637-44 (1998).

29. C. G. Mukira and T. H. Courtney, "Structure and Properties of Mechanically Alloyed and Consolidated Ni-W(Fe) Alloys," United States, (1995).

30. T. H. Courtney and Z. Wang, "Grinding Media Wear During Mechanical Alloying of Ni-W Alloys in a Spex Mill," *Scripta Metallurgica Et Materialia,* 27 [6] 777-82 (1992).

31. T. Car, N. Radic, J. Ivkov, E. Babic, and A. Tonejc, "Crystallization Kinetics of Amorphous Aluminum-Tungsten Thin Films," *Applied Physics A: Materials Science & Processing,* 68 [1] 69-73 (1999).

32. F. Liu, F. Sommer, and E. J. Mittemeijer, "Determination of Nucleation and Growth Mechanisms of the Crystallization of Amorphous Alloys; Application to Calorimetric Data," *Acta Materialia,* 52 [11] 3207-16 (2004).

33. D. M. Minic and B. Adnadevic, "Mechanism and Kinetics of Crystallization of Alpha-Fe in Amorphous $Fe_{81}B_{13}Si_4C_2$ Alloy," *Thermochimica Acta,* 474 [1-2] 41-46 (2008).

34. W.-n. Myung, S. Yang, H. Kimura, and T. Masumoto, "Crystallization of Amorphous Metal Matrix Composites," *Materials Science and Engineering,* 97 [1] 259-64 (1988).

35. E. Piorkowska, A. Galeski, and J. M. Haudin, "Critical Assessment of Overall Crystallization Kinetics Theories and Predictions," *Progress in Polymer Science,* 31 [6] 549-75 (2006).

36. C. Thompson and F. Spaepen, "On the Approximation of the Free Energy Change on Crystallization," *Acta Metallurgica,* 27 [12] 1855-59 (1979).

37. F. Spaepen, "A Microscopic Mechanism for Steady State Inhomogeneous Flow in Metallic Glasses," *Acta Metallurgica,* 25 [4] 407-15 (1977).

38. K. M. Flores, "Structural Changes and Stress State Effects during Inhomogeneous Flow of Metallic Glasses," *Scripta Materialia,* 54 [3] 327-32 (2006).

39. C. A. Schuh, T. C. Hufnagel, and U. Ramamurty, "Mechanical Behavior of Amorphous Alloys," *Acta Materialia,* 55 [12] 4067-109 (2007).

40. C. E. Packard and C. A. Schuh, "Initiation of Shear Bands Near a Stress Concentration in Metallic Glass," *Acta Materialia,* 55 [16] 5348-58 (2007).

41. H. Gleiter, "Nanocrystalline Materials," *Progress in Materials Science,* 33 [4] 223-315 (1989).

42. E. Arzt, "Size Effects in Materials Due to Microstructural and Dimensional Constraints: A Comparative Review," *Acta Materialia,* 46 [16] 5611-26 (1998).

43. V. Richter and M. V. Ruthendorf, "On Hardness and Toughness of Ultrafine and Nanocrystalline Hard Materials," *International Journal of Refractory Metals & Hard Materials,* 17 [1] 141-52 (1999).

44. C. S. Pande, R. A. Masumura, and P. M. Hazzledine, "Yield Stress of Nanocrystalline Materials," *Materials Physics and Mechanics,* 5 [1] 16-22 (2002).

45. M. A. Meyers, A. Mishra, and D. J. Benson, "Mechanical Properties of Nanocrystalline Materials," *Progress in Materials Science,* 51 [4] 427-556 (2006).

46. B. E. Schuster, J. P. Ligda, Z. L. Pan, and Q. Wei, "Nanocrystalline Refractory Metals for Extreme Condition Applications," *JOM,* 63 [12] 27-31 (2011).

47. R. A. Adrievskii, "Properties of Nanocrystalline Refractory Compounds (review)," *Powder Metallurgy and Metal Ceramics,* 32 [11-12] 935-41 (1994).

48. Q. Wei, B. E. Schuster, S. N. Mathaudhu, K. T. Hartwig, L. J. Kecskes, R. J. Dowding, and K. T. Ramesh, "Dynamic Behaviors of Body-Centered Cubic Metals with Ultrafine Grained and Nanocrystalline Microstructures," *Materials Science and Engineering A,* 493 [1-2] 58-64 (2008).

49. J. R. Trelewicz and C. A. Schuh, "The Hall-Petch Breakdown at High Strain Rates: Optimizing Nanocrystalline Grain Size for Impact Applications," *Applied Physics Letters,* 93 [17] 1-3 (2008).

50. C. Suryanarayana and C. C. Koch, "Nanocrystalline Materials - Current Research and Future Directions," *Hyperfine Interactions,* 130 [1] 5 (2000).

51. M. Krasnowski and T. Kulik, "Nanocrystalline or Amorphous Matrix $Al_60Fe_{15}Ti_1$(Co/Mg/Zr)-5%B Composites Produced by Consolidation of Mechanically Alloyed Powders - Lightweight Materials with High Hardness," *Intermetallics,* 28 [1] 120-27 (2012).

52. D. P. Harvey, R. Kalyanaraman, and T. S. Sudarshan, "Consolidation and Mechanical Behaviour of Nanocrystalline Iron Powder," *Materials Science and Technology,* 18 959-63 (2002).

53. S. H. Yoo, T. S. Sudarshan, K. Sethuram, G. Subhash, and R. J. Dowding, "Consolidation and High Strain Rate Mechanical Behavior of Nanocrystalline Tantalum Powder," *Nanostructured Materials,* 12 [1-4] 23-28 (1999).

54. A. Antolak-Dudka, M. Krasnowski, and T. Kulik, "Nanocrystalline Ni_3Al Intermetallic Produced by Hot-Pressing Consolidation of Mechanically Alloyed Powders," *Intermetallics,* 42 [2] 41-44 (2013).

55. A. Singh and S. P. Harimkar, "Spark Plasma Sintering of *in situ* and *ex situ* Iron-Based Amorphous Matrix Composites," *Journal of Alloys and Compounds,* 497 [1-2] 121-26 (2010).

56. D. Roy, D. Chakravarty, R. Mitra, and I. Manna, "Effect of Sintering on Microstructure and Mechanical Properties of Nano-TiO_2 Dispersed $Al_{65}Cu_{20}Ti_{15}$ Amorphous/Nanocrystalline Matrix Composite," *Journal of Alloys and Compounds,* 460 [1-2] 320-25 (2008).

57. M. T. Stawovy and A. O. Aning, "Processing of Amorphous Fe-W Reinforced Fe Matrix Composites," *Materials Science and Engineering A,* 256 [1-2] 138-43 (1998).

58. C. K. Kim, S. Lee, S. Y. Shin, and D. H. Kim, "Microstructure and Mechanical Properties of Cu-Base Amorphous Alloy Matrix Composites Consolidated by Spark Plasma Sintering," *Materials Science and Engineering A,* 449 [1] 924-28 (2007).

59. R. D. Conner, R. B. Dandliker, and W. L. Johnson, "Mechanical Properties of Tungsten and Steel Fiber Reinforced $Zr_{41.25}Ti_{13.75}Cu_{12.5}Ni_{10}Be_{22.5}$ Metallic Glass Matrix Composites," *Acta Materialia,* 46 [17] 6089-102 (1998).

60. K. Cho, L. Kecskes, R. Dowding, B. Schuster, Q. Wei, and R. Z. Valiev, "Nanocrystalline and Ultra-Fine Grained Tungsten for Kinetic Energy Penetrator and Warhead Liner Applications." in. Defense Technical Information Center, Ft. Belvoir, 2007.

61. F. A. Khalid and M. R. Bhatti, "Microstructure and Properties of Sintered Tungsten Heavy Alloys," *Journal of Materials Engineering and Performance,* 8 [1] 46-50 (1999).

62. K. V. Rajulapati, R. O. Scattergood, K. L. Murty, Z. Horita, T. G. Langdon, and C. C. Koch, "Mechanical Properties of Bulk Nanocrystalline Aluminum-Tungsten Alloys," *Metallurgical and Materials Transactions A,* 39 [10] 2528-34 (2008).

63. Q. Wei, H. T. Zhang, B. E. Schuster, K. T. Ramesh, R. Z. Valiev, L. J. Kecskes, R. J. Dowding, L. Magness, and K. Cho, "Microstructure and Mechanical Properties of Super-Strong Nanocrystalline Tungsten Processed by High-Pressure Torsion," *Acta Materialia,* 54 [15] 4079-89 (2006).

64. M. Yao, Z. Zhangjian, T. Jun, and L. Ming, "Fabrication of Ultra-fine Grain Tungsten by Combining Spark Plasma Sintering with Resistance Sintering under Ultra High Pressure," *Rare Metal Materials and Engineering,* 40 [1] 4-8 (2011).

65. E. O. Hall, "The Deformation and Ageing of Mild Steel: II Characteristics of the Lüders Deformation," *Proceedings of the Physical Society B,* 64 [9] 742 (1951).

66. N. J. Petch, "The Cleavage Strength of Polycrystals," *Journal of Iron Steel Institute,* 174 [1] 25-28 (1953).

67. M. Zehetbauer and Y. T. Zhu, "Bulk Nanostructured Materials." Wiley-VCH ; John Wiley [distributor]: Weinheim; Chichester, (2009).

68. B. Seung Woo and K. Jin Ho, "Synthesis of Nanocrystalline $Nd_{16}Fe_{76}B_8$ by Mechanical Alloying and Heat Treatment," *International Journal of Modern Physics B,* 17 [8-9] 1285 (2003).

69. L. L. Ye, Z. G. Liu, K. Raviprasad, M. X. Quan, M. Umemoto, and Z. Q. Hu, "Consolidation of MA Amorphous NiTi Powders by Spark Plasma Sintering," *Materials Science and Engineering A,* 241 [1-2] 290-93 (1998).

70. R. B. Schwarz and W. L. Johnson, "Formation of an Amorphous Alloy by Solid-State Reaction of the Pure Polycrystalline Metals," *Physical Review Letters,* 51 [5] 415-18 (1983).

71. Z. J. Zhang and B. X. Liu, "Solid-State Reaction to Synthesize Ni-Mo Metastable Alloys," *Journal of Applied Physics,* 76 [6] 3351 (1994).

72. B. X. Liu, Z. J. Zhang, O. Jin, and F. Pan, "Metastable Alloys Synthesised by Ion Mixing and Thermodynamic and Kinetic Modeling," *Nuclear Instruments and Methods in Physics Research Section B,* 106 [1-4] 17-22 (1996).

73. R. M. German, "Sintering Theory and Practice.″ Wiley: New York, (1996).

74. R. M. German, "Coarsening in Sintering: Grain Shape Distribution, Grain Size Distribution, and Grain Growth Kinetics in Solid-Pore Systems," *Critical Reviews in Solid State & Materials Science,* 35 [4] 263-305 (2010).

75. R. L. Coble, "Sintering Crystalline Solids I: Intermediate and Final State Diffusion Models," *Journal of Applied Physics,* 32 [5] 787-92 (1961).

76. R. L. Coble, "Initial Sintering of Alumina and Hematite," *Journal of the American Ceramic Society,* 41 [2] 55-62 (1958).

77. G. C. Nelson, "Ceramics: A Potter's Handbook.″ Holt, Rinehart and Winston: New York, (1971).

78. D. Rhodes, "Stoneware & Porcelain : The Art of High-Fired Pottery.″ Chilton Co., Book Division: Philadelphia, (1959).

79. J. E. White and M. M. Jurkowitz, "Hot Pressing of Tungsten Powder.″ Defense Technical Information Center: Ft. Belvoir, Aerospace Corp E. L. Segundo Calif, (1963).

80. W. Chen, U. Anselmi-Tamburini, J. E. Garay, J. R. Groza, and Z. A. Munir, "Fundamental Investigations on the Spark Plasma Sintering/Synthesis Process - I. Effect of DC Pulsing on Reactivity," *Materials Science and Engineering A,* 394 [1-2] 132-38 (2005).

81. U. Anselmi-Tamburini, S. Gennari, J. E. Garay, and Z. A. Munir, "Fundamental Investigations on the Spark Plasma Sintering/Synthesis Process - II. Modeling of Current and Temperature Distributions," *Materials Science and Engineering A,* 394 [1-2] 139-48 (2005).

82. U. Anselmi-Tamburini, J. E. Garay, and Z. A. Munir, "Fundamental Investigations on the Spark Plasma Sintering/Synthesis Process III. Current Effect on Reactivity," *Materials Science and Engineering A,* 407 [1-2] 24-30 (2005).

83. Y. Wang, K. Wang, N. Tan, C. Liu, Y. Li, and Z. Kou, "High Pressure Sintering Behavior of Polycrystalline Diamond with Tungsten," *High Pressure Research,* 31 [3] 419-27 (2011).

84. P. Matteazzi and F. Wolf, "Mechanomaking of High Speed Steel AISI M2: Powders Fabrication," *Materials Science and Engineering A,* 246 [1-2] 235-43 (1998).

85. L. Redouani and S. Boudrahem, "Hot Isostatic Pressing Process Simulation: Application to Metal Powders," *Canadian Journal of Physics,* 90 [6] 573-83 (2012).

86. A. Jinka, "A Finite-Element Prediction of Densification Kinetics during the Hot Isostatic Pressing of Metal Powder Compacts," *Journal of Materials Processing Technology,* 57 [3/4] 382-92 (1996).

87. R. Orru, R. Licheri, A. M. Locci, A. Cincotti, and G. C. Cao, "Consolidation/Synthesis of Materials by Electric Current Activated/Assisted Sintering," *Materials Science & Engineering R,* 63 [4-6] 127-287 (2009).

88. S. Chanthapan, A. Kulkarni, J. Singh, C. Haines, and D. Kapoor, "Sintering of Tungsten Powder With and Without Tungsten Carbide Additive by Field Assisted Sintering Technology," *International Journal of Refractory Metals and Hard Materials,* 31 [1] 114-20 (2012).

89. "Isocarb I-85 Graphite," pp. Isocarb I-85 Graphite Mechanical Properties. in*,* Vol. 2013. Electrodes, Inc., 2013.

90. "AXF-5Q." in*,* Vol. 2012. Edited by I. Poco Graphite. Poco Graphite, Inc, 1997-2012.

91. J. R. Groza and A. Zavaliangos, "Sintering Activation by External Electrical Field," *Materials Science and Engineering A,* 287 [2] 171-77 (2000).

92. T. Nishimura, M. Mitomo, H. Hirotsuru, and M. Kawahara, "Fabrication of Silicon Nitride Nano-Ceramics by Spark Plasma Sintering," *Journal of Materials Science Letters,* 14 [15] 1046-47 (1995).

93. L. Gao, Z. Shen, H. Miyamoto, and M. Nygren, "Superfast Densification of Oxide/Oxide Ceramic Composites," *Journal of the American Ceramic Society,* 82 [4] 1061-63 (1999).

94. K. Nogi and T. Kita, "Rapid Production of β-$FeSi_2$ by Spark-Plasma Sintering," *Journal of Materials Science,* 35 [23] 5845-49 (2000).

95. M. Radwan, T. Kashiwagi, and Y. Miyamoto, "New Synthesis Route for Si_2N_2O Ceramics Based on Desert Sand," *Journal of the European Ceramic Society,* 23 [13] 2337-41 (2003).

96. B. Basu, T. Venkateswaran, and D. Y. Kim, "Microstructure and Properties of Spark Plasma-Sintered ZrO_2-ZrB_2 Nanoceramic Composites," *Journal of the American Ceramic Society,* 89 [8] 2405-12 (2006).

97. W. Tian, K. Vanmeensel, P. Wang, G. Zhang, Y. Li, J. Vleugels, and O. Van der Biest, "Synthesis and Characterization of Cr_2AlC Ceramics Prepared by Spark Plasma Sintering," *Materials Letters,* 61 [22] 4442-45 (2007).

98. A. Nakahira, M. Tamai, H. Aritani, S. Nakamura, and K. Yamashita, "Biocompatibility of Dense Hydroxyapatite Prepared Using an SPS Process," *Journal of Biomedical Materials Research,* 62 [4] 550-7 (2002).

99. A. Bellosi, F. Monteverde, and D. Sciti, "Fast Densification of Ultra-High-Temperature Ceramics by Spark Plasma Sintering," *International Journal of Applied Ceramic Technology,* 3 [1] 32-40 (2006).

100. Y. Kimura, H. Yamaoka, N. Sekido, and Y. Mishima, "Processing, Microstructure, and Mechanical Properties of Nb/Nb_5Si_3 Two-Phase Alloys," *Metallurgical and Materials Transactions A,* 36 [3] 483-88 (2005).

101. X. L. Shi, G. Q. Shao, X. L. Duan, R. Z. Yuan, and H. H. Lin, "Mechanical Properties, Phases and Microstructure of Ultrafine Hardmetals Prepared by WC-6.29Co Nanocrystalline Composite Powder," *Materials Science and Engineering A,* 392 [1-2] 335-39 (2005).

102. I. J. Shon, H. C. Kim, D. H. Rho, and Z. A. Munir, "Simultaneous Synthesis and Densification of Ti_5Si_3 and Ti_5Si_3-20 vol% ZrO_2 Composites by Field-Activated and Pressure-Assisted Combustion," *Materials Science and Engineering A,* 269 [1-2] 129-35 (1999).

103. S. Mula, K. Mondal, S. Ghosh, and S. K. Pabi, "Structure and Mechanical Properties of Al-Ni-Ti Amorphous Powder Consolidated by Pressure-Less, Pressure-Assisted and Spark Plasma Sintering," *Materials Science and Engineering A,* 527 [16-17] 3757-63 (2010).

104. P. Angerer, E. Neubauer, L. G. Yu , and K. A. Khor, "Texture and Structure Evolution of Tantalum Powder Samples During Spark-Plasma-Sintering (SPS) and Conventional Hot-Pressing," *International Journal of Refractory Metals and Hard Materials,* 25 [4] 280-85 (2007).

105. G. Yamamoto, Y. Sato, M. Omori, K. Yokomizo, T. Hashida, T. Takahashi, A. Okubo, S. Watanabe, and K. Tohji, "Route to the Synthesis of Binder-Free SWCNT Solids with Enhanced Mechanical Properties," *AIP Conference Proceedings,* 832 [1] 425-29 (2006).

106. X. Y. Zhang, S. H. Tan, J. X. Zhang, D. L. Jiang, B. Hu, and C. Gao, "Lossy AlN-SiC Composites Fabricated by Spark Plasma Sintering," *Journal of Materials Research,* 19 [9] 2759-64 (2004).

107. T. Mori, T. Nishimura, K. Yamaura, and E. Takayama-Muromachi, "High Temperature Thermoelectric Properties of a Homologous Series of n-Type Boron Icosahedra Compounds: A Possible Counterpart to p-Type Boron Carbide," *Journal of Applied Physics,* 101 [9] 1-4 (2007).

108. D. M. Minić, A. Maričić, and B. Adnađević, "Crystallization of α-Fe Phase in Amorphous $Fe_{81}B_{13}Si_4C_2$ Alloy," *Journal of Alloys and Compounds,* 473 [1-2] 363-67 (2009).

109. Y. D. Sun, P. Shen, Z. Q. Li, J. S. Liu, M. Q. Cong, and M. Jiang, "Kinetics of Crystallization Process of Mg–Cu–Gd Based Bulk Metallic Glasses," *Journal of Non-Crystalline Solids,* 358 [8] 1120-27 (2012).

110. A. A. Abu-Sehly and A. A. Elabbar, "Kinetics of Crystallization in Amorphous $Se_{73.2}Te_{21.1}Sb_{5.7}$ Under Isochronal Conditions: Effect of Heating Rate on the Activation Energy," *Physica B-Condensed Matter,* 390 [1-2] 196-202 (2007).

111. H. A. Calderon, G. Kostorz, and G. Ullrich, "Microstructure and Plasticity of Two Molybdenum-Base Alloys (TZM)," *Materials Science & Engineering A,* 160 [2] 189-99 (1993).

112. ASTM Standard B311-93, "Test Method for Density Determination for Powder Metallurgy (P/M) Materials Containing Less Than Percent Porosity." in. ASTM International, West Conshohocken, PA, 1993 (2002).

113. ASTM Standard E112-96, "Standard Test Methods for Determining Average Grain Size." in. ASTM International, West Conshohocken, PA, 1955 (2004).

114. P. Scherrer, "Bestimmung der Grösse und der inneren Struktur von Kolloidteilchen mittels Röntgensrahlen," *Nachr Ges Wiss Goettingen, Math-Phys Kl,* 26 [1] 98-100 (1918).

115. G. K. Williamson and W. H. Hall, "X-ray line broadening from filed aluminium and wolfram," *Acta Metallurgica,* 1 [1] 22-31 (1953).

116. L. Vegard, "Die Konstitution der Mischkristalle und die Raumfllung der Atome," *Zeitschrift für Physik,* 5 [1] 17-26 (1921).

117. J. M. Joubert and N. Dupin, "Mixed Site Occupancies in the μ Phase," *Intermetallics,* 12 [12] 1373-80 (2004).

118. J. J. English, "Tungsten-Iron System, Binary and Ternary Phase Diagrams of Cb, Mo, Ta, and W, DMIC Rep. 152," pp. 124-29. in ASM Alloy Phase Diagrams Center. ASM International, Materials Park, OH, 1961.

119. P. Gustafson, "An Experimental Study and a Thermodynamic Evaluation of the Cr-Fe-W System," pp. 2531-46. in Metallurgical and Materials Transaction A, Vol 19, ASM Alloy Phase Diagrams Center. ASM International, Materials Park, OH, 1988.

120. V. Raghavan, "Fe-Mo-W (Iron-Molybdenum-Tungsten)," pp. 627-28. in Journal of Phase Equilibria, Vol 15, ASM Alloy Phase Diagrams Center. ASM International, Materials Park, OH, 1994.

121. Z. Munir, U. Anselmi-Tamburini, and M. Ohyanagi, "The Effect of Electric Field and Pressure on the Synthesis and Consolidation of Materials: A Review of the Spark Plasma Sintering Method," *Journal of Materials Science,* 41 [3] 763-77 (2006).

122. G. Skandan, H. Hahn, B. H. Kear, M. Roddy, and W. R. Cannon, "The Effect of Applied Stress on Densification of Nanostructured Zirconia during Sinter-Forging," *Materials Letters,* 20 [5] 305-09 (1994).

123. R. Cooper, S. A. Manktelow, F. Wong, and L. E. Collins, "The Sintering Characteristics and Properties of Hard Metal with NiCr Binders," *Materials Science & Engineering A,* 105 [1] 269-73 (1988).

124. V. Srikanth and G. Upadhyaya, "Sintered Properties of WCrNi Heavy Alloys," *Journal of the Less Common Metals,* 120 [2] 213-24 (1986).

125. M. Kikuchi, H. Usuki, M. Kajihara, and R. Tanaka, "Precipitation of Sigma Phase in Nickel-Rich Ni-Cr-W Alloys as an Intermediate Precipitate," *Scripta Metallurgica,* 19 [4] 421-24 (1985).

126. D. Y. Kim and A. Accary, "Sintering Processes." Plenum Press: New York, NY, (1980).

127. A. Bock, W. D. Schubert, and B. Lux, "Inhibition of Grain Growth on Submicron Cemented Carbides," *Powder Metallurgy,* 24 [1] 20-6 (1992).

128. T. Chookajorn, H. A. Murdoch, and C. A. Schuh, "Design of stable nanocrystalline alloys," *Science* 337 [6097] 951-4 (2012).

129. J. M. Joubert, "Crystal Structure, Hydrogen Absorption Properties and Crystal Structure of the Deuterides of some Nb–Ni Derived Phase Compounds," *Journal of Solid State Chemistry,* 178 [5] 1620-29 (2005).

130. V. Raghavan, "Cr-Fe-W (Chromium-Iron-Tungsten)," pp. 539-42. in Journal of Phase Equilibria, Vol 15, ASM Alloy Phase Diagram Center. ASM International, Materials Park, OH, 1994.

131. C. Wang, L. Cheng, and Z. Zhao, "FEM Analysis of the Temperature and Stress Distribution in Spark Plasma Sintering: Modelling and Experimental Validation," *Computational Materials Science,* 49 [2] 351-62 (2010).

132. Z. W. Zhang, G. L. Chen, G. Chen, and J. E. Zhou, "Amorphization and Thermal Stability of Mechanical Alloyed W–Ni–Fe," *Materials Science and Engineering: A,* 417 [1–2] 34-39 (2006).

133. P. A. Carvalho and J. T. M. De Hosson, "Stacking Faults in the Co_7W_6 Isomorph of the μ Phase," *Scripta Materialia,* 45 [3] 333-40 (2001).

134. W. Trzebiatowski, H. Ploszek, and J. Lobzowski, "X-Ray Analysis of Chromium-Molybdenum and Chromium-Tungsten Alloys," *Analytical Chemistry,* 19 [2] 93-95 (1947).

135. S. T. Murphy, A. Chroneos, C. Jiang, U. Schwingenschlögl, and R. W. Grimes, "Deviations from Vegards Law in Ternary III-V Alloys," *Physical Review B,* 82 [7] (2010).

136. W. Li, P. Markus, and L. Jari, "Lattice Parameter in GaNAs Epilayers on GaAs: Deviation from Vegard's law," *Applied Physics Letters,* 78 [19] (2001).

137. C. Aragó, C. L. Wang, and J. A. Gonzalo, "Deviations from Vegard's Law in the Curie Temperature of Mixed Ferroelectric Solid Solutions," *Ferroelectrics,* 337 [1] 233-37 (2006).

138. D. Zhou and B. F. Usher, "Deviation of the AlGaAs Lattice Constant from Vegard's Law," *Journal of Physics D: Applied Physics,* 34 [10] 1461-65 (2001).

139. A. V. G. Chizmeshya, M. R. Bauer, and J. Kouvetakis, "Experimental and Theoretical Study of Deviations from Vegard's Law in the Sn_xGe_{1-x} System," *Chemistry of Materials,* 15 [1] 2511-19 (2003).

140. M. G. D. Baumann, "Spectroscopic and Structural Properties of Molecular Solid Solutions Between Photoluminescent Quadruply-Bonded Molybdenum and Tungsten Compounds," pp. 163. in Chemistry, Vol. Doctor of Philosophy. University of Wisconsin, United States, 1993.

141. J. Poetschke, V. Richter, and R. Holke, "Influence and Effectivity of VC and Cr_3C_2 Grain Growth Inhibitors on Sintering of Binderless Tungsten Carbide," *International Journal of Refractory Metals and Hard Materials,* 31 [1] 218-23 (2012).

142. U. K. Vashi, R. W. Armstrong, and G. E. Zima, "The Hardness and Grain Size of Consolidated Fine Tungsten Powder," *Metallurgical Transactions,* 1 [6] 1769-71 (1970).

APPENDIX A

Other Common Names for Pulsed Electric Current Sintering[87]

Other Common Names for Pulsed Electric Current Sintering

(Direct) Electric resistance sintering (ERS)
Direct resistance sintering
Electric charge sintering
Electric conduction sintering
Electric contact sintering
Electric current activated/assisted sintering (ECAS)
Electric current sintering
Electric discharge compaction (EDC)
Electro discharge consolidation (EDC)
Electric discharge sintering (EDS)
Electric field assisted sintering (EFAS)
Electric pressure sintering (EPS)
Electric pulse assisted (EPA) consolidation
Electric pulse current sintering
Electric pulse discharge sintering
Electric pulse sintering (EPS)
Electric sintering
Electrical discharge-type activated pressure sintering
Electrically activated pressure sintering
Electroconsolidation (EC)
Electroplastic compression (EC)
Environmental electric discharge sintering (EEDS)
Field activated pressure assisted combustion synthesis (FAPACS)
Field activated pressure assisted (FAPA) combustion synthesis and densification
Field activated pressure assisted synthesis (FAPAS)
Field activated sintering technique (FAST)
Field assisted densification
High-energy High Rate (HEHR) consolidation
Impulse plasma sintering
Instrumented electric discharge consolidation
Instrumented pulse discharging consolidation
Instrumented pulse electro discharge consolidation
Plasma activated sintering (PAS)
Plasma assisted sintering (PAS)
Plasma pressure compaction (P_2C) or (PPC)
Plasma sintering
Pulse current activated sintering (PCAS)
Pulse current hot quasi-isostatic pressing (PCHIP)

Pulse current hot pressing (PCHP)
Pulse current pressure sintering (PCPS)
Pulse current sintering (PCS)
Pulse discharge sintering (PDS)
Pulse electric current pressure sintering (PECPS)
Pulse electric current sintering (PECS)
Pulse electric discharge consolidation
Pulse high current (PHC) heating sintering
Pulse plasma sintering (PPS)
Resistance heated hot pressing
Resistance sintering (RS)
Resistance sintering under pressure
Resistance sintering under ultra-high pressure (RSHUP)
Resistive sintering
Spark discharge sintering
Spark isostatic pressing (SIP)
Spark plasma activated sintering
Spark plasma sintering (SPS)
Spark pressure sintering
Spark sintering

APPENDIX B

Results for PECS W+, W9Cr1, W8Cr2, W9Mo1, and W8Mo2 Specimens

Table 14 Densities, porosities, hardnesses, grain sizes and crystallite sizes of W+, W9Cr1, W8Cr2, W9Mo1, and W8Mo2 pulsed electric current sintered specimens.

Alloy-Temp-Time-Pressure	*Density (g/cm^3)*	*Porosity (%)*	*Hardness (HV)*	*Grain Size (μm)*	*Crystallite Size (nm)*
W+-1000C-1min-HP	16.43	6.73	1102	-	35
W+-1100C-1min-HP	17.75	0.14	1349	-	43.5
W+-1200C-1min-HP	18.11	0.06	1117	-	-
W+-1000C-20min-HP	17.56	1.79	1351	-	42
W+-1100C-20min-HP	17.86	0.00	1090	-	48.5
W+-1100C-1min-LP	17.55	1.28	1207	-	-
W+-1200C-1min-LP	18.11	0.05	1038	-	-
W+-1300C-1min-LP	18.10	0.10	893	-	-
W+-1400C-1min-LP	18.03	0.08	768	2.03	-
W+-1500C-1min-LP	18.16	0.49	693	3.10	-
W+-1100C-20min-LP	18.05	0.83	968	-	-
W+-1200C-20min-LP	18.15	0.05	852	1.78	-
W+-1300C-20min-LP	18.04	0.03	765	2.26	-
W+-1400C-20min-LP	17.83	0.27	684	3.46	-
W9Cr1-1000C-1min-HP	15.52	5.29	400	-	34
W9Cr1-1050C-1min-HP	16.06	1.24	1188	-	32.5
W9Cr1-1100C-1min-HP	16.90	0.64	1347	-	38
W9Cr1-1200C-1min-HP	17.22	0.03	1395	-	-
W9Cr1-1000C-20min-HP	15.84	1.45	940	-	29.5
W9Cr1-1100C-20min-HP	16.93	0.15	1281	-	44.5
W9Cr1-1100C-1min-LP	16.09	2.51	1072	-	-
W9Cr1-1200C-1min-LP	17.31	0.04	1220	-	-
W9Cr1-1300C-1min-LP	17.03	0.01	1079	-	-
W9Cr1-1400C-1min-LP	17.18	0.17	899	1.69	-
W9Cr1-1500C-1min-LP	17.41	0.55	895	2.34	-
W9Cr1-1600C-1min-LP	17.67	0.55	777	4.04	-
W9Cr1-1700C-1min-LP	17.98	0.99	684	6.60	-
W9Cr1-1100C-20min-LP	17.28	0.08	1325	-	-

W9Cr1-1200C-20min-LP	17.77	0.05	1037	1.21	-
W9Cr1-1300C-20min-LP	17.37	0.06	899	2.12	-
W9Cr1-1400C-20min-LP	17.54	0.44	772	2.79	-
W8Cr2-1000C-1min-HP	14.05	9.80	642	-	21.5
W8Cr2-1050C-1min-HP	15.24	3.76	1231	-	30
W8Cr2-1100C-1min-HP	15.91	1.63	1520	-	35.5
W8Cr2-1000C-20min-HP	15.11	2.63	989	-	30
W8Cr2-1100C-20min-HP	16.16	0.56	1398	-	41
W9Mo1-1000C-1min-HP	16.20	0.05	1132	-	35.5
W9Mo1-1050C-1min-HP	17.07	0.00	1229	-	42
W9Mo1-1100C-1min-HP	17.32	0.00	1132	-	47.5
W9Mo1-1000C-20min-HP	17.23	0.04	1391	-	43.5
W9Mo1-1100C-20min-HP	17.38	0.00	955	-	48.5
W8Mo2-1000C-1min-HP	15.94	0.072	1320	-	37.5
W8Mo2-1050C-1min-HP	17.07	0.43	1360	-	42
W8Mo2-1100C-1min-HP	17.32	0.01	1316	-	43.5
W8Mo2-1000C-20min-HP	16.38	0.01	1417	-	43.5
W8Mo2-1100C-20min-HP	16.40	0.06	1050	-	-